POLITECNICO DI MILANO

Scuola di Ingegneria Industriale e dell' Informazione

Corso di Laurea Magistrale in
Ingegneria Energetica

EVALUATION OF MINIATURIZED FAST RESPONSE PROBES

Relatore: Prof. Giacomo Bruno PERSICO

Co-relatore: Prof. Guillermo PANIAGUA

Tesi di Laurea di:

Giovanni BONETTI Matr.780494

Anno Accademico 2012 - 2013

Acknowledgements

First of all I need to thank my family for their support and their sacrifices. Thanks, for everything you did so far for me.
I am also very grateful to prof. Giacomo Persico for trusting me as a student and giving me the opportunity to work in the Von Kármán Institute. Thank you also for your help, and for being always available to support me until the very last minute.
My gratitude goes to Prof. Guillermo Paniagua, for accepting me as a member of his team, for advising me, and to all the people I met during this experience. It has been very great to see from this special perspective how researchers work.
The biggest thank goes to Dr. Sergio Lavagnoli for his constant presence and support during my stage and for everything he taught me. About measurements, but also about life.
I wouldn't have been able to carry on the project without hints from Cis for the CFD, David for Catia and Valeria for Matlab. Thank you Oscar for using the routine I implemented and for suggesting corrections. Thanks Fabrizio for being very kind with the last minute setup for probes testing. Special thanks to Angela for helping me with tests. I wish you all the best for the rest of your project, and for the work I left you to carry on. I know you can make it, don't forget it!
Thanks to my flatmate Giulia and all the other amazing people I've got to know in Belgium. I hope to see you again somewhere on this little planet. Thanks to the other friends I left in Italy which shared with me some moments of real life during these years at Politecnico.
And thanks to Anna, for the help with the acronyms, but especially for all the rest you did for me in these months.

Contents

List of figures

List of tables

Abstract

Measurements of aerodynamic performances in turbomachinery require continuous development of miniaturized instruments capable to capture the unsteadiness of the flow. Two new prototypes of miniaturized fast response pressure probes for total pressure measurements and flow directions are developed. A state of the art single hole pressure probe is selected as a reference design for the prototypes. A smaller transducer is chosen to get further miniaturization. Geometrical dimensions are scaled and optimized accordingly. To increase angular insensitivity for total pressure measurements a Kiel shaped shield is introduced. Aerodynamic performances of probes in operating conditions are also modelled numerically solving URANS equations with Numeca FINE/Open™. A multi parameters approach is implemented and adopted to assess the convergence of unsteady computations. Two prototypes are manufactured and preliminary tests for angular sensitivity are executed.

Italian summary

Capitolo 1
Introduzione

Negli scorsi decenni lo sviluppo delle turbine a gas è stato trainato prevalentemente dalla disponibilità di nuovi materiali capaci di resistere a sollecitazioni elevate ad alte temperature. Tuttavia lo studio dell'aerodinamica delle turbomacchine continua a giocare un ruolo di primaria importanza nel settore. Oggetto di questa tesi è lo sviluppo di sonde di pressione miniaturizzate ad alta risposta in frequenza che verranno impiegate nell' ambito di una campagna sperimentale al Von Kármán Institute for Fluid Dynamics in Belgio. Benché siano sviluppate per una specifica applicazione, gli usi delle sonde sono molteplici.
Il Von Kármán Institute è un centro di ricerca in ambito fluidodinamico organizzato in tre dipartimenti: Environmental & Applied Fluid Dynamics, Aeronautics & Aerospace, Turbomachinery. Possiede svariate gallerie del vento e installazioni specifiche per campagne sperimentali. Una delle più significative è la CT3. Si tratta di una facility rotante su cui sono montati uno stadio e mezzo di turbina transonica di alta pressione (statore-rotore-statore). Le sonde oggetto di questo lavoro verranno impiegate nella CT3. Questa tesi è stata sviluppata durante un tirocinio presso l'istituto sotto la supervisione del professor G. Paniagua.

Gli strumenti per misure fluidodinamiche generalmente devono essere il meno intrusivi possibile, per minimizzare le alterazioni del flusso indotte dalla misura. Questo aspetto è particolarmente critico per le misure in turbomacchine, a causa delle ridotte sezioni di passaggio e delle alte velocità del flusso. Per questa ragione lo sviluppo di strumentazione nel settore è continuamente orientato verso la miniaturizzazione delle sonde. Oltretutto, a causa della forte instazionarietà del flusso, strumenti di misura per queste applicazioni devono avere dei tempi di risposta molto rapidi. Frequenze di risposta desiderate sono dell'ordine dei 40-50 kHz.

Tra le grandezze di maggior rilievo per la caratterizzazione del flusso ci sono la pressione totale e la velocità. Esse sono correlate tra loro: dalla conoscenza della distribuzione di pressione su un corpo immerso in un fluido è possibile determinarne la velocità. Per misurare la pressione totale è prassi comune arrestare il flusso mediante il naso di una sonda su cui può essere posizionato un

sensore, oppure una presa di pressione collegata ad un sensore remoto tramite una linea pneumatica.

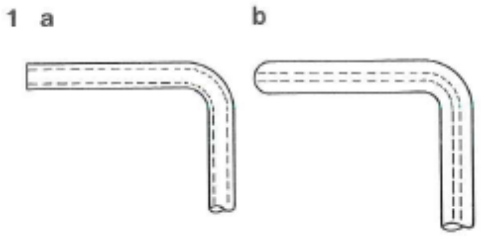

Figura 1.2. Forme classiche della parte terminale di sode per misure di pressione totale. [3]

Le misure di pressione totale sono molto sensibili alla direzione del flusso incidente. Per rendere lo strumento meno sensibile all'angolo di attacco, talvolta si realizza una piccola schermatura, meglio conosciuta come "Kiel".

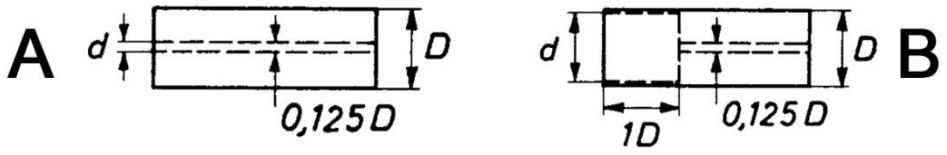

Figura 1.4. Forme classiche della parte terminale di sode per misure di pressione totale. Dettaglio del foro. [3]

Si può misurare la pressione totale anche utilizzando sonde cilindriche immerse nel flusso trasversalmente, dotate di fori sul fianco. In questo caso però la pressione avvertita dalla sonda corrisponde alla pressione totale del flusso indisturbato solo per piccoli angoli di incidenza.

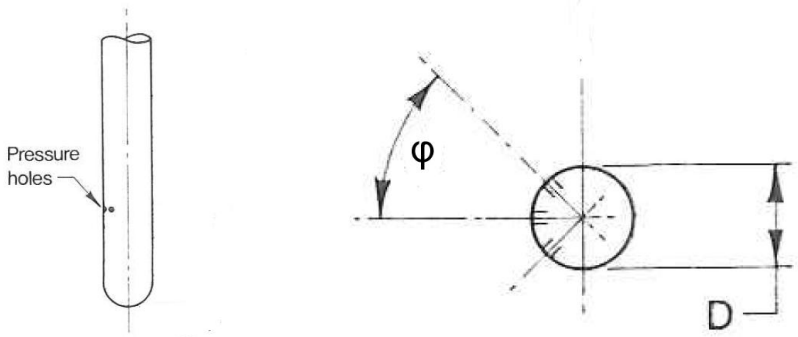

Figura 1.5. Vista frontale e in sezione di una sonda cilindrica impiegata trasversalmente rispetto al flusso.

Sonde di pressione di questo tipo sono molto utilizzate per misure direzionali. La distribuzione di pressione sul profilo della sonda, infatti, può essere ricondotta alle caratteristiche del flusso indisturbato. Geometrie alternative al cilindro sono possibili, come nel caso di sonde direzionali di tipo wedge. Le sonde direzionali possono essere dotate di uno o più fori a seconda della specifica metodologia di misura adottata. Generalmente la pressione rilevata dai diversi sensori è ricondotta alle caratteristiche del flusso attraverso degli opportuni coefficienti che costituiscono le mappe di calibrazione.

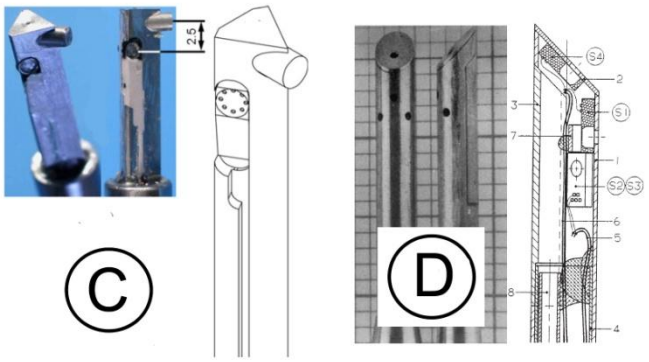

Figura 1.7. Esempi di sonde direzionali. C) 3-hole wedge probe per misure in turbine transoniche sviluppato al VKI da Delhaye. D) Sonda cilindrica a quattro fori sviluppata all' ETH Zurich.

In questo lavoro una sonda di pressione cilindrica ad un foro viene scelta per le misure direzionali e adottata come design di riferimento. La sonda viene ulteriormente miniaturizzata e per misurare di pressione totale, viene aggiunto un piccolo schermo cilindrico (Kiel) nei pressi della presa di pressione, con l'intento di migliorarne l'insensibilità all'angolo del flusso.

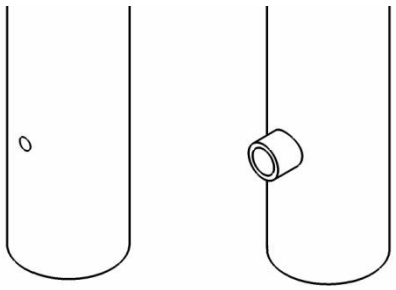

Figura 1.9 - Sonda cilindrica ad un foro e relativa configurazione Kiel oggetto di questa tesi.

Nel capitolo 2 si illustrano i criteri adottati nel design e nell'ottimizzazione della geometria per i prototipi. Nel capitolo 3 viene descritta una metodologia impiegata per la verifica della convergenza di simulazioni non stazionarie. Nel capitolo 4 si illustra l'uso della termofluidodinamica computazionale (CFD) per lo studio dell'aerodinamica esterna e confrontare le prestazioni delle due sonde.
Il capitolo 6 evidenzia le conclusioni e illustra i risultati ottenuti dai test preliminari sui prototipi.

Capitolo 2
Design delle sonde

Il design di ciascuna sonda parte necessariamente da una stima delle caratteristiche del flusso che deve essere misurato. Ciascuno strumento è caratterizzato da un range di funzionamento che determina sia la qualità della misura che l'integrità della strumentazione. Le sonde sviluppate in questo lavoro verranno impiegate in una campagna sperimentale all'interno della facility CT3 del von Kármán Institute a valle del rotore. Da simulazioni numeriche del flusso nella turbomacchina sono stati ottenuti gli intervalli di variabilità delle grandezze fluidodinamiche nella zona di misura. Tra questi valori è stata selezionata la media come situazione rappresentativa delle condizioni operative.

Tabella 2.1. Intervallo di variabilità delle condizioni del flusso nella CT-3 in corrispondenza del piano di misura.

	min	max	mean
T_{TOT} [K]	315	415	365
P_{TOT} [bar]	0.42	0.50	0.46
T_{STAT} [K]	314	395	359
P_{STAT} [bar]	0.42	0.43	0.44
ρ [kg/m^3]	0.465	0.375	0.426
M [m/s]	0.05	0.5	0.275
V [m/s]	17.8	199.1	104.4
Yaw [°]	-90	45	-22.5
Pitch [°]	-90	30	-30
$\rho \cdot V/\mu$ [m^{-1}]	$1 \cdot 10^6$	$6 \cdot 10^6$	$3.5 \cdot 10^6$

In figura 2.2 è schematizzato il profilo della sonda in posizione all'interno della facility. Le sonde generalmente vengono montate su uno stelo di forma cilindrica e vengono introdotte dall'esterno, attraverso fori realizzati nel casing della turbina.

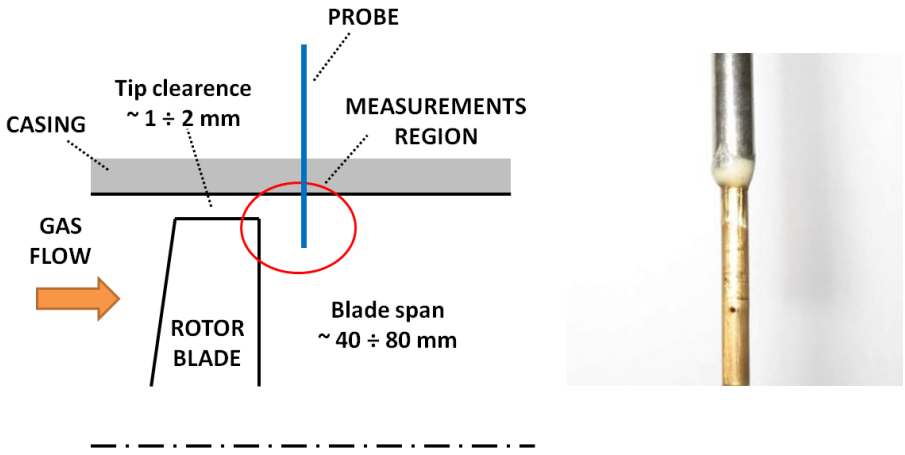

Figura 2.2. Sinistra: schizzo della regione di misura e della posizione della sonda in turbina. Destra: sonda ad un foro sviluppata al Politecnico di Milano (CYL-2b).

Le sonde devono rispettare requisiti di robustezza ed essere compatibili con l'accessibilità del luogo di misura. Ad esempio in caso di classici tubi di Pitot, la dimensione del foro nella cassa della turbina e la curvatura del tubo devono essere adeguati a consentirne l'inserimento. La parte destra di figura 2.2 è la fotografia di una sonda cilindrica a singolo foro sviluppata al Politecnico di Milano (CYL-2b) scelta in questo lavoro come design di riferimento. La semplicità e compattezza della geometria costituiscono la miglior risposta alle varie esigenze operative e conferiscono alla sonda adeguata robustezza. Anche l'introduzione della schermatura, per il Kiel probe, non costituisce una particolare criticità da questo punto di vista poiché le ridotte dimensioni della testa della sonda rispetto allo stelo non ne complicano il montaggio. Insieme alla minore interferenza con il flusso, questo è un altro indubbio vantaggio del Kiel probe rispetto all'uso dei classici Pitot tube.

Un altro grande vantaggio della sonda sviluppata a Milano risiede nella semplicità costruttiva e quindi nel basso costo di produzione. Alcune sonde di pressione per queste applicazioni, vengono realizzate montando all'interno di minuscoli tubicini dei sensori miniaturizzati, con la membrana sensibile rivolta verso la presa di pressione, come nell'esempio riportato in figura 2.3. Ciò viene fatto per tenere la membrana il più possibile vicina al foro e rivolta verso l'esterno da dove provengono le fluttuazioni di pressione. L'esempio riportato in figura, relativo ad una sonda con addirittura quattro fori, chiarisce la complicazione costruttiva e la fragilità dell'apparecchio, soprattutto se si pensa che il diametro esterno della sonda è di soli 2.5 mm. La sonda di Milano, invece, è stata concepita con un approccio più semplice e innovativo. Si tratta di un

cilindro cavo all'interno del quale viene alloggiato un sensore commerciale (anch'esso di geometria cilindrica) con la membrana sensibile rivolta verso il basso (vedi figura 2.3). Le fluttuazioni di pressione raggiungono la membrana passando attraverso la linea pneumatica e la cavità, di forma conica per agevolarne la riflessione verso la membrana piezoresistiva.

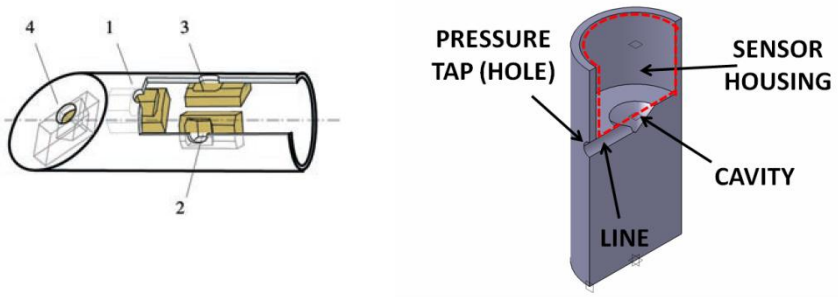

Figura 2.3. Sinistra: dettaglio del montaggio dei sensori all'interno della sonda a quattro fori sviluppata all' ETH Zurich. Destra: dettaglio della configurazione geometrica e dell'alloggiamento del sensore sviluppato al Politecnico di Milano.

Per queste ragioni, la sonda sviluppata a Milano è stata presa in considerazione come design di riferimento. Elemento fondamentale nello sviluppo delle sonde è la scelta del sensore utilizzato.

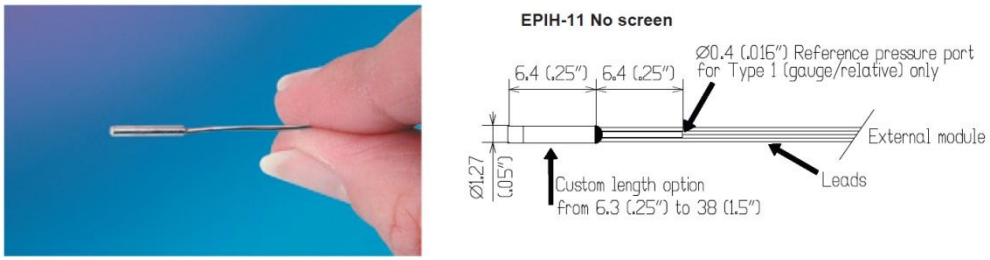

Figura 2.4. Sensori di pressione miniaturizzati. Sinistra: Kulite® XCQ-062. Destra: Dimensioni in mm (inches) del sensore EPIH-11 non schermato commercializzato da Measurement-Specialities™.

Avendo scelto di utilizzare trasduttori disponibili a livello commerciale, confrontando le diverse opzioni disponibili sul mercato, un unico candidato mostra di avere il potenziale per sostituire il Kulite® XCQ-062 utilizzato nella sonda scelta come riferimento. I sensori della serie EPIH prodotti da Measurement-Specialities™ sono molto simili in termini di dimensioni e condizioni operative ai Kulite®. Nella sua versione senza schermo l' EPIH è disponibile con un diametro esterno di 1.27 mm, il che è inferiore agli 1.7 mm del corrispondente Kulite®, offrendo un margine per ridurre le dimensioni complessive della sonda.

La risposta dinamica della sonda dipende dalla propagazione delle onde di pressione nel sistema linea-cavità. Nello sviluppo della sonda di Milano [1] alcuni modelli analitici e numerici sono stati utilizzati per stimare la frequenza di risonanza del sistema. L'approccio più semplice porta al modello di Helmoltz, che si basa su due ipotesi. La prima è che il fluido è soggetto a comprimibilità ma è fermo nella cavità, il che è ragionevole quando la lunghezza assiale della cavità è trascurabile rispetto alla linea. La seconda è che il fluido nella linea possa ritenersi incomprimibile, il che è ragionevole quando il suo volume è trascurabile rispetto a quello della cavità. L'effetto di smorzamento è imputabile alla viscosità ed è calcolato secondo la formula di Poiseuille per flussi laminari incomprimibili.
Tuttavia queste ipotesi non sono valide nella geometria in esame, soprattutto la seconda poiché i volumi di linea e cavità sono dello stesso ordine di grandezza.
Un modello alternativo, attribuito a Houghen *et. al.* [1], si è rivelato più affidabile nella previsione. La particolarità di questo modello, è di considerare l'effetto di comprimibilità anche nella linea. Il modello consiste in due equazioni per stimare frequenza di risonanza ω_n e coefficiente di smorzamento ζ:

$$\omega_n = \frac{c}{L\sqrt{\frac{1}{2}+\frac{V}{Vt}}} \tag{2.1}$$

$$\zeta = \frac{16\mu L\sqrt{\frac{1}{2}+\frac{V}{Vt}}}{d_t^2 c\rho} \tag{2.2}$$

Nelle equazioni, con *V* si intende il volume della cavità, *Vt* è il volume della linea, μ la viscosità, *c* la velocità del suono e ρ la densità. Il diametro del foro (chiamato anche pressure tap, o semplicemente tap) è indicato con d_t e *L* è la lunghezza della linea, che in caso di linee molto piccole è corretta utilizzando L_{corr} invece di *L*. L_{corr} è definita come:

$$L_{corr} = L + \frac{8}{3\pi} d_t \tag{2.3}$$

Con l'introduzione della lunghezza corretta, e facendo riferimento alla notazione descritta in figura 2.5, è possibile riscrivere l'equazione della frequenza di risonanza come:

$$\omega_n = \frac{c}{\left(L^* - \frac{d_t}{2\tan\alpha}\right)\sqrt{\frac{1}{2}+\frac{\frac{\pi D^3 \tan\alpha}{24}}{\frac{\pi d_t^2}{4}\left(L^* - \frac{d_t}{2\tan\alpha}\right)}}} \tag{2.4}$$

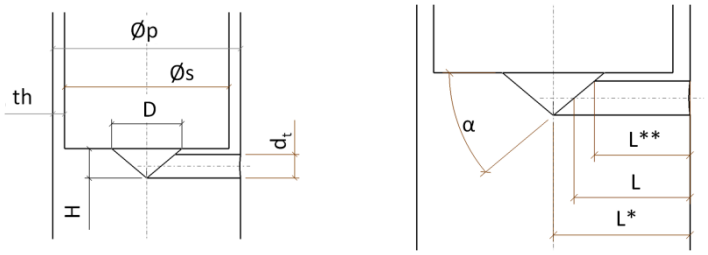

Figura 2.5. Vista in sezione della parte terminale della sonda e riferimenti geometrici usati nell'ottimizzazione. Sinistra: diametro del sensore (*Øs*), diametro esterno della sonda (*Øp*), spessore del materiale (*th*) diametro di base della cavità conica (*D*), altezza della cavità conica (*H*) diametro della linea cilindrica e del foro (d_t). Destra: Dettaglio della definizione della lunghezza della linea utilizzata nelle equazioni. L'angolo della cavità conica è α.

Assumendo che la forma del sistema linea-cavità venga mantenuta e che siano semplicemente scalate alcune dimensioni, l'equazione della frequenza di risonanza di fatto esprime un legame funzionale tra cinque parametri.

$$\omega_n = \mathcal{F}(c, L^*, d_t, \alpha, D) \tag{2.5}$$

Note le condizioni del flusso, e introdotte alcune ulteriori ipotesi, una volta scelto il sensore (che impone ulteriori vincoli sulle dimensioni minime possibili) questo legame è esprimibile in funzione di soli due parametri:

$$\omega_n = \mathcal{F}(d_t, D) \tag{2.8}$$

Assunto come scenario di riferimento il caso con D = 0.8 mm e d_t = 0.3 mm, mantenendo uno spessore di materiale (*th*) pari a 0.1 mm è possibile valutare l'effetto del diametro del foro e della dimensione della cavity per i due sensori disponibili. I risultati sono esposti in tabella 2.2.

Tabella 2.2. Ottimizzazione delle dimensioni di linea e cavità per entrambi i sensori.

Metal thickness (*th*):	0.1 mm
Conical cavity angle (α):	≈ 36.8 °
Sensor:	**XCQ-062**
Sensor diameter:	1.7 mm
Probe external diameter:	1.9 mm

$\omega_n=F(D, d_t)$ [kHz]			
	d_t [mm]		
***D* [mm]**	0.1	0.2	0.3
0.5	42.09	63.11	71.79
0.8	22.73	39.62	50.73
1.2	12.66	23.25	31.63

Metal thickness (*th*):	0.1 mm
Conical cavity angle (α):	≈ 36.8 °
Sensor:	**EPIH-11**
Sensor diameter:	1.27 mm
Probe external diameter:	1.47 mm

$\omega_n=F(D, d_t)$ [kHz]			
	d_t [mm]		
***D* [mm]**	0.1	0.2	0.3
0.5	47.66	73.13	84.35
0.8	25.30	44.11	56.63
1.2	14.02	25.47	34.30

Come previsto si evince che la scelta del sensore più piccolo comporta un margine per un potenziale aumento della frequenza di risonanza rispetto alla sonda di riferimento.
La riduzione del diametro esterno della sonda potrebbe peggiorare la risoluzione spaziale della sonda. Tuttavia, riducendo anche il diametro del foro questo svantaggio è parzialmente compensato. Mediante il modello è stato anche valutato l'impatto che errori nel processo produttivo o tolleranze numeriche possano avere in termini di frequenza di risonanza attesa. Anche nel peggior scenario considerato, la frequenza di risonanza stimata non è mai scesa significativamente al di sotto dei 40 kHz, che è il limite minimo desiderato per queste sonde.
Ulteriori modelli non sono stati considerati, sia perché si sono già rivelati inefficaci nello studio della sonda di Milano, sia perché non diminuirebbero l'incertezza della previsione. Inoltre la fase di realizzazione di un prototipo e relativi test, resta un passaggio imprescindibile per la caratterizzazione del comportamento delle sonde.

In termini di design aerodinamico del profilo, si è scelto di mantenere la forma cilindrica perché si è rivelata essere la più adatta per misure in ampi campi di variabilità del numero di Reynolds (10^3 - 10^5) e in termini di numero di Mach (0.2 - 0.9) [11].

Per minimizzare l'effetto di bloccaggio dovuto all'inserimento della sonda nel flusso, (effetto molto marcato in prossimità della parete) la distanza del foro dall'apice della sonda è stata ridotta a 2 mm. Anche l'effetto di questa decisione verrà verificato a posteriori durante la fase di calibrazione.

Per quanto riguarda la definizione delle dimensioni del Kiel, non esistono validi riferimenti in letteratura, principalmente perché questa configurazione è adottata soprattutto in tubi di Pitot e non per cilindri posti trasversalmente al flusso, come in questo caso. Tuttavia, come rappresentato in figura 2.8 sembra evidente che ci sia una tendenza ad ottenere sonde sempre più insensibili alla direzione del flusso incidente quando viene massimizzato il rapporto $Øk_i/Øk_e$.

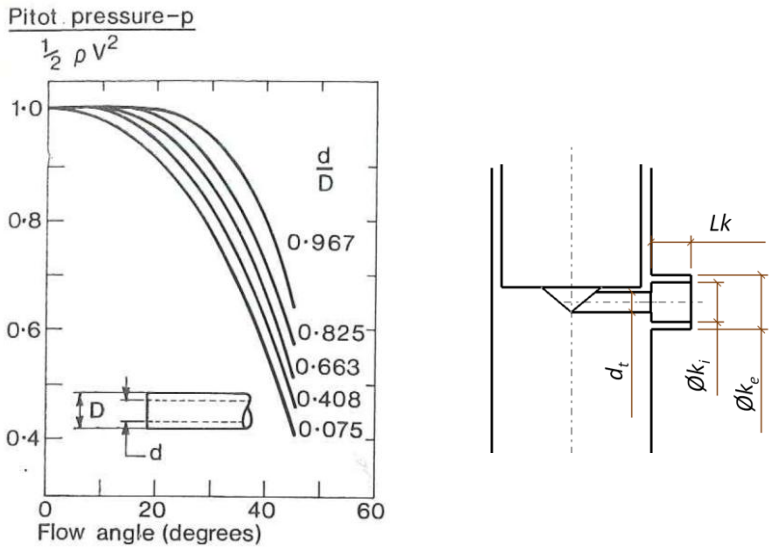

Figura 2.8. Sinistra: effetto dell'angolo del flusso per sonde di pressione totale ad estremità cilindrica [3]. Destra: nomenclatura utilizzata in questa tesi.

Definite le geometrie, la realizzazione dei prototipi è stata fatta mediante elettroerosione (EDM), tecnica che garantisce elevata precisione e buona finitura superficiale a costi ragionevoli. La tolleranza nominale dichiarata dal costruttore è di ± 0.01 mm.

La lunghezza della parte terminale delle sonde è di 25 mm e verrà inserita per 5 mm all'interno dello stelo. Le dimensioni definitive dei prototipi sono illustrate nelle figure 2.11 e 2.12.
Inoltre è stato deciso di:
- lasciare 0.05 mm di materiale tra la linea e l'alloggiamento del sensore;
- aprire leggermente l'angolo della cavità conica, per mantenere D = 0.6 mm e il centro della cavità coincidente con la linea.
La frequenza stimata con il modello è di 56.2 kHz.

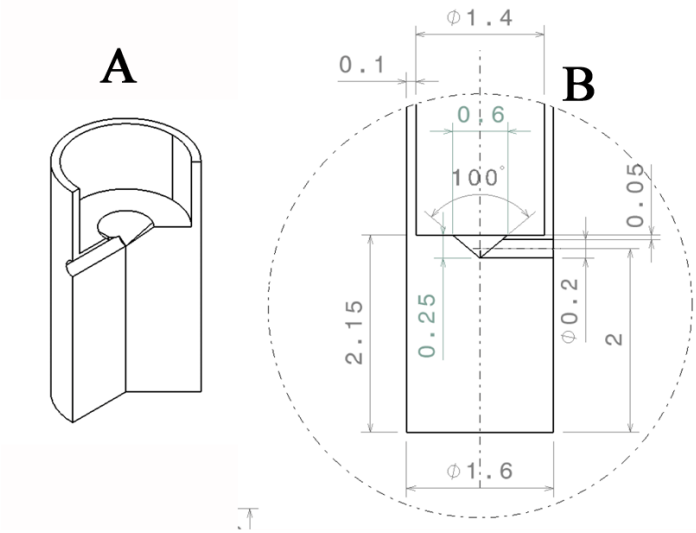

Figura 2.11. Dettaglio della sonda a singolo foro.
Vista tridimensionale in sezione (A) e dimensioni in mm (B).

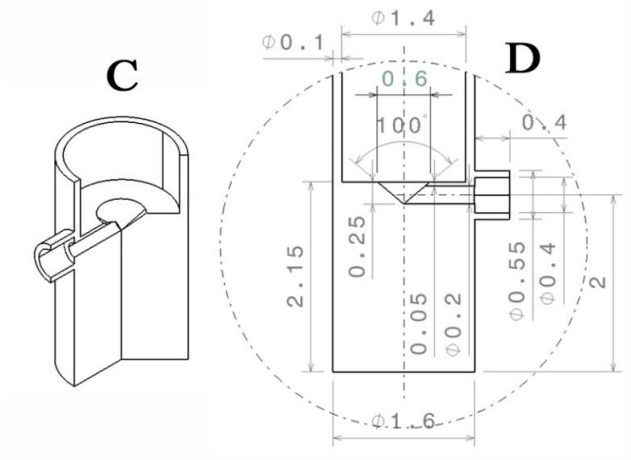

Figura 2.12. Dettaglio della sonda Kiel.
Vista tridimensionale in sezione (C) e dimensioni in mm (D).

Dal punto di vista meccanico sono state fatte due semplici verifiche. La prima riguarda la massima deflessione dovuta dalla forza di trascinamento esercitata dal fluido. La parte terminale della sonda si comporta come una trave incastrata sottoposta a carico uniformemente distribuito lungo la sua lunghezza.

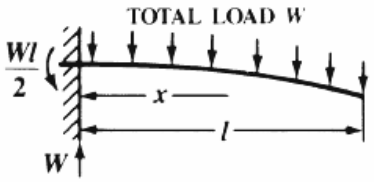

Figura 2.13 . Trave incastrata soggetta a carico uniformemente distribuito. [17]

Il materiale utilizzato è acciaio inossidabile, è la deflessione massima ottenuta all'apice della sonda vale circa $\delta_{max} \approx 3.76$ µm. Nel caso del Kiel probe sicuramente la resistenza offerta dal profilo è maggiore e quindi anche la deflessione prodotta. Tuttavia, data l'entità estremamente ridotta di questo risultato, non si ritiene necessario effettuare ulteriori verifiche in tal senso.
L'ultimo aspetto verificato nel design preliminare è che la frequenza di vibrazione propria della struttura risulti notevolmente inferiore rispetto alla frequenza di vibrazione indotta dal distacco dei vortici. Esiste evidenza sperimentale del disturbo indotto sulla misura a causa delle vibrazioni delle sonde, che inducono fluttuazioni artificiali nelle componenti della velocità nei pressi della presa di pressione.
Da questo punto di vista il problema è assimilabile ad un'asta incastrata con massa concentrata all'apice. Poichè la testa della sonda è cava, per ospitare il sensore, oltre il 95% della massa si trova concentrata all'apice.

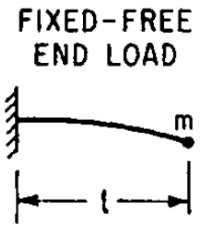

Figura 2.14 . Trave incastrata con massa concentrata all'apice. [18]

La frequenza di oscillazione naturale del corpo risulta essere circa 56.3 Hz. Come volevasi dimostrare è notevolmente al di sotto delle frequenze fluidodinamiche, stimate nell'ordine dei 13 kHz.

Capitolo 3

Convergenza di soluzioni unsteady CFD: approccio multi-parametro

Nelle simulazioni CFD instazionarie, la verifica della convergenza si fa generalmente monitorando delle quantità tempo varianti. Quando queste variabili manifestano un comportamento periodico, la convergenza si ritiene raggiunta. In questo lavoro, l'approccio proposto da J.P. Clark e E.A. Grover [19] è stato preso in considerazione. Il metodo è stato proposto per simulazioni instazionarie di flusso nelle turbomacchine, ma i principi su cui si basa sono di validità generale e può quindi essere esteso a qualsiasi variabile che raggiunta la convergenza manifesti un comportamento periodico. Il metodo si basa sul confronto di periodi consecutivi, effettuato combinando tra loro diverse caratteristiche di ciascun periodo, esprimendole in forma adimensionale con i seguenti coefficienti:

$$fM = 1 - \left|1 - \frac{\overline{q_2}}{\overline{q_1}}\right| \tag{3.12}$$

$$fA(k+1) = 1 - \left|1 - \frac{A(k+1)_2}{A(k+1)_1}\right| \tag{3.13}$$

$$fFI(n) = 1 - \left|1 - \frac{\phi(k+1)_2 - \phi(k+1)_1}{\pi}\right| \tag{3.14}$$

$$fS = |CCF(0)| \tag{3.15}$$

$$fP = \frac{\sum_{k_{expected}} PSD(k+1)}{\sum_{k=0}^{N-1} PSD(k+1)} \tag{3.16}$$

I coefficienti proposti per l'osservazione delle variabili soggette a convergenza riguardano l'andamento del valor medio, modulo e fase della trasformata di Fourier per le frequenze di interesse, quantità di energia contenuta nella frazione dello spettro (nel dominio delle frequenze) corrispondente alle frequenze ricercate, coefficiente di cross correlazione. Per come sono stati definiti, questi coefficienti assumono valore unitario quando periodi tra loro consecutivi sono uguali, condizione che si raggiunge una volta ottenuta la convergenza. Il monitoraggio della convergenza può quindi essere effettuato controllando solo il minimo tra questi parametri oppure osservandoli tutti. La soluzione si ritiene a

convergenza quando tutti i parametri prossimi all'unità, maggiori di una determinata soglia.
La soglia proposta da J.P. Clark e E.A. Grover [19] è fissata a 0.95.
Il metodo è stato implementato in una routine in ambiente Matlab® ed inizialmente testato su segnali generati artificialmente. Come si evince dalla figura 3.1 durante l'evoluzione della variabile monitorata verso la periodicità, tutti gli indicatori crescono e tendono all'unità al termine del transitorio.

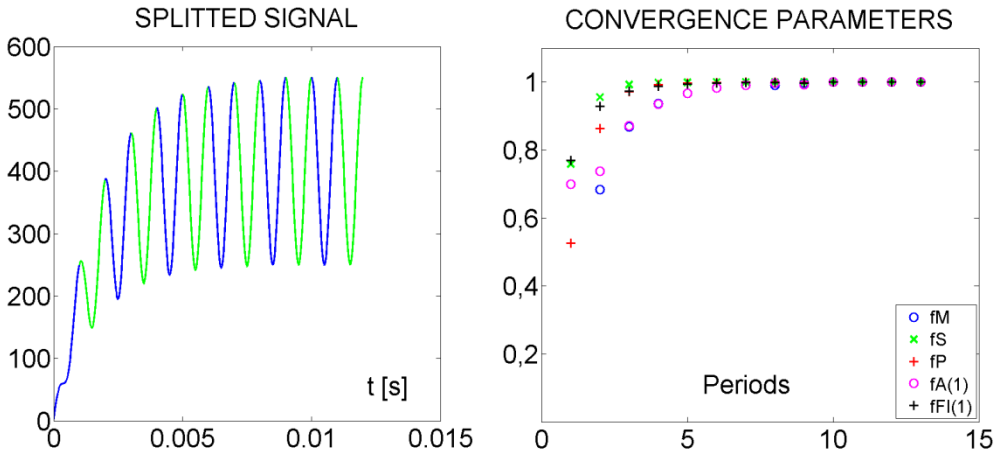

Figura 3.1. Esempio di un segnale che evolve verso un andamento periodico e relativi parametri di convergenza.

L'implementazione del metodo, e la generalizzazione della procedura hanno richiesto un cambio di prospettiva rispetto al punto di vista degli autori che hanno proposto questo approccio. Nelle simulazioni del flusso in turbomacchine, la periodicità di primo interesse è correlata alla frequenza di passaggio delle pale, che è nota a priori ed imposta come condizione al contorno del problema. In una generica simulazione instazionaria quale il flusso esterno attorno ad un profilo, invece, l'entità dell'instazionarietà è nota solo a posteriori. Il suo ordine di grandezza può essere stimato ma l'esatto valore ottenuto dipende dalla soluzione del problema. Per determinare la lunghezza dei periodi da confrontare, bisogna necessariamente tenere in considerazione questo aspetto. Di conseguenza, il codice implementato in Matlab® non è completamente automatico e richiede senso critico e interazione con l'utente.

L'applicazione della procedura a soluzioni di generiche simulazioni instazionarie ha rivelato delle potenziali criticità nel metodo dovute principalmente a:
- situazioni in cui la lunghezza dei periodi non è un multiplo esatto del passo di discretizzazione temporale;
- discretizzazione temporale troppo lasca;

- errata scelta della frequenza fondamentale da parte dell'utente.
Tutte queste situazioni di fatto dipendono dalla discretizzazione impiegata nell'analisi e possono comportare bassi valori degli indicatori della convergenza anche a convergenza avvenuta. Per ovviare a questo problema è stata introdotta la possibilità di interpolare la soluzione incrementando il numero di punti disponibili per periodo.

Capitolo 4
Analisi numerica delle prestazioni

Le prestazioni delle sonde sono state analizzate mediante modellazione numerica, avvalendosi della termofluidodinamica computazionale (CFD). La natura del flusso reale attorno al profilo, è completamente tridimensionale. Tuttavia si ritiene che una rappresentazione bidimensionale del profilo delle sonde immerso nel flusso possa fornire validi risultati benchè aprossimati. La validità del modello verrà confermata o smentita posteriori, mediante il confronto con l'evidenza sperimentale.

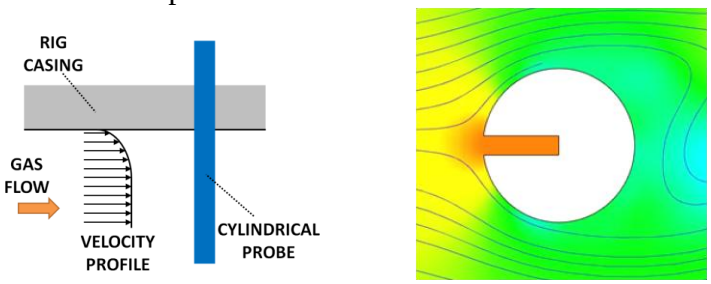

Figura 4.1. Sinistra: schizzo del profilo della sonda nella turbina.
Destra: vista in sezione della sonda cilindrica in corrispondenza della presa di pressione.

Il regime di moto attorno al profilo è assimilabile a quello del flusso trasversale rispetto al cilindro, tipicamente classificato in letteratura utilizzando il numero di Reynolds e di Strouhal.

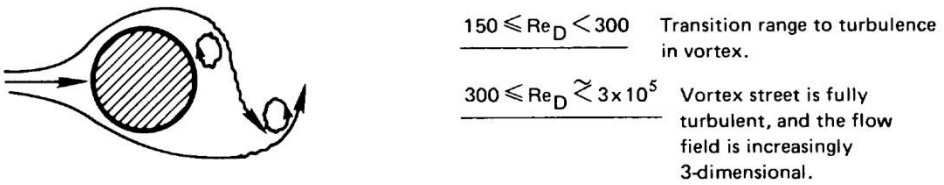

Figura 4.2. Particolare del regime di flusso attorno al cilindro [21].

Il numero di Reynolds stimato è circa 3000, quindi il regime di moto atteso è di flusso subcritico. Tramite il numero di Strouhal (0.21) è possibile stimare la frequenza di distacco dei vortici, (f_v = 14857 Hz) e la corrispondente scala temporale. La lunghezza del periodo T è di $6.73 \cdot 10^{-5}$ secondi. La stima della scala temporale è necessaria per la definizione di un adeguato passo di discretizzazione per il solutore, che facendo riferimento a lavori analoghi, viene scelto $1 \cdot 10^{-6}$ secondi.
Il problema è modellato come flusso turbolento esterno ad un profilo. Il solutore impiegato è Numeca FINE™/Open. Il modello di turbolenza scelto è Spalart-Allmaras per tre ragioni:

1) è stato storicamente sviluppato per la modellazione di flussi esterni attorno a profili;
2) è basato su una singola equazione, il che costituisce un vantaggio in termini computazionali, soprattutto alla luce del fatto che il problema è instazionario e richiede una quantità notevole di iterazioni prima di raggiungere la convergenza;
3) è considerato sufficientemente robusto sia per griglie lasche che per griglie con discretizzazione spaziale molto fitta.

Per la risoluzione di problemi stazionari il solutore usa uno schema di tipo Runge-Kutta esplicito in quattro stadi. Per la soluzione dei problemi instazionari, si avvale della tecnica dual time stepping. I metodi numerici scelti hanno un'accuratezza del secondo ordine.

La definizione del dominio si è basata su informazioni relative a lavori analoghi presenti in letteratura. Poichè non si è riscontrato un parere univoco al riguardo, ci si è riferiti principalmente al lavoro di D. Delhaye *et. al.* [17].
Assunto come lunghezza caratteristica il diametro della sonda il dominio rettangolare si estende per 20 diametri a valle del profilo, e per 10 rispettivamente a monte e ai fianchi.

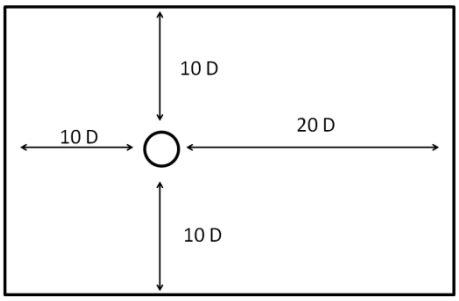

Figura 4.4. Estensione del dominio attorno al profilo.

La dimensione delle celle è stata definita mediante analisi di sensitività della mesh non strutturata, caratterizzata da tre zone con diversa discretizzazione spaziale. Con riferimento alla figura sottostante, un passo di discretizzazione sempre più piccolo è stato imposto andando dalla zona esterna (A), alla regione di scia (B), ed infine nei pressi del profilo (C) dove le celle hanno la dimensione minima. In termini di grandezza adimensionale delle celle in parete ($y+$), è stato mantenuto ovunque un valore inferiore ad 1.

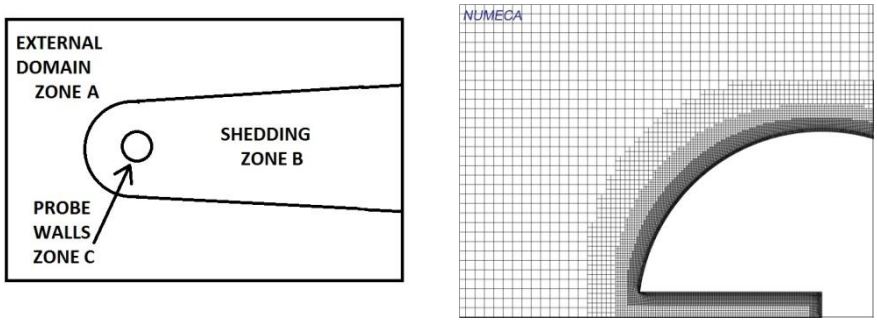

Figura 4.5. Sinistra: dettagli delle zone a diversa discretizzazione del dominio. Destra: particolare della griglia scelta con l'analisi di sensitività nei pressi del profilo.

Per la definizione della discretizzazione spaziale si è provato a stimare l'incertezza usando il metodo del Grid Convergence Index proposto da Roache [28] [29] basato sull'estrapolazione di Richardson. Alcune mesh sono state generate e le soluzioni ottenute con le diverse discretizzazioni sono state paragonate, selezionando alcune variabili. Poichè le quantità sono tempo varianti, il confronto è stato fatto in termini di valor medio, ampiezza delle oscillazioni, e frequenza. La frequenza è risultata piuttosto indipendente dalla discretizzazione spaziale mentre il valor medio e le oscillazioni si sono rivelati molto più sensibili. Il trend è evidente in figura 4.7.

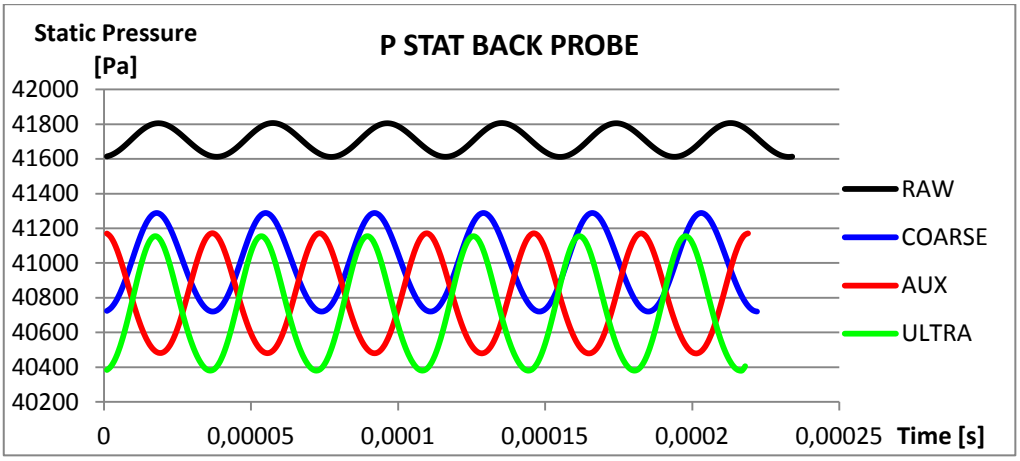

Figura 4.7. Esempio di evoluzione delle variabili monitorate in funzione del diverso livello di discretizzazione spaziale.

Dall'analisi di sensitività si è concluso che l'analisi dell'incertezza può essere inaccurata in questo caso a causa dell'elevato valore del parametro *p*. Per la mesh selezionata si è ottenuto un GCI generalmente inferiore all'1% per i valori medi, e variabile generalmente tra il 4% e il 12% per quanto riguarda l'entità delle oscillazioni. Il trend assunto dalle quantità analizzate indica chiaramente che la mesh *AUX* è quella migliore. Ulteriori infittimenti della griglia non portano nessun vantaggio significativo.

Definite le caratteristiche della mesh, si è proceduto realizzandone diverse, variando di volta in volta l'orientamento della sonda rispetto al dominio. In questo modo è stato possibile variare l'angolo di incidenza del flusso mantenendo le stesse caratteristiche della mesh nella regione di scia.
Le condizioni al contorno imposte sono di tipo "external" [24] [26], adottando i seguenti valori:

- Pressione statica: 43800 [Pa]
- Temperatura statica: 360 [K]
- Numero di Mach: 0.275
- Direzione del flusso: parallelo all'asse *x* nel sistema di riferimento cartesiano della griglia

Per il modello di turbolenza, avendo assunto un rapporto tra viscosità turbolenta e cinematica pari a 100 (da simulazioni CFD del flusso nella facility) si è ricavato un valore di viscosità turbolenta da imporre ai confini del dominio pari a ν_T of $5.05 \cdot 10^{-3}$ m^2/s.

Per la verifica della convergenza, si sono monitorate le forze di lift e drag sul profilo e la procedura illustrata nel capitolo 3 è stata applicata. Si è adottata una soglia pari a 0.99 e un fattore di sovracampionamento pari a 10. Un esempio delle forze di lift e drag ottenute a convergenza è dato in figura 4.11, e i relativi parametri di convergenza in figura 4.12.

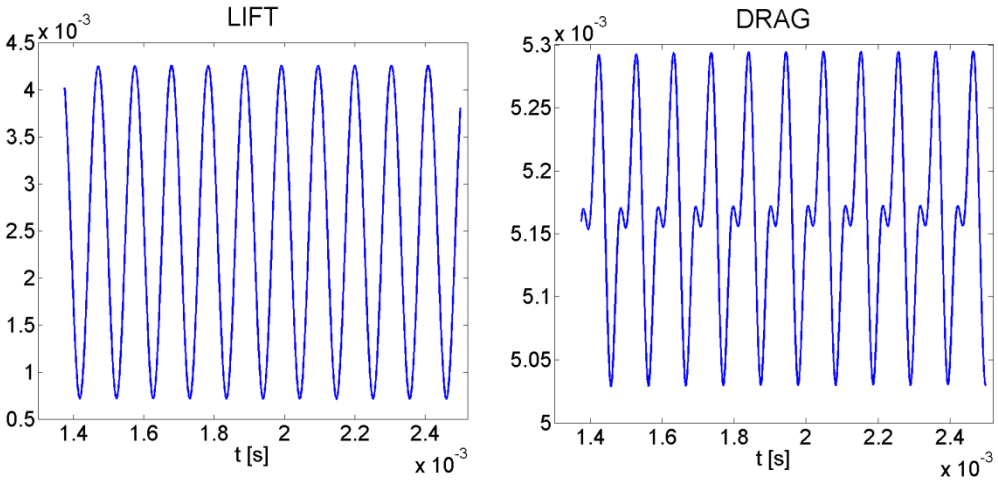

Figura 4.11. Forza di lift e di drag sul profilo della sonda con Kiel inclinata di 30° rispetto al flusso a convergenza raggiunta.

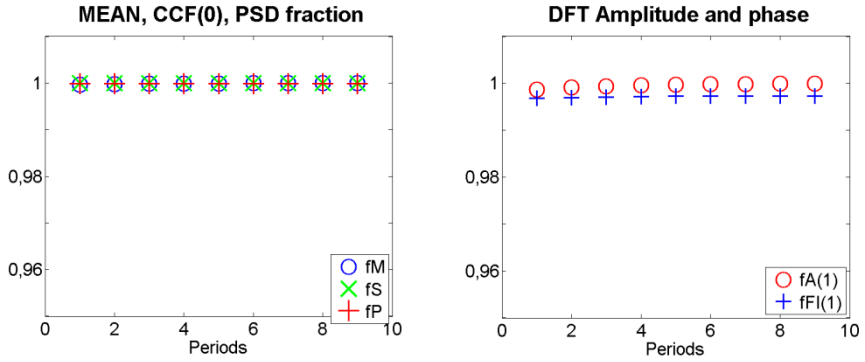

Figura 4.12. Indicatori di convergenza ottenuti applicando la procedura descritta nel capitolo 3 alle variabili rappresentate in figura 4.11.

Per ciascun time step si sono calcolate 50 sub iterazioni e tutti i residui normalizzati al termine dei time step della soluzione a convergenza sono inferiori alle potenze di 10^{-7}.

La validità del modello numerico è stata prima di tutto verificata facendo riferimento al caso del cilindro. Per quanto riguarda il numero di Strouhal i risultati sono coerenti con le aspettative mentre in termini di coefficiente di drag (e quindi di distribuzione di pressione sulla sonda) l'errore è circa del 30%.
E' stato posto il problema in termini di:
1) validità del modello di turbolenza;
2) influenza delle condizioni al contorno;
3) presenza della presa di pressione sul profilo (non è un cilindro perfetto)
4) influenza del numero di Mach.
Sicuramente il modello di turbolenza costituisce una fonte di errore significativa, tuttavia studi simili [27] hanno rilevato margini di errore che vanno dal 25 al 39% anche utilizzando altri modelli di turbolenza. Risultati migliori sono stati ottenuti con modelli algebrici (Reynolds stress models) o simulazioni DES, ma l'eccessivo costo computazionale ne vanificherebbe i benefici.
L'effetto delle condizioni al contorno e della presenza della presa di pressione nel profilo si sono rivelati poco influenti sulla distribuzione di pressione.
L'effetto più marcato é attribuibile alla comprimibilità. Benchè il numero di Mach agli estremi del dominio sia relativamente basso (0.275), è stata riscontrata una dipendenza del coefficiente di drag non trascurabile. Alcuni casi simulati numericamente, confrontati con le misure effettuate da Rodriguez [20] certificano che le correlazioni del coefficiente di drag ottenute da vari autori per flussi a bassa velocità non sono generalizzabili a flussi anche moderatamente comprimibili.

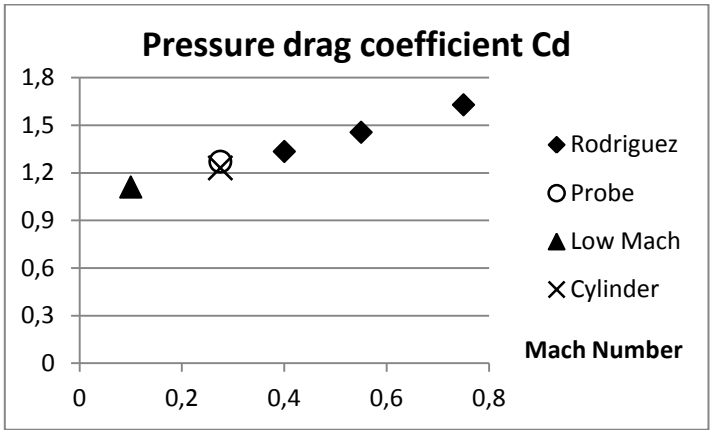

Figura 4.21. Coefficiente di drag ottenuto numericamente per la sonda in condizioni nominali (*Probe*), per il cilindro in condizioni nominali (*Cylinder*) e per la sonda a basso numero di Mach (*Low Mach*). Coefficiente di drag misurato da Rodriguez (Rodriguez).

Alla luce di queste osservazioni, pur trattandosi di un modello approssimato e affetto da semplificazioni, si può ritenerlo in grado di fornire stime ragionevoli della distribuzione di pressione sui profili delle sonde da confrontare.

In termini di sensitività angolare, le due sonde possono essere confrontate sulla base di un coefficiente di pressione così definito:

$$Cp = \frac{p - p_2}{p_0 - p_2} \tag{4.40}$$

in cui p è la pressione media sulla presa di pressione, p_2 la pressione statica a valle del dominio e p_0 la pressione totale a monte. I risultati sono rappresentati in figura 4.24 e messi a confronto con un profilo di pressione teoricamente atteso, secondo Bryer and Pankhurst [3].

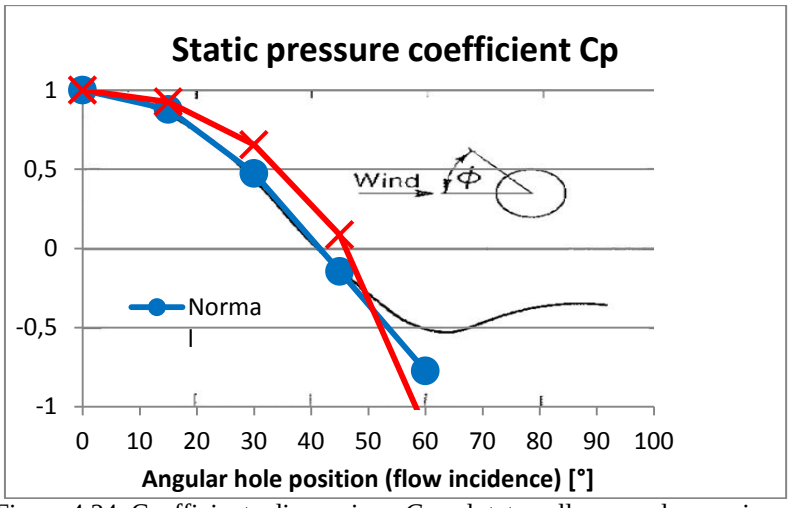

Figura 4.24. Coefficiente di pressione *Cp* valutato sulla presa do pressione.

In termini di *Cp* l'introduzione del Kiel comporta un guadagno del 5% a 15° e del 38% per 30°.
Esprimendo i risultati mediante il coefficiente di calibrazione per la pressione totale utilizzato per caratterizzare la sonda a cui è ispirato questo lavoro, è possibile estendere il confronto dei risultati ottenuti con le simulazioni CFD con le caratteristiche riscontrate per la sonda di riferimento:

$$K_{pt} = \frac{P_t - P_c}{P_t - P_s} \tag{4.41}$$

Nell'equazione (4.41) P_t e P_s sono rispettivamente la pressione statica e totale, mentre P_c è il valore di pressione misurata.

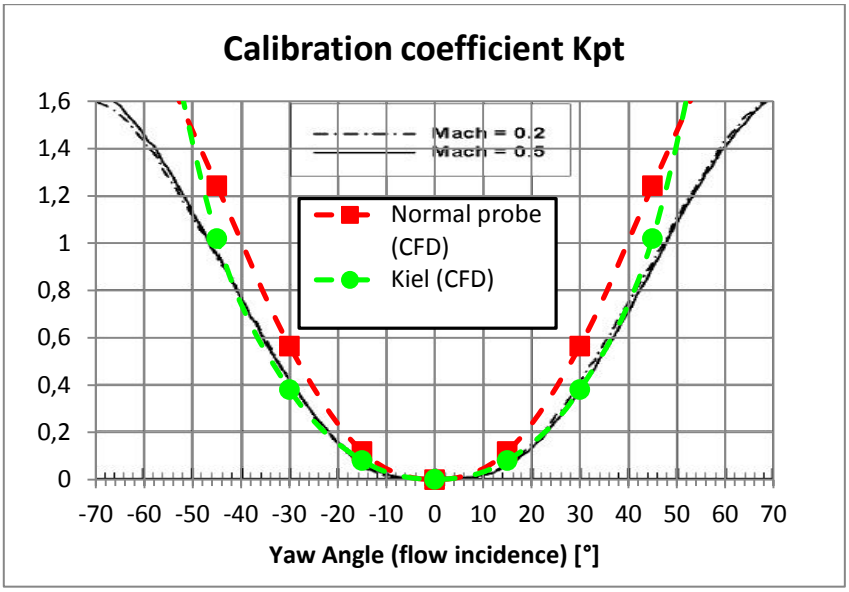

Figura 4.25. Confronto del coefficiente di calibrazione *Kpt* stimato col modello numerico per le nuove sonde e determinato sperimentalmente al Politecnico di Milano.

Secondo il modello numerico, la nuova sonda dovrebbe presentare una diversa pendenza nella curva del coefficiente di calibrazione, e il vantaggio introdotto dal Kiel viene sostanzialmente confermato. Tuttavia, anche da questo confronto non pare esserci una evidente e nettamente più ampia regione di insensibilità alla direzione del flusso.
Il modello numerico è stato utilizzato anche per valutare l'effetto della lunghezza del Kiel. Dai risultati ottenuti si può ritenere che la lunghezza scelta sia adeguata.

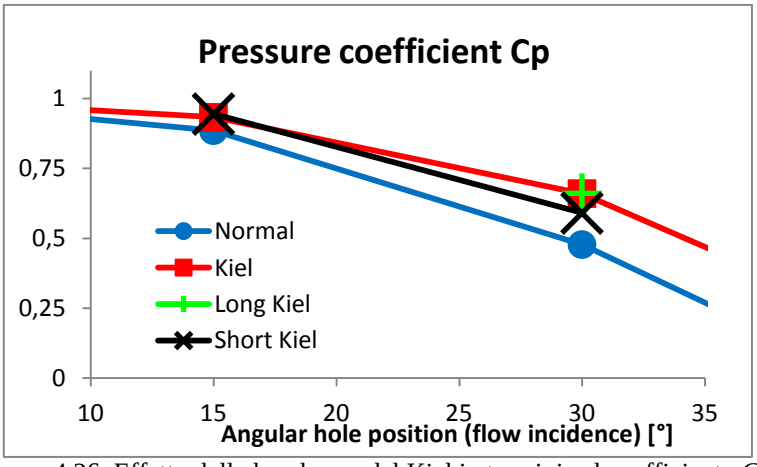

Figura 4.26. Effetto della lunghezza del Kiel in termini sul coefficiente *Cp*.

Ulteriori osservazioni dei risultati hanno portato alla conclusione che la differenza tra la pressione letta dalla sonda e quella rilevata sulla superficie della presa di pressione dipende (oltre che dalle caratteristiche dinamiche del sistema linea-cavità) anche dalla direzione del flusso incidente. Nel caso della sonda cilindrica a singolo foro questo fatto comporta una penalizzazione crescente all'aumentare dell'angolo di incidenza del flusso. Per il Kiel probe, questo effetto è completamente assente poichè il flusso viene arrestato completamente prima di raggiungere l'inizio della linea. Dall'osservazione delle fluttuazioni di pressione indotte dal distacco dei vortici si sono osservati tre aspetti importanti.

1) Anche se di piccola intensità, le componenti fluttuanti della pressione possono propagarsi lungo tutta la linea e raggiungere la cavità, introducendo un errore sulla misura di pressione.

2) L'intensità dei disturbi indotti dal distacco di vortici cresce progressivamente muovendosi dal punto di ristagno andando verso la parte posteriore del profilo, come osservato nel lavoro di Rodriguez [20].

3) La presenza del Kiel sembra essere in grado di mitigare l'effetto di questi disturbi, ma solo fino al raggiungimento di un valore limite dell'angolo di incidenza, oltre il quale il disturbo cresce sensibilmente.

Per elevati angoli di incidenza, il modello numerico individua l'insorgere di un fenomeno di ricircolo all'interno del Kiel, davanti alla presa di pressione, più accentuato per il caso a 60° ma già evidente a 45°.

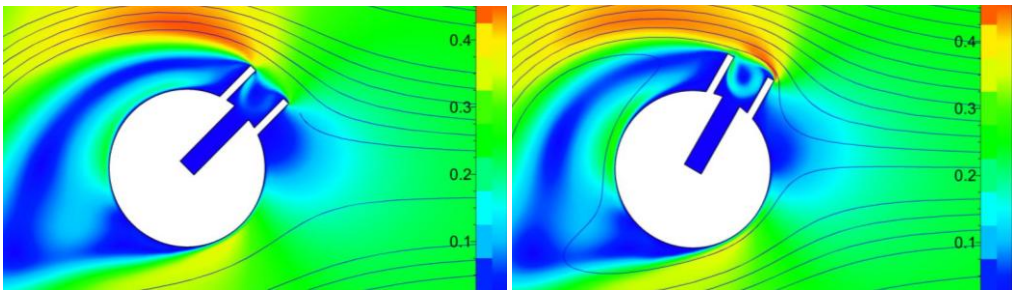

Figura 4.31. Numero di Mach per istanti corrispondenti attorno al profilo della sonda con Kiel per angoli di incidenza del flusso di 45° e 60°.

Capitolo 5
Test preliminari e conclusioni

Due prototipi sono stati realizzati e sottoposti a test preliminari per dimostrare la fattibilità delle sonde e capire se il design possa essere confermato per produrne altri oppure debba essere perfezionato. Nel momento in cui questa viene scritta pochi risultati sperimentali sono disponibili, e l'attività di verifica è tutt'ora in corso.

La risposta delle sonde per diversi angoli di flusso è stata verificata ponendole all'interno del getto di un ugello calibrato e ruotandole tra i -90° e i +90°.
Per la sonda cilindrica a singolo foro i risultati sembrano essere soddisfacenti.

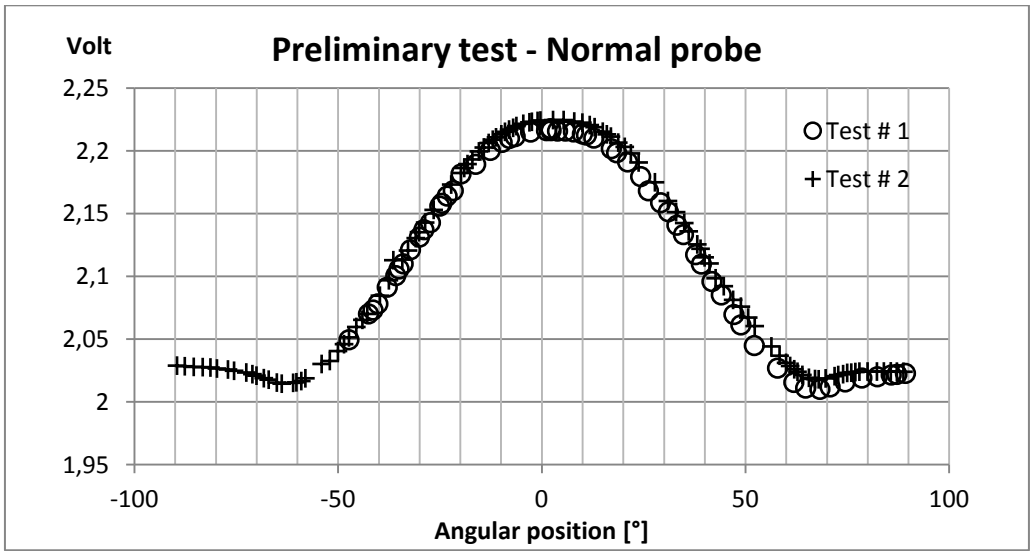

Figura 5.5. Test preliminare per la sonda cilindrica a singolo foro.

In termini di coefficiente di calibrazione per la pressione totale i risultati evidenziano un diverso range di linearità e sostanzialmente una diversa sensitività rispetto alla sonda in uso al Politecnico di Milano.

I risultati ottenuti con il modello CFD dimostrano ancora una volta di essere affetti da un errore in termini assoluti. La bontà del confronto fatto col modello numerico tra Kiel e sonda normale non è stata verificata a causa degli scarsi risultati ottenuti per il Kiel.

I risultati dei test preliminari ottenuti per il Kiel probe non sono incoraggianti. Benchè i risultati esposti in questo lavoro siano parzialmente compromessi da un effetto di deriva termica (questi test sono stati fatti "a feddo" per varie ragioni) che verrà rimosso nelle prossime prove, le curve sembrano essere caratterizzate da una forte asimmetria, e soprattutto risultano dipendenti dalla storia temporale della prova. Il picco ben evidente in figura 5.8 infatti compare in entrambe le prove durante la prima parte del test. Test # 2 infatti è stato eseguito partendo da angoli negativi e muovendosi progressivamente verso quelli positivi; per test # 3 vale il viceversa.

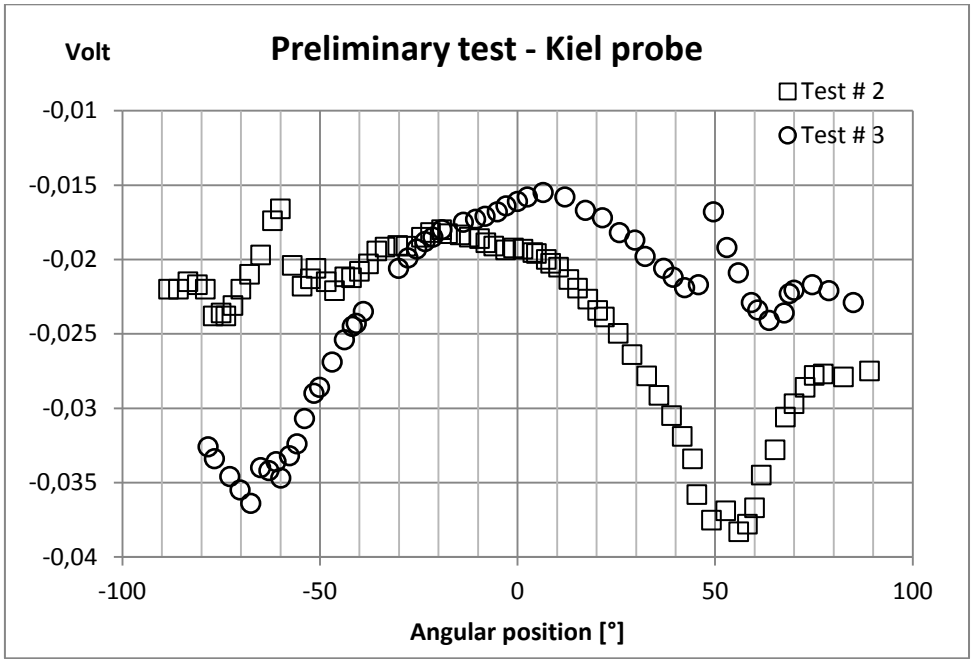

Figura 5.8. Test preliminare di sensitività angolare per il Kiel probe.

Questo fenomeno può essere dovuto principalmente a due ragioni:
1) imperfezioni ed errori nella realizzazione della sonda,
2) design del Kiel errato.

Benchè ci siano indizi a sostegno della prima delle due ipotesi, è ritenuta poco probabile, soprattutto perchè non sarebbe in grado di giustificare la dipendenza della misura dalla storia dell'angolo di incidenza del flusso.
La seconda invece è più probabile. In particolare, alla luce dei risultati ottenuti con il modello numerico è lecito sospettare che nell'intorno dei 50° possa esserci una bolla circolatoria all'interno del Kiel. Il fenomeno (più accentuato secondo i calcoli CFD ad angoli più elevati) potrebbe instaurarsi proprio per elevati angoli di incidenza, e raggiunto un valore critico la struttura dello strato limite potrebbe cambiare drasticamente, determinando il picco rilevato nelle prove. Ulteriori

prove come quella rappresentata in figura 5.10 dimostrano che operando all'interno di un range più ristretto di angoli di incidenza questo fenomeno non si verifica. Così è possibile che, passando da piccoli angoli di incidenza ad angoli più grandi, il fenomeno circolatorio possa non innescarsi, e ciò giustificherebbe l'asimmetria del picco rilevata nei primi test.

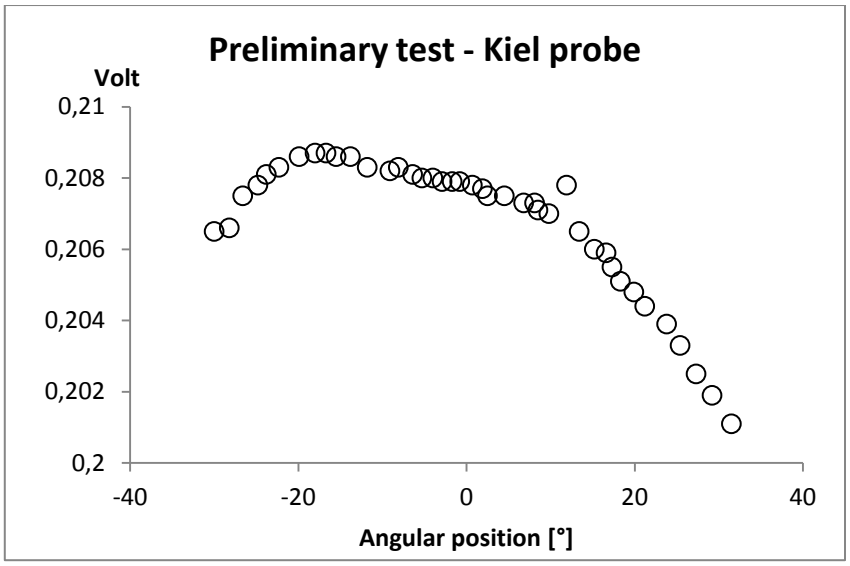

Figura 5.10. Test preliminare di sensitività angolare per il Kiel probe.

Questa spiegazione è puramente intuitiva e andrebbe verificata mediante ulteriori test e indagini teoriche più approfondite.
Tuttavia, a prescindere dalla spiegazione e descrizione di questo fenomeno, se i prossimi test confermeranno questi risultati preliminari la sonda con il Kiel risulta essere inaffidabile per le misure in turbomacchine.
Ulteriori geometrie, andrebbero considerate per futuri sviluppi. Per esempio si potrebbero uniformare le dimensioni del Kiel e della linea pneumatica con un unico condotto a diametro interno costante, oppure convergente.

Mentre i risultati della sonda con Kiel appaiono deludenti, se le prove dinamiche confermeranno le aspettative riguardo la sonda cilindrica a singolo foro, questa potrebbe costituire l'esemplare più piccolo del mondo nel suo genere, essendo più piccola sia della sonda in uso al Politecnico di Milano che della sonda cilindrica a singolo foro sviluppata a Zurigo.

La naturale prosecuzioni di questo lavoro è il completamento dei test preliminari, la calibrazione e l'uso delle sonde nella prossima campagna sperimentale. Questo lavoro prosegue grazie al lavoro del Dr. Sergio Lavagnoli e Angela Morelli.

Chapter 1

Introduction

Turbomachinery performances in the last 60 years have been improving significantly, thanks to a continuous effort in research and development which involves many disciplines. The largest contribution to higher efficiency came from the development of metal alloys able to withstand higher temperature, and improved blade design. Accurate estimates of temperature distribution are required to prevent damages and to predict components lifetime. Blade cooling and heat transfer phenomena in such critical conditions require thorough theoretical, numerical and experimental investigations. Forecasts for future air transport demand ask for more efficient and compact engines. Thus, even though modern engines efficiencies are very high and there are limits imposed by thermodynamics which cannot be overtaken, the industry still require a great amount of research and development for a detailed characterization of turbines. At the Von Kármán Institute for Fluid Dynamics (VKI) research on turbines is conducted mainly through experiments and numerical simulations. This thesis regards the development of miniaturized fast response pressure probes to be used for an upcoming experimental campaign. In this chapter some introductory ideas regarding pressure measurements are presented and the research objectives and methodology explained.

1.1 The Von Kármán Institute

The Von Kármán Institute (VKI) is located in Rhode Saint-Genèse in Belgium a few kilometres south of Brussels. It is named after the famous scientist Theodore Von Kármán who, in the course of 1955, was also chairman of the Advisory Group for Aeronautical Research and Development (AGARD) of NATO. He proposed with his assistants, Frank Wattendorf and Rolland Willaume, the establishment of an institution devoted to training and research in aerodynamics which would be open to young engineers and scientists of NATO nations. The mission of the Institute has always been to focus on research and training but also to support international cooperation. The Von Kármán Institute was established in October 1956 in buildings which previously hosted the aeronautical laboratory of the Civil Aviation Authority of the Belgian Ministry of Communications. Today the Von Kármán Institute is a centre of excellence in research on fluid dynamics structured in three departments: Aeronautics & Aerospace, Turbomachinery, Environmental and Applied fluid dynamics. The

Institute is founded by the Belgian Government and other international institutions and industries. It has about fifty different wind tunnels and specialized facilities for testing. A few among them are unique in the world. This Thesis has been elaborated during an internship in the turbomachinery department in the team of professor G. Paniagua.

1.2 Turbine unsteady flow measurements

Any turbine blade can be tested in a wind tunnel like a generic profile but many flow features cannot be reproduced in such way. For more accurate investigations, especially to take account of stator and rotor blade interactions, there are mainly three kinds of test facilities:

- linear cascades;
- annular and rotating continuously running test rigs;
- short duration test facilities.

Probes developed in this work are meant to operate in VKI CT3 short duration facility which belongs to the third categories. An extensive description of the facility and further references can be found in the PhD thesis of Persico [1] and in many publications of professors and researchers from VKI. The peculiarity of this kind of rig is that the desired flow conditions are established in a quasi steady state for a very short interval of time, namely a few tenths of a second. The rig has one and a half stage (stator - rotor - stator) and is capable to adjust Mach and Reynolds number independently. One of the most difficult engine phenomena to be reproduce in laboratories is the effect of heat transfer. The very high temperature of combustor exhaust gases cannot be replicated at reasonable cost in laboratories and would prevent the usage of many instruments which are very sensitive to temperature. Isentropic light piston compression tubes like CT3 have been developed specifically to tackle this problem. The driving force behind most of the heat transfer phenomena in fact is not the absolute temperature, but the temperature ratio, for example between the flow and the walls or blade surfaces. Since the duration of the test is very short, it is possible to impose a temperature ratio representative of real engine conditions. Basically this is done adjusting the temperature of the air blown in the facility. Local adjustments can be done also placing heating cartridge in selected locations of the facility. The overall apparatus allows boundary layer developments to be reproduced taking into account also the effect of heat transfer. The duration of the test is very short thus there is no chance to reach steady state temperature in the walls and blades. From measurements of transient temperature distribution in solid parts it is possible to measure the actual temperature ratio and the heat flux.

Many measurement techniques are applied in fluid dynamics, but narrow spaces, accessibility, mechanical stress and vibration effects of the rotating parts of the rig restrict the range of available methods for this application. Moreover, it is necessary to minimize flow disturbances introduced by instruments. For example less intrusive flow visualization techniques are very attractive in principle, but the need to provide optical access to the test section and to guarantee mechanical integrity limits their applicability. In rotating rigs the most common type of instruments consists of surface mounted sensors and several kinds of probes. Examples are given in figure 1.1 .

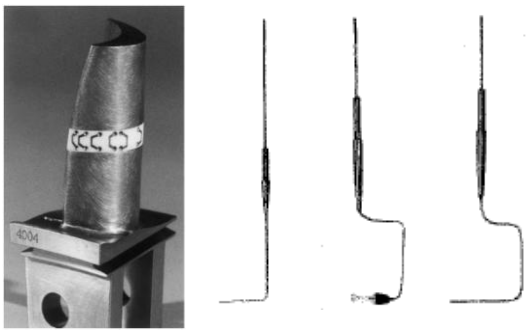

Figure 1.1. Examples of instruments used for measurements in turbomachinery. Left side is an example of surface mounted transducers for heat flux measurements on a turbine blade at VKI [2]. Probes on the right side are taken from [3]. It is interesting to notice that even the stem shape can be designed in different ways according to the required measurement.

The need for less intrusive instruments led to further and further miniaturization of probes over past decades. The second major issue in turbomachinery measurements regards the time response of the instrumentation. Flow in turbomachinery is characterized by many unsteady phenomena. The major unsteadiness is dictated by the effect of rotor blade passing frequency. In order to detect other relevant phenomena like shocks and secondary vortexes it is necessary to detect higher harmonics of the blade passing frequency. Thus instruments for turbomachinery have to be very precise but also capable to detect very fast perturbations occurring in the flow.

This work focus on pressure probes, which are fundamental tools for flow characterization, because from pressure field measurements it is possible to obtain major flow characteristics like velocity and losses.

1.2.1 Total pressure

The total pressure is defined as the pressure obtained by isentropically decelerating the flow to rest. For this reason it is also called stagnation pressure.

Application of Bernoulli's theorem along a stream tube, lead to the following equation:

$$\frac{v^2}{2} + gh + \int \frac{dp}{\rho} = constant \tag{1.1}$$

where v is the velocity, g is gravity acceleration, h might be seen as the height of the stream tube section measured above a reference point, p is the pressure and ρ is the density. Stream tube infinitely narrow can be considered as streamlines. Equation (1.1) can be seen as the relation between pressure and velocity along a streamline in inviscid flow. In most of the cases the contribution of gh is negligible with respect to the other quantities so it can be dropped and the equation should be considered valid for horizontal flow.
For low speed the flow can be treated as incompressible thus in case of horizontal flow, equation (1.1) takes the form:

$$\frac{1}{2}\rho v^2 + p = constant \tag{1.2}$$

which is the most common form of Bernoulli's equation encountered in practical works. Let p_0 be the pressure measured at a stagnation point (v=0) with the nose of a probe, equation (1.2) gives the total pressure of the flow before the probe was inserted in the stream:

$$p + \frac{1}{2}\rho v^2 = p_0 \tag{1.3}$$

The former is true if the probe is so narrow that only one streamline is brought to rest and viscosity effect is negligible, which is an ideal case. Experimental evidence reveals that the effect of viscosity is negligible except for very small probes working at very small velocity. Moreover variation of the size of the probe nose has small impact on total pressure readings if the probe is properly aligned with the flow. On the contrary, spatial accuracy is affected by the size of the probe. In case of compressible flow, for an ideal gas brought to rest isentropically, equation (1.1) takes the form:

$$\frac{v^2}{2} + \frac{\gamma}{\gamma-1}\frac{p}{\rho} = constant \tag{1.4}$$

where γ is the specific heat ratio and the contribution of gh has been neglected. Equation (1.4) is Bernoulli's equation for compressible flow which applies for both subsonic and supersonic flows provided that there are no shock waves. At a stagnation point, writing equation (1.4) in terms of Mach number (M) the total pressure is:

$$p_0 = p\left[1 + \frac{\gamma-1}{2}M^2\right]^{\frac{\gamma}{\gamma-1}} \quad (1.5)$$

Total pressure is related to the energy content of the flow and can be used to estimate losses in turbomachinery. Bernoulli's equation is a relationship between total pressure and velocity thus when total and static pressure measurements are combined together, it is possible to measure flow velocity. Thus an accurate total pressure measurement is a fundamental prerequisite for any flow field characterization. In case of subsonic flow, total pressure can be measured simply decelerating the flow adequately with the nose of a blunt obstacle. If the flow is supersonic, a bow shock is generated in front of the nose and a lower total pressure will be measured, because of energy dissipation through the shock. In Pitot tubes the total pressure is commonly measured through an orifice on the nose of a probe facing the flow.

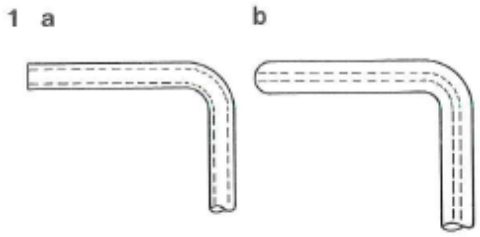

Figure 1.2. Common nose shapes for total pressure probes [3].

The stagnation pressure can be recorded with a sensor placed at the end of the pneumatic line or closer to the nose. With a remote sensor it is possible to build very small and robust probes since they are basically very tiny bent tubes. This is a great advantage for static measurements but a weakness for unsteady pressure measurements. Dissipation inside the line will damp unsteady pressure waves before they can reach the remote sensor. Thus in fast response probes the transducer should be placed as close as possible to the orifice. This measurements technique greatly benefited from the miniaturization of semiconductor based pressure transducers. Very small sensors can be placed inside the probe, very close to the measurement point. Encapsulated sensors can also be immersed directly into the flow in what is known as a "flush mounted" configuration. An example of a flush mounted sensor is given in figure 1.3.

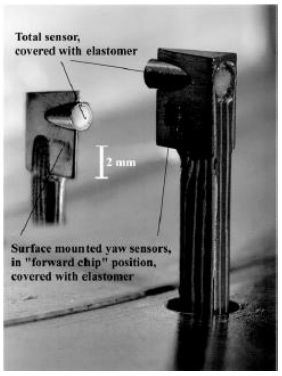

Figure 1.3. Three-sensor wedge probe of Oxford (Ainsworth *et. al.* 1994). In this probe three sensors are flush mounted, one on the wedge and two on the sides. [4]

Flow incidence influences significantly total pressure measurements, because it affects the position of the stagnation point on probes. For accurate total pressure measurements the probe shape should be designed in order to be less sensitive as possible to flow incidence. Noses of Pitot tubes are not very sensitive to angles of attack and several geometries have been developed. Among them extreme values of insensitivity are achieved with shielded probes (Kiel probes). With reference to the example depicted below angular insensitivity of configuration B (±23°) is double respect to case A (±11°) at M=0.26 according to [5].

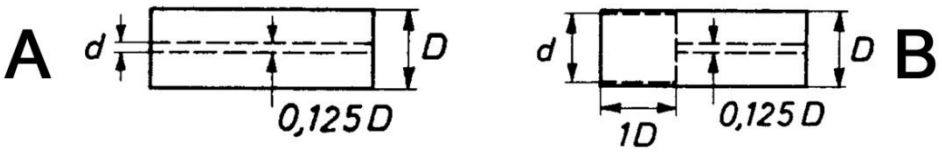

Figure 1.4. Common nose shapes adopted for total pressure probes. Orifice detail [4].

Total pressure can also be measured through holes placed on the side of a transverse cylinder. In this case, because of the curvature of the surface, incidence has a greater impact on the location of the stagnation point and thus on the total pressure measure. When flow incidence (yaw angle φ in figure 1.4) is null the stagnation point is located on hole which senses the actual total pressure.

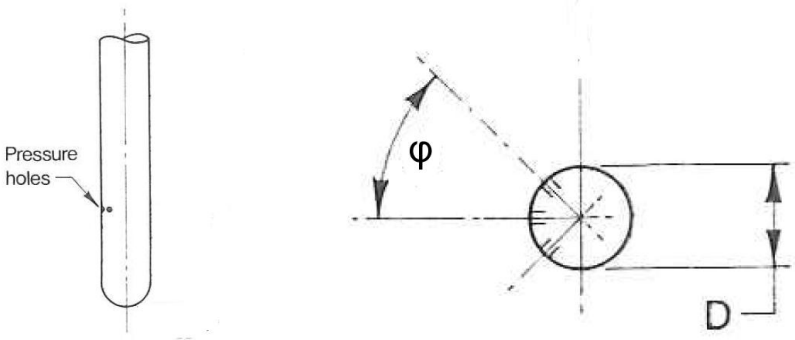

Figure 1.5. Transverse cylinder pressure probe, frontal and section view [4].

Extensive studies of the boundary layer demonstrated that in ideal conditions velocity is null only on the stagnation point. The presence of a pressure gradient in the boundary layer in fact accelerates the flow on the surface along the circumferential direction, from the forward stagnation point to the rear part of the profile. Moreover in real cases the condition of flow at complete rest on the stagnation point it is not achieved and must be seen as a limit condition being only approached.

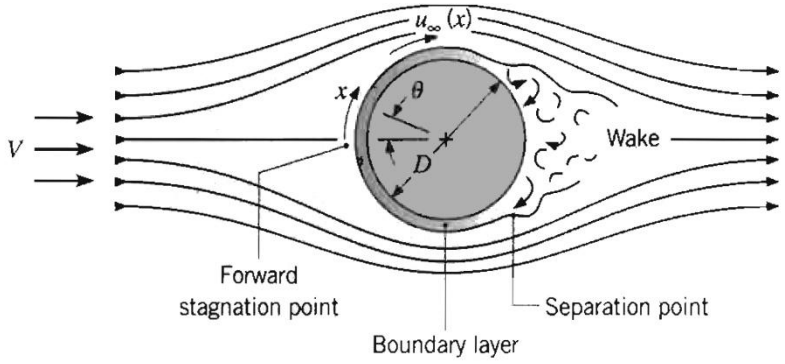

Figure 1.6. Sketch of the flow structure around a circular cylinder in cross flow [6].

For this reason total pressure measurements with transverse cylinder can be performed with same accuracy of other probes but in a more narrow range of incidence angles.

1.2.2 Flow angle

Along with total and static pressure, flow direction measurements are needed to describe the flow. When pressure distribution is known at certain locations on probes surface, since the geometry in known, it is possible to describe the surrounding flow field. For accurate directional information one pressure

measurement is not sufficient. Pressure probes with a symmetrical arrangement of sensing holes are generally adopted. There are two common ways to measure flow directions with them. In the "null reading" or "equibalanced method" the probe is oriented to a position that gives the same pressure reading for a pair of symmetrical holes. For turbomachinery applications, especially in the case of short duration facilities, this method is not suitable. The second method is to keep probes stationary and to reconstruct flow features through calibration coefficients. In this case, probe output must be fully characterized in controlled flow conditions. Calibration maps represent the functional relationship between pressure readings and can be interpolated to reconstruct the flow field during measurement campaigns.
Two dimensional flow measurements are possible using only two pressure ports. However it is quite common to include a third sensor to measure total pressure with the same probe. Multi-holes and multi-sensors probe are sometimes called combination probes. Several geometries have been developed and combination probes can have even five pressure ports. A few illustrative examples are given below in Figure 1.7.

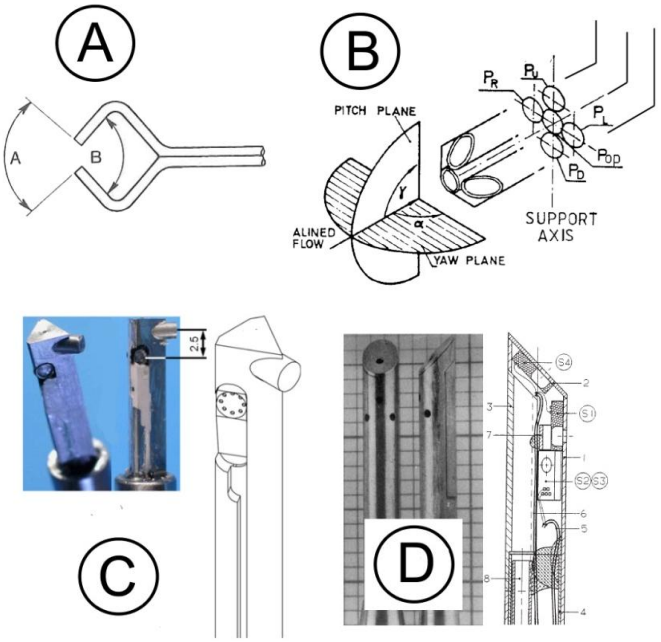

Figure 1.7. Examples of directional probes. A) Claw yawmeter [3] not suitable for measurements in turbomachinery. B) Sketch of the nose of a multi-hole directional probe with pitch and yaw directions [5]. C) 3-hole wedge probe for measurements in transonic turbomachinery developed at VKI by Delhaye. [7]. D) ETH 4-hole cylindrical probe of ETH Zurich [2].

The location of pressure ports should be defined accurately as a trade off between the necessity to reduce probe dimensions, the requirement of high spatial accuracy, and boundary layer effects. For example in the wedge probe depicted in figure 1.7 the flat sensor on the side wall is kept at a distance of 2.5 mm from the centre of the cylindrical total pressure transducer. This is to minimize disturbances generated by the upper transducers on pressure readings of the side sensor, but it is a disadvantage in terms of spatial accuracy.
An alternative approach in order to get multiple pressure readings with minimum probe dimensions is to use a single hole probe in a virtual multi hole probe mode. Kupferschmied *et. al.* present this technique in [8] while another example is given by Schlienger, Kalfas and Abhari in [9]. As depicted in figure 1.8 a three hole probe measure can be done combining a single hole pressure readings recorded at different times. Calibration maps and methods should be defined accordingly, and for accurate measurements the repeatability of flow conditions must be ensured. The probe is at a fixed location but it is turned of a certain angle around his axis between each measure.

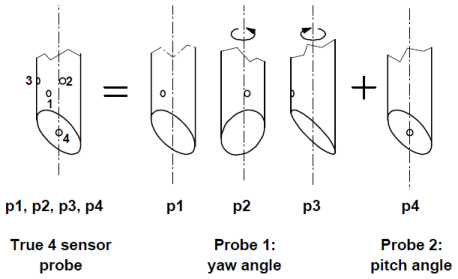

Figure 1.8. Measurement concept of a virtual 4 sensor probe. This example is taken from [9]. and is part of the FRAP® measurement system developed at ETH Zurich. Yaw angle is measured combining three readings from a single hole probe. In this specific case there is also a fourth measure for pitch angle.

In a similar manner in axial turbomachinery it is possible to combine measurements taken at different positions along the circumferential direction to reconstruct flow field characteristics. During the same test, probes at different locations face the same blade passing at different times. Adequate synchronization of the acquired signal and properly spacing between probes must be chosen. Additional considerations should be taken into account, but this is not the right context for an adequate explanation of the method. However it is worth to mention this possibility as it is of great interest for single hole probes application in turbomachinery.

1.3 Objectives and research methodology

The objective of this work is the development of fast response probes for total pressure and flow direction measurements to characterize the rotor flow field in a high pressure turbine stage. A single hole probe has been taken as reference design. The design has been revised in order to achieve further miniaturization and better performances.
In order to improve angular insensitivity for total pressure measurements, a very small shield is applied on a transverse cylindrical probe. Thus two different prototypes have been designed and manufactured. In subsequent chapters we will refer to the cylindrical probe as "the single hole probe" or the "normal probe", while the shielded configuration will be referred as the "Kiel probe".

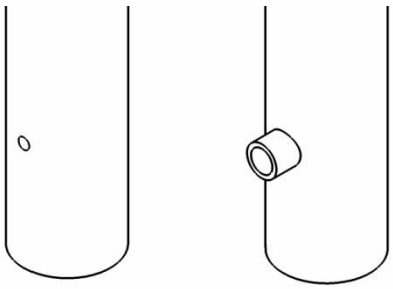

Figure 1.9 - The single hole cylindrical probe and the corresponding shielded configuration (Kiel) objective of the present study.

The choice to try to use a transverse cylindrical probe for total pressure measurements instead of a flush mounted transducer or a Pitot tube is dictated by two reasons. The first is the better aerodynamic, especially because the flow direction changes continuously in turbomachines, and the second is the better spatial resolution. A rigorous definition of spatial resolution of aerodynamics probes is not straightforward. However it is quite intuitive that a flush mounted transducer facing the flow like the ones depicted in figures 1.3 and 1.7 will sense a total pressure averaged on his frontal surface. The order of magnitude of spatial resolution would be the sensor diameter. For the single hole transverse cylinder, the spatial resolution is related to the hole diameter while for the Kiel probe it is dictated by the shield diameter. Taking as an example the sensor adopted in this work, the order of magnitude of spatial resolution would be 1.47 mm for flush mounted application, which reduce significantly to 0.55 mm and 0.2 mm when sensor is placed inside the transverse cylinder.
The preliminary design of probes is described in chapter 2 using an analytical approach.
Beside the probe development, a method to assess convergence in unsteady simulations originally proposed for turbomachinery have been extended to a

general unsteady solution and applied in this work. Chapter 3 explain this strategy while in Appendix A the implemented Matlab® script is reported.
Probe performances and aerodynamics have been investigated with numerical modelling presented in chapter 4. Grid dependence has been assessed with sensitivity study and a method to estimate uncertainty is applied. By computational fluid dynamics flow around probes profiles has been modelled, according to expected conditions in the facility. The impact of the Kiel on the angular insensitivity is evaluated. Vortex frequencies and their impact on pressure readings have also been taken into account.
In chapter 5 results from preliminary experiments are given and overall conclusions on the present work are summarized.

Chapter 2

Probe design

The design of instrumentation for fluid flow measurements is subjected to many requirements. Every instrument is characterized by a proper range representing limits for the instrument usage. Outside the proper range measures could be affected by errors, and the instrument itself can suffer irreversible damages. Thus the first step of the design should always be the definition of flow conditions the probe will be operating into. In this chapter, operating flow conditions are outlined, then the probe geometry is optimized. The final step is to verify that mechanical stress will not affect probe integrity and measures.

2.1 Turbine flow conditions

Probes developed in this work will serve for the aerodynamic characterization of a high pressure turbine stage tested in a transient rotating turbine rig. Real engine flow conditions should be scaled accordingly while geometry similarity keeps flow angles constant.

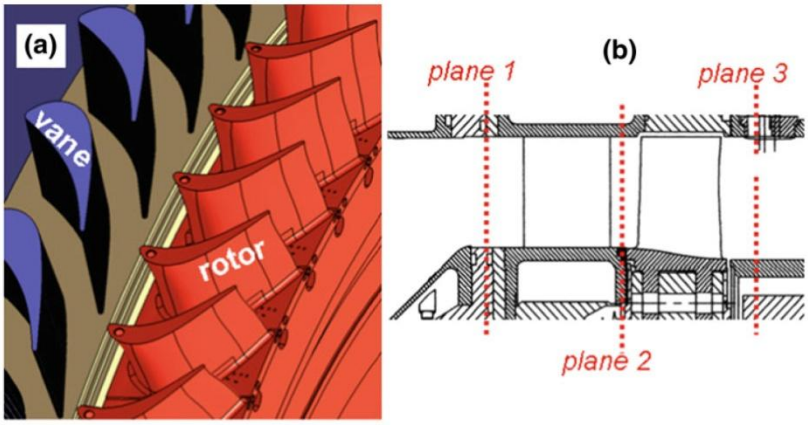

Figure 2.1. Compression tube rig used for turbine testing. 3-D (a) and meridional (b) view of a turbine stage investigated in CT-3 in previous test campaigns [7].

The CT-3 facility allows adjusting independently Mach (*M*) and Reynolds (*Re*) numbers which are maintained at the value expected in the engine. Total pressure and temperatures ratios on the stage are also maintained.

Table 2.1. Range of variation and mean values of flow characteristics expected in CT3 on the measurement plane.

	min	max	mean
T_{TOT} [K]	315	415	365
P_{TOT} [bar]	0.42	0.50	0.46
T_{STAT} [K]	314	395	359
P_{STAT} [bar]	0.42	0.43	0.44
ρ [kg/m^3]	0.465	0.375	0.426
M [m/s]	0.05	0.5	0.275
V [m/s]	17.8	199.1	104.4
Yaw [°]	-90	45	-22.5
Pitch [°]	-90	30	-30
$\rho \cdot V/\mu$ [m^{-1}]	$1 \cdot 10^6$	$6 \cdot 10^6$	$3.5 \cdot 10^6$

2.2 Design requirements and constraints

Every probe has to deal with constraints depending on the specific application. As sketched in figure 2.2 the probe is mounted on a stem to be hold inside the investigated flow region. The test environment (the turbine rig in our case) needs to be accessible accordingly through holes drilled in the external casing.

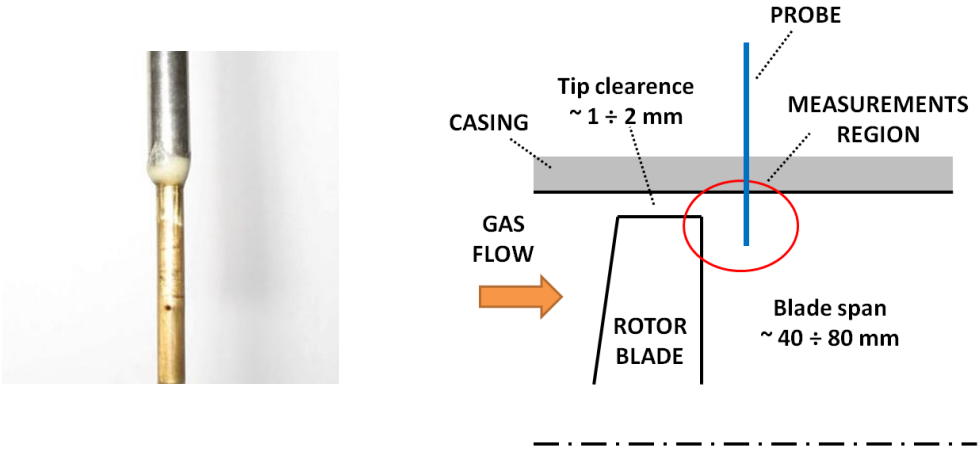

Figure 2.2. Left part: single hole pressure probe developed at Politecnico di Milano (CYL-2b) [10]. Right side: sketch of the measurements region and probe position in the turbine rig.

The overall assembly must also satisfy mechanical requirements and especially allow a proper orientation of the probe tap with respect to the flow. Once the small head of the instrument is mounted on a cylindrical long stem the probe can be introduced inside the test rig through simple holes drilled in the external casing (see figure 2.2). To ensure proper orientation of the pressure tap in the rig, a reference must be placed on the stem which can be easily rotated from the outside. Connection between probe head and stem must ensure coincidence of symmetry axes of both parts. The stem must be empty in order to allow sensor cables to be accessible from the outside. In case of classic Pitot probes, hole sizes on the rig casing and stem curvature must permit the introduction of the probe assembly. The probe depicted in the left side of figure 2.2 is a cylindrical single hole pressure probe developed at Politecnico di Milano (CYL-2b). For this probe, extreme small dimensions and the location of the pressure port on the side make none of the aspects mentioned critical. Even the introduction of the Kiel shield on the pressure port would not represent a problem when the probe need to be mounted on the facility. The Kiel length is much smaller than the stem diameter, thus it can still pass through a cyrcular hole. This is another operating advantage of this configuration respect to a classic Pitot probe. Besides that, robustness, simplicity and low manufacturing cost define the frame of possible geometries and design alternatives.

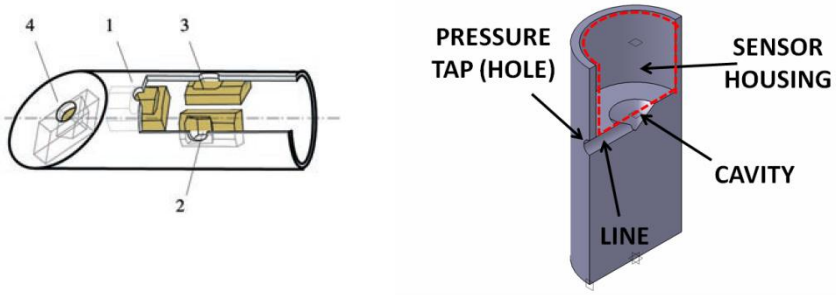

Figure 2.3. Left side: detail of sensors mounting inside the four hole pressure probe developed at ETH Zurich [11]. Right side: Politecnico di Milano (CYL-2b). Detail of the geometrical configuration adopted for the single hole probe developed at Politecnico di Milano.

Many probes are manufactured fixing extremely small and fragile transducers in very little gaps with great care and precision. This is done in order to keep the transducers as close as possible to the hole and perpendicular to the flow entering the line. The manufacturing cost increases and probes are inevitably very delicate. Compared to them the single hole probe developed at Politecnico di Milano show higher robustness and simplicity. As depicted in figure 2.3 the cylindrical sensor is placed vertically with the sensitive membrane facing a conical cavity, connected to the exterior through a cylindrical pneumatic line.

The presence of the line and the cavity introduce a damping effect on the pessure perturbations which pass through the hole. The most challenging part of the manufacturing is the probe head. Line-cavity dimensions are extremely small and the wall surrounding the sensor must be long enough to hold it. Its thickness should be as small as possible to minimize the overall probe diameter; surfaces must be smooth and without burrs. Manufacturing tolerances and imperfections can affect sensibly probe performances leading to measurements errors. Moreover, sensor insertion and sealing should be done with extreme care and just by expertise. Too tight fixing could cause mechanical stress on the sensitive membrane. Bad fixing could allow leakages that would alter inevitably the pressure sensed by the transducer.

Major constraints on the design depend from the sensor. Further information about available technologies and their use in fast response pressure probes can be found in literature [1] [4] [8] [11] [12]. There are also remarkable applications of miniaturized sensor developed for biomedical applications [7] but manufacturing cost and robustness of commercially available miniaturized pressure transducer make them the best choice for our application.
In this work the probe developed at Politecnico di Milano has been considered as a reference design of a miniaturized pressure probe proposed by Persico *et. al.* [13] for further probe development. The attempt to improve it should begin from the sensor choice.

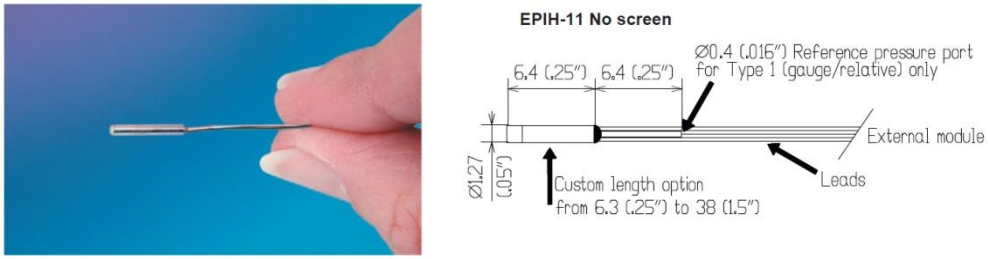

Figure 2.4. Miniaturized encapsulated pressure sensors. Left side: Kulite® XCQ-062 series. Right side: physical dimensions of Measurement-Specialities™ EPIH-11 without screen. Dimensions are given in mm (inches).

From a comparison of available technologies only one candidate has the potential to replace the Kulite® XCQ-062 Series for this application. Measurement-Specialities™ EPIH miniaturized sensors are very similar in dimensions and operating ranges. These very small sensors are silicon based transducers encapsulated in different compact packaging. The sensitive membrane is covered by a protective layer of polymeric material and usually it is placed behind an external perforated screen. In his configuration without the screen, EPIH-11 has an external diameter of 1.27 mm. This is less than 1.7 mm of the Kulite® thus there is a margin for probe external diameter reduction.

Pressure range is 1.5 bar (25 psi) based on expected turbine rig pressure level. Both sensors have a natural frequency above 100 kHz, which is high enough for the present application. Blade passing frequency (and the related pressure peaks) is approximately 7 kHz. The line-cavity acts as a low-pass filter with a resonant frequency which is desired to be as high as possible, potentialy in the range of 40 ÷ 50 kHz as reported in [13] and [1]. Even if the transducer has a higher frequency response, every frequency over this threshold will be damped by the line-cavity arrangement.
Once the sensor is chosen, for fast response measurements the line-cavity system is the critical aspect. Since the different diameter of the two sensors is a geometrical constraint, once the transducer is selected the line-cavity configuration can be designed based on the sensor geometry. The comparison should be done from this perspective, because sensors characteristics are similar.

2.3 Frequency response analysis

For the design of CYL-2b probe a few analytical and numerical models have been used to optimize the line and cavity dimensions [1]. The simplest approach leads to the Helmoltz equation which is subjected to this hypotesis:
- the fluid can be assumed to be at rest (though compressible) in the cavity, which is reasonable when the axial length of the cavity is negligible with respect to the line length;
- the flow in the line can be assumed to be incompressible which is reasonable when the line volume is negligible with respect to the cavity volume.
The damping effect of the line is computed with Poiseuille's formula for laminar incompressible flow, thus is related to the viscosity.
The above assumptions are not suitable for the geometries under consideration here. Thus, in the development of CYL-2b at Politecnico di Milano, a corrected lenght for the line has been introduced and a more accurate model ascribed to Houghen *et. al.* [1] was considered, to take account of the effect of the compressibility in the line, which might become important as the line volume is comparable with the line volume.
The model consists of two expressions which predict the natural frequency ω_n and a non-dimensional damping ζ:

$$\omega_n = \frac{c}{L\sqrt{\frac{1}{2}+\frac{V}{Vt}}} \tag{2.1}$$

$$\zeta = \frac{16\mu L\sqrt{\frac{1}{2}+\frac{V}{Vt}}}{d_t^2 c\rho} \tag{2.2}$$

where V is the volume of the cavity, Vt is the line volume, μ is the fluid viscosity, c is the speed of sound and ρ is the fluid density. The tap diameter is d_t and L is the line length which is corrected in case of small line length using L_{corr} instead of L. L_{corr} is defined as:

$$L_{corr} = L + \frac{8}{3\pi} d_t \tag{2.3}$$

If we introduce the corrected length of equation (2.3) in equation (2.1) keeping the same notations and considering geometrical references from figure 2.4 after some algebra the resonant frequency (ω_n) equation can be rewritten as:

$$\omega_n = \frac{c}{\left(L^* - \frac{d_t}{2\tan\alpha}\right)\sqrt{\frac{1}{2} + \frac{\frac{\pi D^3 \tan\alpha}{24}}{\frac{\pi d_t^2}{4}\left(L^* - \frac{d_t}{2\tan\alpha}\right)}}} \tag{2.4}$$

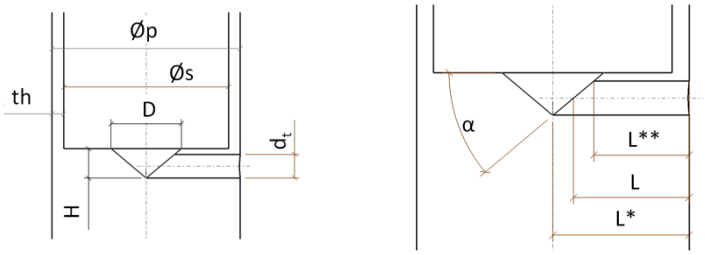

Figure 2.5. Section view of the probe head and geometrical references for optimization.
Left side: sensor diameter (*Øs*), probe external diameter (*Øp*), wall thickness (*th*) base diameter of the conical cavity (*D*), conical cavity height (*H*) cylindrical line diameter at the probe tap (d_t). Right side: detail of the line length. The line length *L* to be used for equations (2.1), (2.2) and (2.3) is defined as the midpoint between *L** and *L***. The conical cavity angle is *α*.

2.3.1 Geometry optimization

Dimensions of the line and the cavity have been optimized according to the analytical model that was found to be succesful in the original design. It has been retained reasonable to aply it again provided that the original shape of the cavity is maintained (cylindrical line and conical cavity) and just a few parameters are scaled. Equation (2.4) is a functional correlation between the frequency ω_n, the speed of sound c and four geometrically independent parameters.

$$\omega_n = \mathcal{F}(c, L^*, d_t, \alpha, D) \tag{2.5}$$

Assuming no gap between the sensor and external walls, the probe external diameter *Øp* is correlated with the sensor diameter *Øs* only through the thickness *th* :

$$L^* = \frac{\phi p}{2} = \frac{\phi s}{2} + th \tag{2.6}$$

If the thickness *th* is imposed (i.e. because of manufacturing constraints) and for a known speed of sound it is possible to optimize the geometry of the cavity and the line independently for both sensors just varying three geometrical parameters.

$$\omega_n = \mathcal{F}(d_t, \alpha, D) \tag{2.7}$$

The analytical model considered in the current analysis is based on global parameters (line length, line volume and cavity volume) but does not give any valuable information about the shape of the cavity. One of the peculiar aspects of Milano's CYL-2b probe is the innovative shape of the cavity, which reflects pressure waves on the sensor membrane. A thorough investigation would be necessary to properly describe the impact of the geometry, especially the effect of angle α on pressure waves propagation and reflection inside the cavity. In order to maintain the pressure propagation mechanism as similar as possible with the original design, the width of angle α is kept constant (≈ 37°). Thanks to the last assumption frequency can be optimized changing only two parameters thus the comparison between the two sensors will be clearer.

$$\omega_n = \mathcal{F}(d_t, D) \tag{2.8}$$

The reference case is D = 0.8 mm and d_t = 0.3 mm (original dimensions of CYL-2b). The thickness *th* is kept equal to 0.1 mm, which is a representative value for the mechanical feasibility limit. Under these assumptions, the effect of geometrical dimensions on the predicted frequency response for both sensors has been calculated and is reported in table 2.2.

Table 2.2. Optimization of line and cavity dimensions for two available sensors.

Metal thickness (*th*):	0.1 mm		
Conical cavity angle (α):	≈ 36.8 °		
Sensor:	**XCQ-062**		
Sensor diameter:	1.7 mm		
Probe external diameter:	1.9 mm		
$\omega_n=F(D, d_t)$ [kHz]			
	d_t [mm]		
***D* [mm]**	0.1	0.2	0.3
0.5	42.09	63.11	71.79
0.8	22.73	39.62	50.73
1.2	12.66	23.25	31.63

Metal thickness (*th*):	0.1 mm		
Conical cavity angle (α):	≈ 36.8 °		
Sensor:	**EPIH-11**		
Sensor diameter:	1.27 mm		
Probe external diameter:	1.47 mm		
$\omega_n=F(D, d_t)$ [kHz]			
	d_t [mm]		
***D* [mm]**	0.1	0.2	0.3
0.5	47.66	73.13	84.35
0.8	25.30	44.11	56.63
1.2	14.02	25.47	34.30

The predicted resonant frequency for the base case (XCQ-062, D=0.8 mm, d_t=0.3 mm) is higher than the value predicted for the original CYL-2b probe because of the higher speed of sound which account for 380 m/s in the present work. Results show clearly that in order to get a high resonant frequency it is necessary to increase the probe tap diameter and to reduce the cavity volume. In fact, smaller cavities are less affected by the periodic filling and emptying process due to pressure variations in the external flow field. When the flow in the cavity is at rest there are no viscous dissipations and pressure waves can travel across the medium with a smaller damping effect. The effect of probe tap diameter (d_t) is the opposite since a smaller diameter increases the dissipating effect of the line. The damping effect of the line is proportional to its length because it is mainly due to wall viscous stress. Since the smaller sensor allows reducing the external probe diameter, the line becomes shorter and for the same cavity diameter (D) the resonant frequency is higher.

Another geometrical feature to consider for geometry optimization is the angular span of the pressure tap with respect to the probe centre, which is a function of the probe radius of curvature ($L^*=Øp/2$).

The tap diameter d_t has to be chosen as a trade-off between frequency response and measurement spatial resolution which is better when the tap is small with respect to the curvature radius.

Table 2.3. Angular span for both sensors keeping the same material thickness and probe external diameters assumed in table 2.2.

Sensor:	**XCQ-062**		
d_t [mm]	0.1	0.2	0.3
angular span [°]	6.0	12.0	17.9

Sensor:	**EPIH-11**		
d_t [mm]	0.1	0.2	0.3
angular span [°]	7.8	15.5	23.1

From results shown in tables 2.2 and 2.3 it is clear that the smaller sensor have a potential for better performances. Keeping the same cavity volume, a reduction of the external diameter implies a shorter line length and thus a higher resonant frequency. In both cases a reduction of the cavity diameter *D* has a positive effect. A reduction of the probe tap diameter would decrease the angular span, but again this effect is partially attenuated for the smaller sensor.
From geometry optimization the choice is in favour of sensor EPIH-11 with a tap diameter of 0.2 mm and cavity diameter of 0.6 mm. For this configuration the predicted resonance frequency is 62.3 kHz.
The decision to reduce the cavity diameter (*D*) has to account for the physical structure of the sensor. The sensitive membrane faces the conical cavity from its base; therefore even though smaller cavities should approach the physical limit for fast dynamic response of the cavity, an excessive reduction of *D* is limited by the physical extension of the sensor sensitive area.

All aspects evaluated so far apply also to the Kiel probe configuration since it is just a variant of the cylindrical probe baseline. However, from a dynamic point of view the Kiel head is a cavity placed upstream the probe tap of the dynamic system investigated so far. This will affect inevitably the dynamic response of the overall system with an additional damping which will be quantified experimentally.

2.3.2 Design robustness

It is interesting to question the reliability of the model and assess its sensitivity to small variations of input parameters. Similarly it is possible to guess the impact of manufacturing errors on frequency response. First of all for the reference configuration the hypothesis of perfect coincidence between the sensor diameter (*Øs*) and the pocket drilled in the probe head is removed. A small gap is necessary to account for dimensional tolerances and transducer insertion. Even the metal minimum thickness can change according to technological

feasibility. Both considerations affect directly the line length and thus the frequency response. Five different configurations have been compared with the reference scenario. To account for the gap between sensor and probe head the sensor diameter in equation (2.4) has been increased to 1.3 mm and to 1.4 mm. Assuming 0.1 mm as the nominal thickness (*th*), all cases have been evaluated even for the worst scenario of 0.2 mm thickness.
Another effect considered is the impact of a 0.1 mm of additional depth for the cavity which could happen in two different ways (namely A and B in table 2.4) as sketched in figure 2.6 . Such eventualities will slightly affect also the line length, but its major impact is on the cavity volume. The last geometrical effect (table 2.4 case C) considered is a reduction of 50% in line volume which could happen if its diameter (d_t) decrease of approximately 30% or if the line will not be properly aligned with the cavity. In the latter case however, it is more likely that pressure waves propagation mechanism would change significantly and the analytical model would fail a priori to represent properly the dynamic characteristic of the line-cavity system.
Results of the analysis are briefly summarized in table 2.4, both as absolute values and as relative variation with respect to the reference scenario (highlighted in bold in table 2.4).

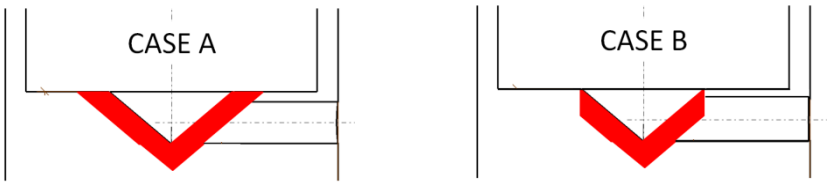

Figure 2.6. Impact of manufacturing errors on the cavity shape. The sketch highlights the additional volume resulting from an excess of 0.1 mm in cavity depth. Left side is representative of case A and right side of case B as described above in paragraph 2.3.2.

Table 2.4. Impact of mechanical tolerances and manufacturing errors on the predicted resonance frequency. On the left part of the table the frequency is correlated to the gap around the sensor and metal thickness *th*. On the right side, columns A, B, C refer to different scenarios explained above in paragraph 2.3.2 and depicted in figure 2.6. The relative impact is accounted with respect to the reference scenario of ω_{ref}=62.3 kHz. ($\Delta\% = \frac{\omega-\omega_{\mathrm{ref}}}{\omega_{\mathrm{ref}}} \cdot 100$)

Sensor: **EPIH-11** Conical cavity angle (α): ≈ **36.8** ° *D*: **0.6** mm d_i: **0.2** mm										
					A		B		C	
Øs [mm]	*th* [mm]	*Øp* [mm]	ω_n [kHz]	Δ%	ω_n [kHz]	Δ%	ω_n [kHz]	Δ%	ω_n [kHz]	Δ%
1.27	**0.1**	**1.47**	**62.3**	0.0	47.8	-23.3	44.8	-6.2	41.8	-6.8
1.27	0.2	1.67	58.1	-6.8	45.0	-27.8	42.3	-11.6	39.4	-12.1
1.3	0.1	1.5	61.6	-1.1	47.4	-24.0	44.4	-7.1	41.4	-7.7
1.3	0.2	1.7	57.5	-7.8	44.6	-28.4	41.9	-12.3	39.1	-12.8
1.4	0.1	1.6	59.5	-4.5	46.0	-26.2	43.2	-9.8	40.2	-10.3
1.4	0.2	1.8	55.6	-10.8	43.4	-30.4	40.8	-14.7	38.0	-15.2

We can conclude that even in worst cases the frequency does not fall significantly below 40 kHz, which is the lower limit desired for these probes. Results show clearly the additional damping when length line is increased because of an eventual gap around the sensor (*Øs*) or an increase in metal minimum thickness (*th*). Among others cases the most relevant impact is the additional volume of case A.

Many theoretical and numerical tools to extend this investigation could be applied, but the fundamental step of prototype manufacturing and testing would still be required to validate any theoretical design. Many factors could affect the behaviour of probes of such small dimensions, and taking account of all of them will not reduce uncertainty on the predicted response. A small gap, or a bad sealing of the sensor head could alter sensibly the volume and the geometry of the pneumatic system. After prototype testing will be possible to update the design and reconsider all assumptions made for prototypes manufacturing.

2.4 Aerodynamic design

In his PhD Thesis Brouckaert [14] has deeply investigated aerodynamic effects on pressure probes. A clear synthesized description is available also in [1] while considerations on different approaches and trends in probes aerodynamic design

at the beginning of 2000 can be found in [15]. For the scope of this work just a few basic concepts are worth to be mentioned.

As outlined by Kupferschmied *et al*. in [11] the main goal of geometry design is to find a compromise between high sensitivity to flow angle variations in steady flow and small dynamic errors in unsteady flow. From an extensive research work it has been found that cylindrical probes are the less affected by dynamic errors. Influence to different Mach and Reynolds numbers is taken into account during aerodynamic calibration by definition of proper coefficients. From this point of view, cylindrical probes have been found to exhibit good calibration characteristics for Reynolds number (based on probe diameters) in the range of 10^3 to 10^5 and Mach numbers from 0.2 to 0.9 [11].
Beside cylindrical probes, wedge probes are very promising, especially in terms of angular sensitivity but they are strongly affected by dynamic phenomena like circulation-induced lift and dynamic stall which can alter significantly the measurement, especially in highly unsteady flows. This is relevant especially when they are not properly aligned with the flow direction. This weakness is crucial in turbomachinery measurements downstream of a rotor where flow angles change continuously. Together with already mentioned advantages, these aspects made the cylindrical shape the best for the present application.

The second relevant effect to be mentioned is the blockage. Any probe interacts with the flow which is immersed into, and its presence imposes variations in pressure distributions and Mach number of the flow. In order to evaluate the blockage effect it is necessary to compare the frontal area of the immersed probe with the flow channel area. In turbomachinery measurements, probe blockage effect must be evaluated with respect to blade height and pitch, which define the flow channel area. Usually blockage is due mainly to the presence of the stem, while the probe head has less influence because of its smaller dimensions. However in case of measurements close to the end wall of the rig (or a generic channel) the impact of head dimensions is of primary importance. Moreover close to walls additional effects due to the boundary layer and the presence of high velocity gradients affect the pressure distributions on the probe introducing further errors in the measured quantities. Beside the diameter reduction which has been discussed already, the last dimension to be defined is the distance of the pressure tap from the tip of the probe head. About pressure ports, Bryer and Pankhurts [3] suggest to keep the ratio between tap diameter (d_t) and probe diameter ($Øp$) below 1/3 which is satisfied in our case. The same work states that when the same ratio is below 1/12 the tip shape has negligible impact on calibration if holes are positioned at a distance of twice probe diameter or more from the tip. This criterion does not hold in the present case. In Persico's PhD thesis [1] it is remarked that in case of CYL-2b, the tap distance from tip was 5 mm in order to make the probe insensitive to pitch angle variation of ± 10°. The

probe developed during this work is intended for measurements close to the rig casing where its head can alter significantly the flow. Thus the decision is to reduce distance between probe tap and tip head at 2 mm to minimize probe intrusivity. This choice seems to be in agreement with similar applications depicted in Figure 2.7 [8]. Although in the referred paper probe tap locations are not discussed, it seems clear to be approximately 2 mm thus we can retain our assumption reasonable. After prototype testing additional insights could lead to better evaluation for this parameter. Pitch angle sensitivity and related calibration coefficient will state the success or the failure of our decision.

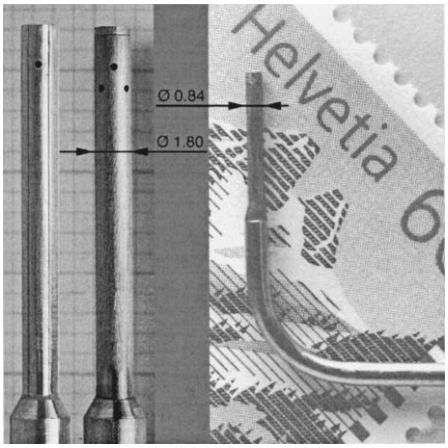

Figure 2.7. Miniaturized fast response pressure probes developed at ETH Zurich. Among the smallest probes in the world they represent a remarkable example of state of the art instrumentation for measurements in turbomachinery [8].

Concerning the Kiel configuration, probe aerodynamic issues are not clear. The proposed geometry is innovative therefore to the best knowledge of the author there are no relevant references in the open literature. Some design criteria for Kiel head are available in [3], [16], [5] but all of them have been developed and derived from classic Pitot tube, which are bent tubes aligned with the flow direction. In this case the Kiel head is mounted on a transverse cylinder probe which has a completely different boundary layer.
The simplest Kiel shape is a cylinder mounted on the front of the pressure port, as already anticipated. For most cases and shapes it has been found that total pressure readings become less sensitive to yaw when the ratio of the orifice diameter ($Øk_i$ in our case) to the tube diameter ($Øk_e$) increases. A graphical correlation is given in figure 2.8.

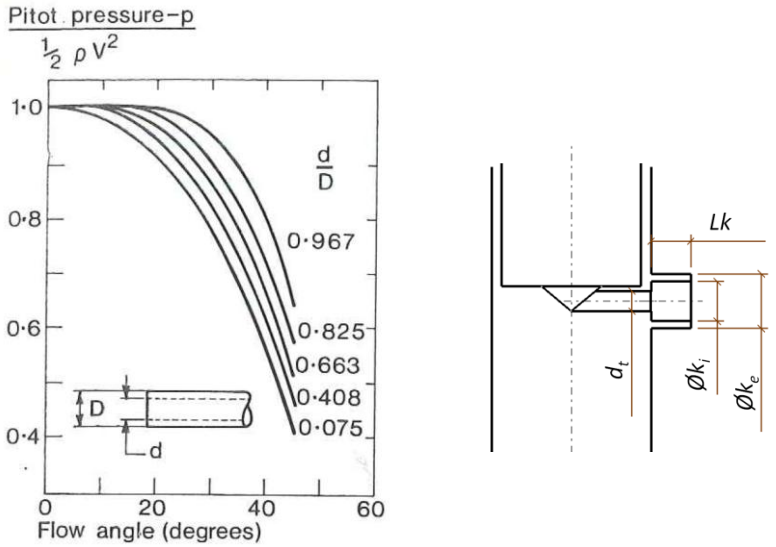

Figure 2.8. Left side: effect of flow angle on cylindrical ended tubes [3].
Right side: dimensions references used in the present work.

Assuming a Kiel thickness (th_k) of 0.075 mm with an internal Kiel diameter ($Øk_i$) of 0.4 mm the external Kiel diameter ($Øk_e$) is 0.55 mm. The $Øk_i/Øk_e$ ratio is 0.727. Guidelines for the shield length (Lk) are even more scarce, and there is no clear evidence about a unique criterion for the proper recess of the sensor. Different recommendations are given in [2] where different optimum ratio $Lk/Øk_i$ is reported, ranging from 0.2 up to 1.

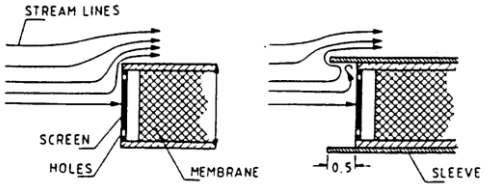

Figure 2.9. Sketch of sensor recess from the probe mouth taken from [2].

Moreover the completely different geometrical configuration, make this recommendation (usually adopted for Pitot tube) questionable for our application. The idea behind it, is that we can compare the pressure port (the hole on the cilinder) to the sensitive membrane of a Pitot tube as depicted in figure 2.9. The pressure that reachs the transducer travelling through the line-cavity arrangement is related to the pressure on the external hole surface. Thus if with a shield it is possible to keep tha stagnation pressure insisting on the hole as close as possible to the stagnation pressure for a wider angular range, the probe should be more suitable for total pressure measurements. The criteria adopted for the definition of the shield length should be looked from this perspective. In this sense the Kiel lenght can be seen as the recess of a sensitive membrane (the

hole) from the probe mouth. For the present prototype the shield length is chosen to be equal to the internal Kiel diameter. A simple parametrical analysis has been done with CFD simulation.

The last aerodynamic effect to be mentioned here is the effect of viscosity on the Kiel head, known also as the "Barker effect". [5]
At low Reynolds number friction close to the stagnation point can change the pressure distribution leading to a higher total pressure measured by the probe. The effect has been investigated by several authors and results for common shapes are presented again in graphical forms like in figure 2.10.

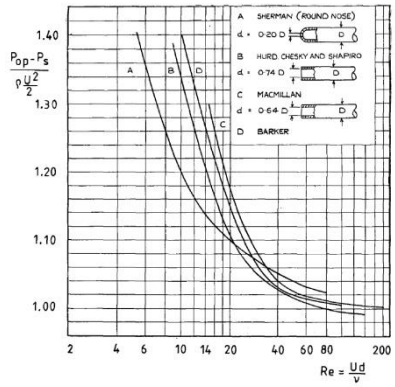

Figure 2.10. Effect of viscosity on total pressure measurements. [5].

A Reynolds number based on the Kiel diameter in the expected operating condition will be above 700, far away from the region of viscosity influence.
However when measurements are taken very close to the casing wall, this effect might be no more negligible and special care should be taken in data post processing and interpretation.

2.5 Prototype geometry

In previous paragraphs a few aspects regarding probe design have been considered critically. According to them a preliminary prototype design for the probe tip has been defined. Electro discharge machining (EDM) has been selected to manufacture the miniature probe head with acceptable tolerances and manufacturing costs. Nominal tolerances are stated by the manufacturer to be ± 0.01 mm. The total length of the probe head is 25 mm and for 5 mm it will be inserted in the stem which is 100 mm long. Final dimensions and a section view of both probes are given in figures 2.11 and 2.12.
It has been decided to:
- leave 0.05 mm of material between the line and the sensor housing;

- slightly open the cone angle in order to keep D = 0.6 mm and the centre of the cone coincident with the line end.
The predicted resonant frequency is 56.2 kHz.
The same geometrical configuration has been adapted for the Kiel probe.

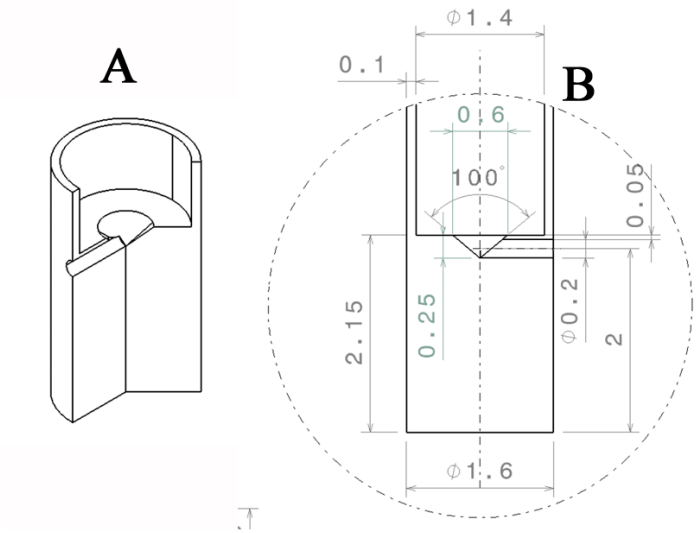

Figure 2.11. Single hole probe prototype tip detail.
3D section view (A) and tip dimensions given in mm (B).

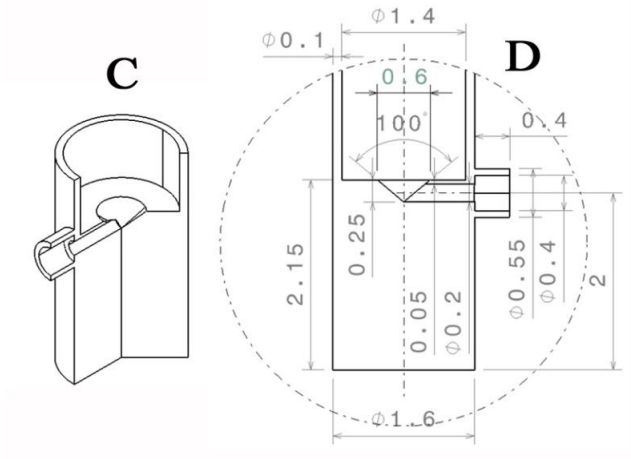

Figure 2.12. Kiel probe prototype tip detail.
3D section view (C) and tip dimensions given in mm (D).

2.6 Mechanical analysis

Every probe undergoes mechanical stresses when operating. The air flowing exerts drag force on the instrument and vibrations are induced by aerodynamics

effects (vortex shedding). Probe deformation may affect significantly the sensor performance in operation. An estimate of maximum deflection is given considering the maximum immersion of the probe in the flow during the test campaign.
The probe head acts like a cantilever beam with uniform distributed load.

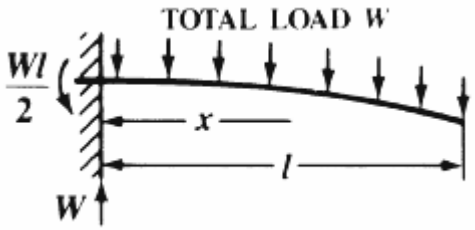

Figure 2.13 . Cantilever beam with uniformly distributed load. [17]

In this case the maximum deflection ($\delta_{\max}$) occurs at the probe tip:

$$\delta_{\max} = \frac{Wl^3}{8EI} \tag{2.9}$$

while the stress at the support is:

$$s = \frac{Wl}{2Z} \tag{2.10}$$

if the cross section is constant this corresponds to the maximum stress.
In equations 2.9 and 2.10 *E* is the modulus of elasticity (N/m^2), *I* is the moment of inertia (m^4), *W* the total load (N), *s* the stress at the cross section (Pa), *l* is the length as indicated in figure 2.13, and *Z* is the section modulus of the cross-section of the beam (the ratio between the moment of inertia and the distance from neutral axis to the extreme fiber, which is the external radius of the beam in this case) [16]. The maximum loading occurs when the whole head is immersed in the flow, namely when the beam length is 20 mm.
From CFD modeling the drag force (*Fd*) over the cylinder profile has been estimated to reach a maximum of approximately 0.005 N on a 1 mm long profile. Let *dl* be the length of the modeled profile. The total load *W* is:

$$W = \frac{Fd}{dl} l = 0.01\ N \tag{2.11}$$

For a hollow cylinder (for 90% of the length it's empty) referring to notation introduced in figure 2.5 and prototype dimensions, the moment of inertia is:

$$I = \frac{\pi(\emptyset p^4 - \emptyset s^4)}{64} = 1.331 \cdot 10^{-13}\ m^4 \tag{2.12}$$

Being the distance from extreme axis to neutral fiber *Øp*/2, the section modulus account to:

$$Z = \frac{I}{\emptyset p/2} = \frac{\pi(\emptyset p^4 - \emptyset s^4)}{32\emptyset p} = 1.664 \cdot 10^{-10}\ m^3 \qquad (2.13)$$

Material is stainless steel (type 316) whose modulus of elasticity is 200 kN/mm. Applying formulas 2.9 and 2.10 we get deflection at tip $\delta_{max} \approx 3.76$ μm and maximum stress at the support $s \approx 6$ MPa. Evaluation of stress support in this case is important to ensure integrity of the gluing between probe head and stem (0.2% yield stress of the steel is about 250 MPa). The order of magnitude of the stress has been retained below any critical threshold for glue employed in probes manufacturing. Major concerns were cast about Kiel probe configuration, since it offers a wider surface normal to the flow. For that case drag estimate from the 2D computational modeling are not representative of the reality because of the high asymmetry in real 3D pressure field around the whole probe. From this point of view simulations presented in chapter 4 could be seen as a limit case of maximum stress since the profile section is taken at the point of maximum Kiel external diameter. The worst case scenario modeled can be assumed the one with flow angle of 60°. In that case drag force is more than 50% higher respect to the normal cylinder. The above stated consideration about the stress magnitude does not change qualitatively thus more detailed mechanical stress analysis is not retained necessary.
Similar conclusions can be withdrawn for the maximum deflection. When deflection is high, an error in pitch angle is introduced. Luckily, probe head is very short and steel modulus of elasticity is high enough to get a negligible deflection for the present application.

Vibration of probe head causes spurious velocity components at the measuring orifices affecting the pressure measured. There is experimental evidence that, in adverse conditions, errors due to this phenomenon can be appreciable [16]. Error magnitude is greater in case of resonance between the exciting frequency and the natural frequency of the probe. The most relevant aerodynamically excited vibrations are due to the vortex shedding. In practical application resonance between vortex frequency and probe natural frequency is known to occur in water but it is less likely to happen in air measurements. Still an estimate of probe oscillating frequency is required because there are a few mechanical sources of vibration in the test facility. The probe natural frequency will be compared with results coming from test rig vibration analysis in order to minimize all possible error sources for the test campaign.

The probe head is like a beam with a fixed end and the tip free to oscillate. In vibration studies, mass distribution is a key factor. Since the probe head is empty the simplified representation of a massless beam with concentrated load at the end is suitable.

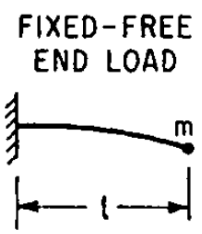

Figure 2.14 . Massless beam with concentrated load at the end. [18]

If we consider the total length l to be 20 mm, according to geometrical dimensions depicted in figure 2.11 assuming a steel density of 7990 kg/m^3 the mass distribution is known. From simple geometrical considerations, it can be demonstrated that 99% of total mass is concentrated at the end of the probe head, since the tip is full of material. Even assuming the empty part to be filled with 10 times the weight of a sensor (Kulite® XCQ-062 weights 2 grams) the mass at the end would still account for more than 94% of the total. Accordingly, the assumption of massless beam with concentrated load holds.
In such conditions, the natural frequency in Hz is given by:

$$\omega_n = \frac{1}{2\pi}\sqrt{\frac{3EI}{ml^3}} \tag{2.14}$$

Assuming the head mass is concentrated at l =18.925 mm using the inertia of the hollow cylinder section given in equation 2.12 the natural frequency would be 56.3 Hz. This value is expected not to affect significantly the time-resolved pressure measurements. This estimate confirms that structural vibration frquencies are always much lower that fluid dynamic oscillations.

Chapter 3

Unsteady CFD convergence: a multi-parameter approach

One of the fundamental aspects of CFD analysis is the definition of a proper convergence criterion. If the iterative method is converging, the difference between the actual solution and the solution from the previous iteration decreases with the number of iterations. To save time and resources, the iterative procedure should be stopped when residuals become sufficiently close to zero, accepting an approximate solution very close to the exact one. When residuals decay below a threshold of a few orders of magnitudes and do not show any further variation this condition is satisfied. However it is common to follow the good practice of monitor some relevant quantities meaningful for the specific problem instead of relying just on residuals. Observation of flow variables, which have a clear physical meaning, gives analysts the right perception of proximity to the exact solution. In steady state problems, is common practice to monitor quantities like pressure distributions around bodies or across specific domain sections for example, to verify if they look reasonable and fully established. For unsteady problems, the approach is slightly different, since flow variables are space and also time dependent, making profiles or local quantities comparisons harder. A common used approach is to compute integrated properties on a certain surface or domain section and monitor their evolution in time. For internal flow in turbomachinery for example one could monitor mass flow, pressure or Mach number across inlet and outlet sections of a passage, while for external aerodynamics usually analysts monitor quantities such lift and drag forces on profiles or the relative pressure fields. After a proper number of iterations their behaviour becomes periodic and solution can be deemed converged.

3.1 CFD convergence methodology

It is important to establish clear criteria to assess in a rigorous way the onset of convergence. Accurate estimation of achieved convergence is crucial especially to perform comparisons between different computations and minimize the overall computational time. This is of utmost importance in unsteady

computations, where the number of iterations increases significantly to solve time dependent discretized equations. In this work a methodology to assess convergence of unsteady numerical dataset is presented. The criteria presented here, is inspired to the work of J.P. Clark and E.A. Grover [19] from U.S. Air Force Research Laboratory and it was originally developed for unsteady convergence in turbomachinery. A few numerical parameters are combined together highlighting different aspects of unsteady flow field, giving the user a deeper awareness of unsteadiness characteristics, which in turbomachinery include several phenomena. Among the most relevant there are blade passing effect and wakes downstream airfoils. Although unsteady computations performed for this work are much simpler, the procedure presented in [19] is quite general in principle and its use can be extended to any time dependent quantity.

The principle of the method relies on the comparison between consecutive periods of any time varying variable. In order to properly assess unsteady convergence, both time mean and time resolved quantities should be taken into account. While it can be trivial to track time mean history over several periods it is not straightforward to discern whether an unsteady calculation is converged based on time-varying quantities. The proposed method combines together five different coefficients which characterize several aspects of flow unsteadiness. Convergence is reached when all parameters remain above a certain threshold. With this approach it is possible to quantify the similarity between consecutives periods by evaluating different features of time dependent signals. Here parameters definitions and meanings are reported and summarized briefly.

The time history of a variable can be divided in periods of constant length *T*. Let the step of the time discretization be Δt the total number of time steps per periods (*N*) amount to:

$$N = \frac{T}{\Delta t} \tag{3.1}$$

Once these three parameters are defined, it is possible to evaluate for each period a mean value, a cross correlation coefficient (CCF), perform a discrete Fourier transform (DFT) and calculate power spectral density (PSD). If we call q the generic variable being monitored, time mean value of q along a single period is:

$$\bar{q} = \frac{1}{N}\sum_{n=0}^{N-1} q(n+1) \tag{3.2}$$

For each time step the fluctuating component is simply:

$$q'(n) = q(n) - \bar{q} \tag{3.3}$$

The discrete Fourier transform (DFT) of the fluctuating component evaluated at an integer multiple (*k+1*) of the period frequency (*f*) is given by

$$P(k+1) = \sum_{n=0}^{N-1} q'(n+1)\, e^{-i\frac{2\pi kn}{N}} \tag{3.4}$$

where Fourier components are defined for values of *k* between 0 and *N-1*.
Each Fourier component is a phasor,

$$P(k+1) = Re + Im\, i \tag{3.5}$$

and it is possible to reconstruct time periodic fluctuation by means of:

$$q'(t) = Re\left\{Ae^{i(\omega t+\phi)}\right\} = Acos(\omega t + \phi) \tag{3.6}$$

where *A* is the normalized DFT magnitude, given by

$$A = \frac{2(Re^2+Im^2)^{1/2}}{N} \tag{3.7}$$

and ϕ is the phase angle defined as

$$\phi = arctan(\frac{Im}{Re}) \tag{3.8}$$

In equation (4.6), ω is the circular frequency corresponding to the integer multiple of the period frequency:

$$\omega = 2\pi f(k+1) \tag{3.9}$$

With reference to a general lag in time (*L*), a cross correlation coefficient can be defined as:

$$CCF(L) = \frac{\frac{1}{N}\sum_{n=0}^{N-1} q\prime((n+1)+L)q\prime((n+1)+N)}{\frac{1}{N}\left[\sum_{n=0}^{N-1} q\prime^2(n+1)\sum_{n=0}^{N-1} q\prime^2((n+1)+N)\right]^{1/2}} \tag{3.10}$$

The cross correlation coefficient can be computed for different time lag values. A characteristic of this parameter is to assume a maximum value of 1 when equal consecutive periods are compared with zero time lag (*L=0*).
When full convergence is obtained, mean value between consecutive periods should not change anymore, and the same should be true for the cross

correlation coefficient (*CCF*), constant and equal to 1 if *L*=0. The same holds for the amplitude and phase values of discrete Fourier transform. However, the DFT generates a spectrum of values for each period, not just a single number. The Fourier transform associates a complex variable to a real number therefore generating a vector with the same number of elements as the input data series. The smallest the discretization step, the highest the number of points per period (vector) and the highest the number of corresponding transformed phases and amplitudes. The discretization step size in the frequency domain is:

$$\Delta f = \frac{sampling\ frequency}{N-1} = \frac{1/\Delta t}{N-1} \tag{3.11}$$

Once some descriptors of each period are defined the procedure summarizes results using dimensionless parameters. Considering two consecutive periods, and referring to them with subscripts 1 and 2, the convergence indicators are defined as:

$$fM = 1 - \left|1 - \frac{\overline{q_2}}{\overline{q_1}}\right| \tag{3.12}$$

$$fA(k+1) = 1 - \left|1 - \frac{A(k+1)_2}{A(k+1)_1}\right| \tag{3.13}$$

$$fFI(n) = 1 - \left|1 - \frac{\phi(k+1)_2 - \phi(k+1)_1}{\pi}\right| \tag{3.14}$$

$$fS = |CCF(0)| \tag{3.15}$$

The last coefficient is the power spectral density fraction calculated as:

$$fP = \frac{\sum_{k_{expected}} PSD(k+1)}{\sum_{k=0}^{N-1} PSD(k+1)} \tag{3.16}$$

The power spectral density (PSD) at a given multiple of the period frequency is defined as the product of the Fourier component at that frequency and its complex conjugate divided by the number of samples, *N*. The coefficient *fP* quantifies the fraction of signal power contained in frequencies of interest with respect to the global signal discrete spectrum.
All five indicators provide a rigorous quantification of the convergence trend of a generic signal. Additionally careful analysis of these indicators may yield valuable information on specific characteristics of the unsteadiness. Especially in turbomachinery, unsteady CFD is a powerful tool that provides information regarding the flow physics. For example global performance and heat transfer phenomena are mostly related to time mean mass flow rates, pressure and

temperature distributions, while resonant stresses depend on unsteady perturbations.
fM, *fA*, *fP* give a clear picture of those characteristics, while *fS* is an indication of how alike are consecutive periods. The parameter *fP* provides information about the relevance of certain frequencies with respects to global unsteadiness. For example in turbomachinery CFD it might be that after some iterations major unsteadiness in the flow field, like blade passing effects is established properly and minor phenomena like vortex shedding at trailing edge are not yet properly modelled by the iterative computations or, likely, they appear at unexpected frequencies not searched for. Low *fP* values or a non constant value from period to period is a good indicator that claims for better observation of results.
It is possible to gather together convergence indicators and define a global convergence level by simply compare all of them and consider the minimum one.

$$fC = \min(fM, fA, fFI, fS, fP) \tag{3.17}$$

Since by definition all coefficients are complementary to unity, convergence is considered obtained when *fC* overcome a reasonable threshold which Clark and Grover [19] assume as 0.95.
This number is a clear indication of how much a period is different when compared with the next. For example *fM* >0.95 means that the mean value of period 2 differs from period 1 for less than 5%. The criterion allows quantifying differences between consecutive periods and monitor the trend towards full convergence that means all parameters (or *fC* if just the minimum of them is highlighted) tends asymptotically to unity as shown in figure 3.1.

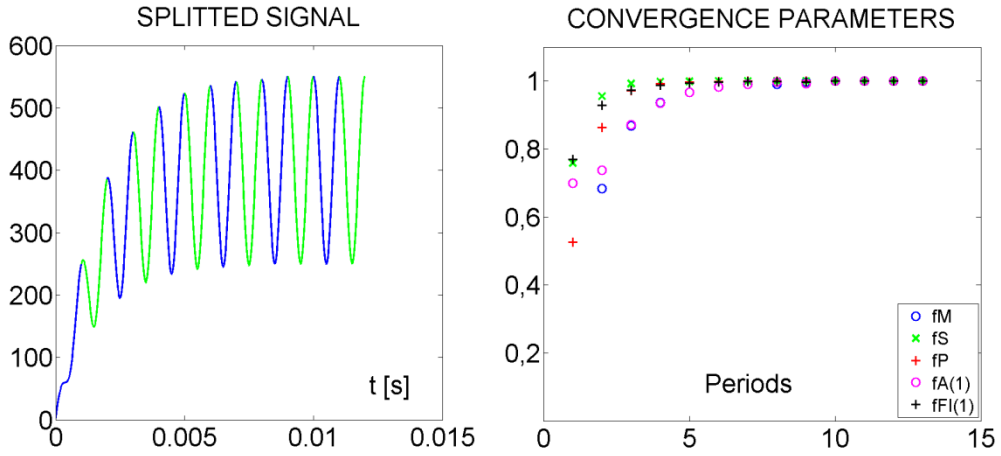

Figure 3.1. Example of convergence parameters trend with respect to unsteady iterations (time) on an artificial signals. After the transient all quantities tends to one.

In this example, convergence parameters are plotted together for an artificial signal. It is clear that after a transient part of the signal all parameters move towards unity. At this stage to keep unsteady computations running would represent a useless computational effort if relevant information will not change significantly from cycle to cycle. Numerical errors will still be present and affect the solution that is in general a discretized approximation of continuum phenomena. Thus it is almost impossible that parameters will ever reach unity like with ideal signals. This method allows to directly monitor convergence of a solution in terms of variables of interests, and to set appropriate quantifiers to rigorously assess convergence trends. It is common habit to judge convergence only based on visual inspections of plots or relying on analyst's experience. This method allows establishing a deterministic criterion, on which the user can set threshold level which represents adequate convergence.

3.2 Software for CFD convergence evaluation

Although the above explained procedure was thought for specific turbomachinery applications, the nature of parameters is far more general and applicable to any periodic signal and thus to any set of unsteady CFD computations. Part of this Thesis is devoted to the implementation of the procedure in a Matlab® routine for data reduction of unsteady CFD.

3.2.1 Routine implementation

In order to apply the convergence method to a general unsteady CFD problem, a routine has been developed and implemented in Matlab®. In turbomachinery unsteady CFD the most important flow unsteadiness is typically generated by the blade passage, whose frequency is known a priori and can be estimated from the rotor speed and blade count. Often it is also of interest the analysis of frequencies multiple of the fundamental engine order.

The method is capable of highlighting precise multiple frequencies of the engine orders but at the same time it can also highlight presence and appearance of non-periodic and periodic unsteadiness uncorrelated with the blade passing frequency. One of the main goal of turbomachinery designers in fact is to look in the signal to identify important imposed frequencies while keeping an eye on the overall unsteadiness of the flow. Their approach should be to implement the procedure in a proper routine where the period length is given as an input parameter and some precise multiple of the fundamental frequency have to be highlighted.

Instead, when the procedure is extended to a generic unsteady CFD solution (i.e. cases of chapter 4) the time scale of flow unsteadiness is unknown a priori. A typical example is vortex behind a blunt body. The appropriate time step can be set using an estimate of the Strouhal number which comes from experimental data and correlations. The exact frequency in the solution results from the iterative discretized solution algorithm and it is not imposed in the form of unsteady boundary condition, as it it occurrs for turbomachinery specific blade passing effect. This makes impossible to implement a routine capable to search for a priori known frequency values: they can be estimated to be in a certain bandwidth but remain unknown.
The same fact implies another relevant issue since the signal has to be split in periods whose length T will be known only when solution is converged and even then it will be an approximate value withdrawn from the solution itself. A priori the period length can be only estimated.
Consequences of this lack of knowledge will be clarifiedlater and explained with few examples. What is to be clarified before getting into details is that for a generalised use of the method for CFD calculations, the point of view must change and the implemented routine accordingly. The core of the process still remains the comparison of consecutive periods, computation of convergence parameters and output generation. It is necessary to implement a routine robust and flexible that allows user interaction to assess the unsteady frequency content from solution observation. So the resulting routine might be less automated and requires user's criticism.

Main steps of the algorithm are summarized in the diagram of figure 3.2.

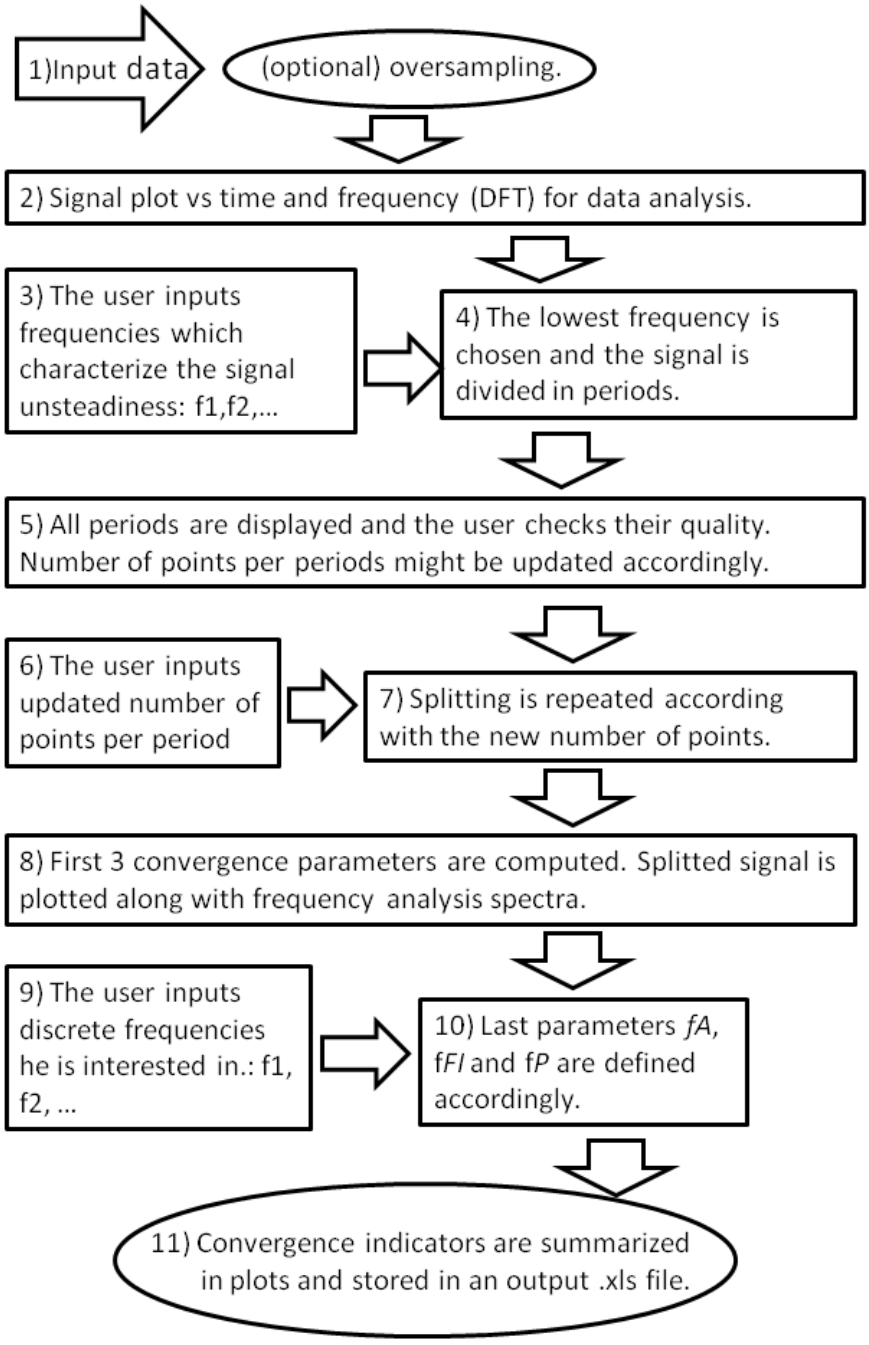

Figure 3.2. Flow chart of the unsteady convergence algorithm.

3.2.2 Software description

This section describes the relevant features of the software tool used for convergence analysis. The script is reported in Appendix A.
The routine requires an input file which shall contain the signal to process in function of time. Data must be gathered in column with no header. Folder path and file names for input and output must be properly adapted by the user.
The output generated by the script consists in three Matlab® figures and one .xls file. The output .xls contains the following data:
- original time step size of the data processed
- actual size of time step used for convergence analysis after oversampling
- actual number of samples per period used for the analysis
- period length and frequency
- values of *fM*, *fS*, *fP*, *fA*, *fFI* parameters. Parameters *fA* and *fFI* are reported along with the corresponding frequency for all discrete spectrum frequencies that best match values originally searched by the user.

Figure 3.3 shows the imported data series (left side) and the corresponding FFT amplitude spectrum (right side).

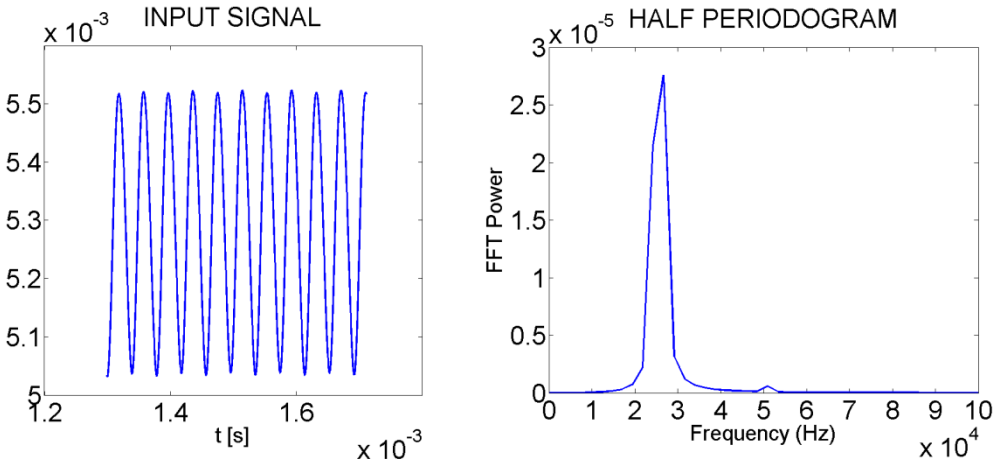

Figure 3.3. Example of the first output figure generated by the script. In this case the variable being processed is the drag force around a cylindrical probe profile taken at the end of a solution for approximately 400 consecutive time steps.

Figure 4.4 displays the split signal adopting two strategies. On the left part separated periods are plotted together, one after the other as they appear in the original signal. On the right side of the window, in a second plot, split periods are depicted not along the right time scale, but shifted to start all at 0 seconds coordinate. If the splitting procedure (the number of and corresponding period length *T* - or the frequency) is correct, equal periods (like in a perfectly

converged solution) tend to match perfectly, appearing as a single line or a very narrow stripe. Of course not converged solution, or periodical signal split erroneously depart significantly from this shape. The set of convergence parameters is generated using same data plotted in figures with different colours: bad looking plots imply not reliable convergence indicators.

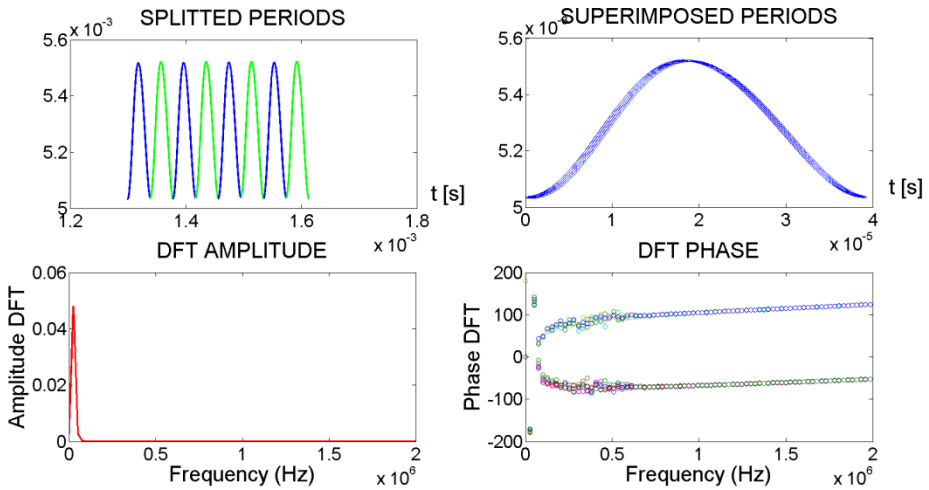

Figure 3.4. Example of the second output figure generated by the script. Data refer to the same signal shown in figure 3.3.

In the bottom part of figure 4.4, there are amplitude and phase spectra obtained via DFT of each period. Spectra generated via DFT for each period are plotted with different colours. From these plots, it is possible to read frequency values to use for calculate *fA* and *fFI* parameters. In turbomachinery unsteady CFD if the blade passing frequency is known and imposed, it is possible to select automatically the fundamental or higher harmonics and compute convergence parameters once this value is introduced at the beginning of a proper algorithm. Instead, in a general situation, frequency content of periods will be clear only at this stage. Even the fundamental frequency comes from the solution so in this sense the relevant frequencies are quantities a priori unknown.

Figure 4.5 shows all convergence parameters for all periods. In the top left there are only *fM*, *fS* and *fP*, while *fA* and *fFI* are displayed in the top right chart. Test of the routine on artificially generated signals revealed that it could be very helpful to separate *fFI* and *fA* in different charts when number of periods and frequencies selected increase. Moreover *fFI* and *fFA* could also manifest some fluctuations due to their sensitivity to the period discretization. The two lower charts address this issue: *fFI* and *fA* are plotted in separate windows to focus on the upper part of values range, above 0.85 where converged behaviour is of primary interest.

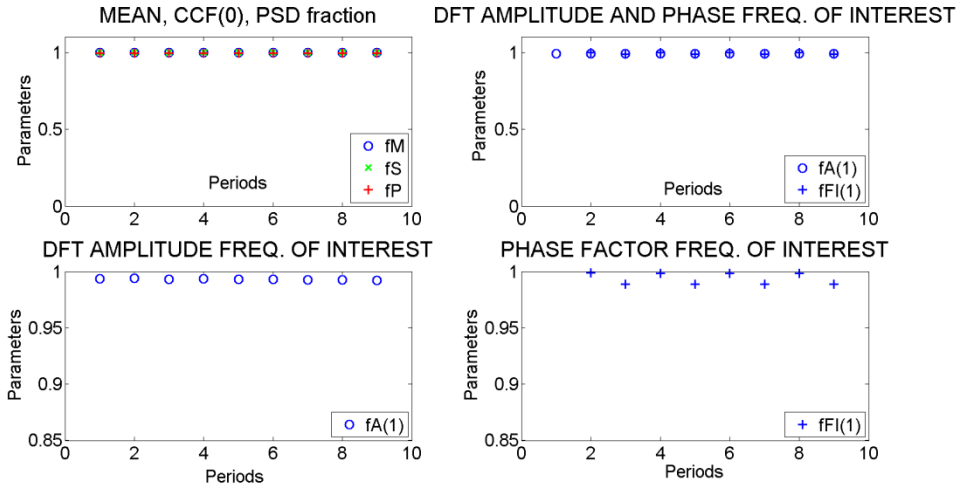

Figure 3.5. Example of the last output figure generated by the script. Data refer to the same signal shown in figure 3.3.

3.2.3 Potential pitfalls

It is worth to describe the role of interpolation introduced in the routine and some apparent pitfall of the method. The procedure has been initially implemented and based on artificial unsteady signals generated at the beginning of the script.

When a complex artificial signal is created from the composition of two sinusoidal traces it is possible to generate a time varying variable which after a certain number of points exhibits perfect periodicity. A typical example is reported in figure 3.6.

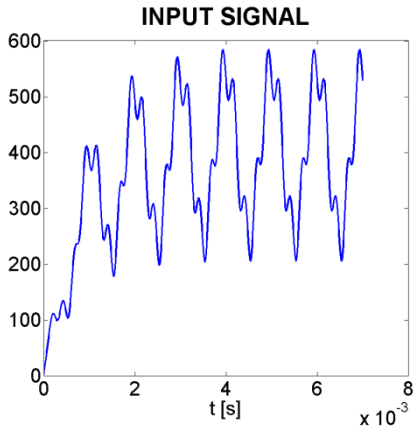

Figure 3.6. Artificial signal damped for the 55% of its length with an exponential function. After the transient the periodic signal is completely defined as:
$y = 400 + 150\cos(2\pi \cdot 1000 \cdot t + 0) + 50\cos(2\pi \cdot 4000 \cdot t + 2)$.

If the signal is divided properly, convergence indicators trend is correct: they start from low values (consecutive periods are very different from each other) and rise towards unity as clearly visible in figure 3.7.

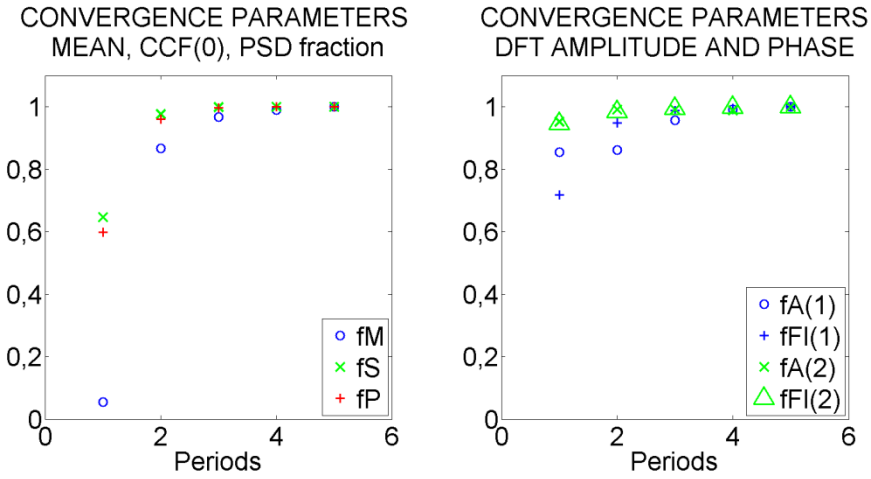

Figure 3.7. Convergence parameters for artificial signal of figure (3.6). On the left side *fM*, *fS* and *fP*; on the right side *fA* and *fFI*, for frequency values of 1000 Hz (1) and 4000 Hz (2).

In spite of the general good behaviour of the method, potential misleading pitfalls arise mainly in three situations:
- the period length is not an integer multiple of the time step;
- coarse period discretization (too few points per period);
- incorrect choice of frequency by the user.

In order to properly clarify the above statements, it is useful to give some examples. The first two aspects are very similar and basically they depend on the discrete nature of data processed. The first step in order to apply the procedure is to define the length of periods and split the signal accordingly. In order to do so, the size of the discretization step defines the length of the period or vice versa. Since discretization steps are discrete quantities and periods have to be defined by a finite number of intervals, the period length can assume values corresponding only to integer multiples of the discretization step. This basic mathematical concept is generally handled reducing as much as possible the discretization step size. Nevertheless the nature of numbers often manifests itself in an odd way. If the original frequency of the signal is for example 3000 Hz, the corresponding period length (T=1/f) will be an irrational number ($0.33\overline{3}\ ms$), therefore even refining a lot the discretization step it is not possible to split the signal in perfectly alike consecutive periods. This is clearly visible in figure 3.8 where the only difference between the two cases is the number of available discretization points (respectively 34 and 33). In this example it is not

possible to avoid a certain time shifting in the splitting procedure, which is reflected in convergence parameters, especially in *fFI* that for the 33 points example is limited slightly above 0.9.

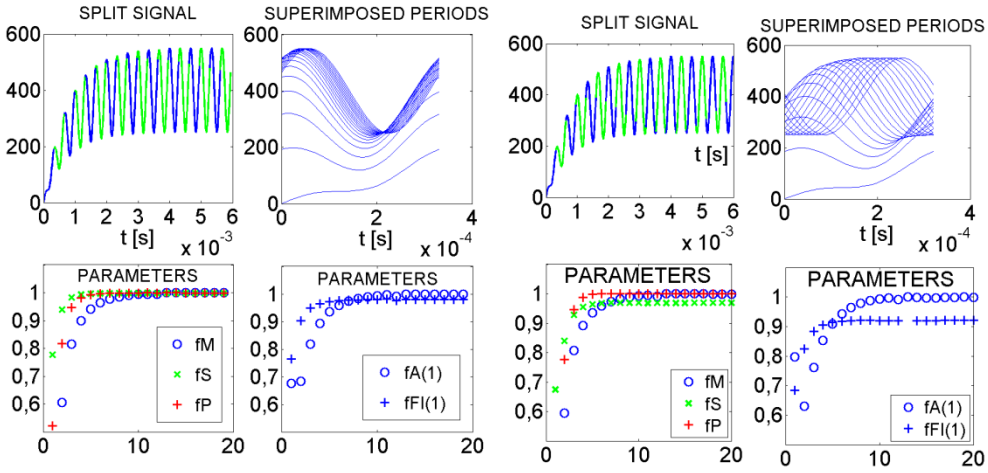

Figure 3.8. Routine test on an artificial signal defined as $y = 400 + 150\cos(2\pi \cdot 3000 \cdot t + 0)$ after the transient. Plots on the left side refers to the analysis with 34 samples per period, while on the right side points used are 33.

The possibility to discretize signals with submultiples of the period length has a non negligible impact on the maximum level of convergence indicators. It affects all indicators, but especially impact on DFT parameters, since they depend on a further discrete transformation of approximate periods. Even though the artificial signal is perfectly periodic phase amplitude parameters are below the convergence threshold of 0.95 (right side of Figure 3.8). It is possible to increase the method robustness by oversampling the original signal using interpolation between consecutive points. This strategy allows to reduce time shifting between separated periods improving convergence parameters. It is important to understand that oversampling data is a choice that should be done by the user on case-to-case basis to stabilize convergence indicators trend.
Moreover, user incorrect choice for the fundamental frequency may produce bad indicators. Although it is not a failure of the method it is worthwhile to clarify this aspect because sometimes it could be misleading and look as a pitfall. It is very important to select the proper frequency for signal splitting, which should be the lowest observed in the signal.
Signal represented in figure 3.9 for example apparently look like a ≈ 25.6 kHz signal, but this is not true. Slightly differences in minima and maxima values are visible between two consecutive periods, because the fundamental frequency in this case is the half: ≈ 12.8 kHz.

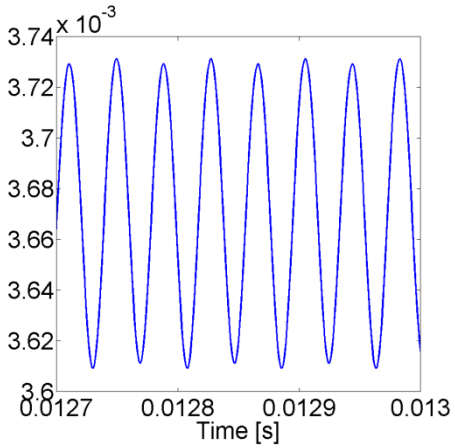

Figure 3.9. Detail of pressure integrated on the probe profile (raw mesh from grid sensitivity analysis) exhibiting a slightly non symmetric periodic behaviour.

It might be difficult to detect it even with Fourier analysis, especially if the first part of the signal is far away from convergence and so it generates low frequency peaks in the DFT amplitude plot. The user might not recognize at a first inspection the presence of a low amplitude fundamental frequency. Even though the power of the signal might be related mostly with a higher harmonic, the time periodicity is dictated by the lower fundamental frequency. In this case when convergence indicators are estimated with the wrong signal period length (corresponding to the higher frequency) they are lower (fig 3.10 - left side) but they improve with the right choice (figure 3.10 -right side).

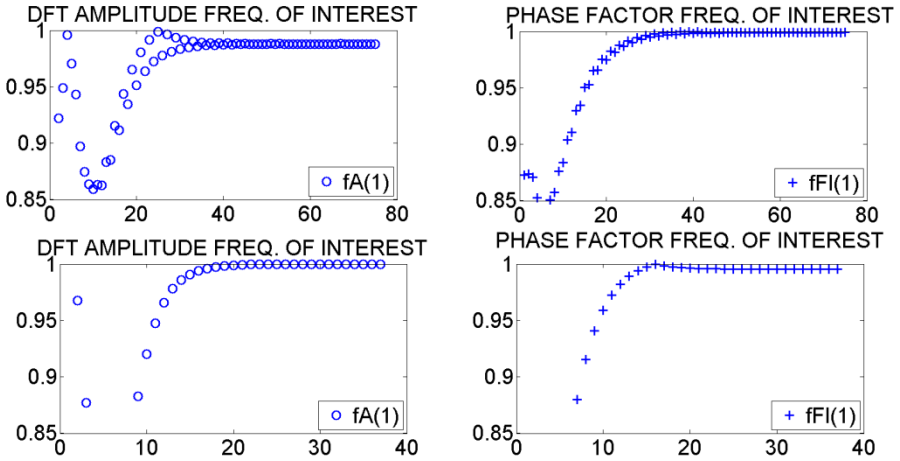

Figure 3.10. Comparison of convergence indicators for two different frequencies.

This critical aspect which might appear as a weakness of the routine instead is a user mistake which reaveals one of the strength of the method: it is capable to detect precise details of the unsteadiness in the flow, even for limit case like in the example above. It is interesting to note also that a warning "error message" is found when looking at convergence indicators plot. In fact although they have been generated for a single frequency they look like they were two different data series on the same plot. They are oscillating exhibiting a regular similarity between couples, not between single consecutive indicators. When such a trend is found, further investigation of lower (fundamental) frequency should be done.

Chapter 4

Probe performance: numerical analysis

Most of the available numerical tools to study fluids flow are based on the finite volume method, which is implemented in several computational fluid dynamics (CFD) software. In this work, CFD have been used to investigate probe aerodynamics in the expected flow conditions. Probe performances are estimated and the effect of the Kiel on the probe, especially in terms of angular sensitivity is evaluated through a comparison between the two probes. The accuracy of this numerical model in the prediction of probe performance will be assessed with a comparison with experimental results from probes calibration. CFD is used also as a support tool in the design process, to estimate optimal Kiel dimensions. The optimal criterion for spatial discretization has been defined with a grid dependence test. To assess convergence, the procedure explained in chapter 3 has been applied.

4.1 Flow physics

Probes developed in this work will be used for measurements close to the end wall of a turbine rig. The flow physics can be represented as a transverse cylinder in cross flow in the proximity of a solid wall as sketched in the left side of figure 4.1.

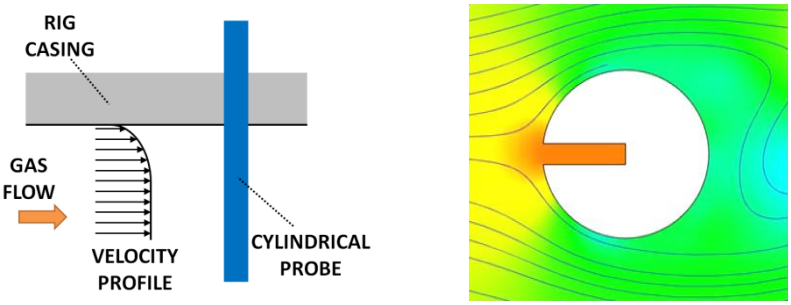

Figure 4.1. Left side: sketch of probe profile immersed into the flow.
Right side: section view of the probe profile at pressure tap location.

The real velocity profile is fully 3D and unsteady because of the passage of turbine blades. the endwall boundary layer and rotor tip leakage vortex. In wall proximity, viscosity effects due to the boundary layer are not negligible, and as mentioned in paragraph 2.4 the pressure port distance from the tip might affect

the pressure distribution on the probe tap. Vortex shedding induced perturbations on the cylindrical profile can travel upstream up to the leading edge of the probe [14], [20]. A two dimensional representation of probes cross section can provide insights about its effect on pressure readings. The section considered for the numerical model is the probe profile sketched in figure 4.1. Thus the complex three dimensional shape of the line and cavity arrangement is approximated with the axial section of a perfect cylindrical line. The pressure measured by the probe is estimated as the pressure obtained at the end of this line (please note that in this analysis the frequency response of the pneumatic system is not considered).
The problem can be regarded as the flow past a circular cylinder. Circular cylinders in cross flow manifest different flow configurations, which can be classified fairly well as a function of the Reynolds number:

$$\mathrm{Re} = \frac{\rho \mathrm{VL}}{\mu} = \mathrm{VL}/\nu \tag{4.1}$$

For the present investigation, probes operate in Reynolds numbers (*Re*) comprised between 1000 and 4000 (based on probe external diameter nominal Re is 3030). This corresponds to the flow regime illustrated in figure 4.2 [21] .

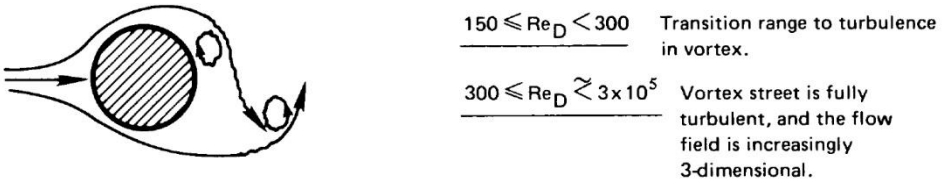

Figure 4.2. Circular cylinder in cross flow. Flow regime detail taken from Lienhard [21].

According to Lienhard, [21] [22] the laminar boundary layer on the profile separates from the surface at a point about 80° from the stagnation point. Flow regime is characterized by periodical release of turbulent eddies; therefore proper modelling should take account of the inherent unsteadiness of the vortex street. It is possible to describe the unsteadiness time scale of the flow, namely the vortex frequency, by another dimensionless parameter, the Strouhal number *St*.

$$St = \frac{f_v D}{u_\infty} = \mathcal{F}(Re_D) \tag{4.2}$$

Where f_v is the vortex frequency, D is the diameter, u_∞ is the characteristic velocity of the flow. The Strouhal number is correlated to the flow Reynolds

number based on the probe cylinder diameter (Re_D). The most common way to express the relationship between such non dimensional parameters is with charts derived from experimental investigations. Figure 4.3 which is taken from Lienhard [21] reports an example in of such $St=\mathcal{F}(Re)$ relationship. In a wide range of Reynolds numbers St is almost constant therefore the vortex frequency of the probe will be the same for a wide range of flow velocities. This is an advantage in probe signal processing and interpretation because a constant frequency component in the signal is easier to be indentified and filtered if necessary.

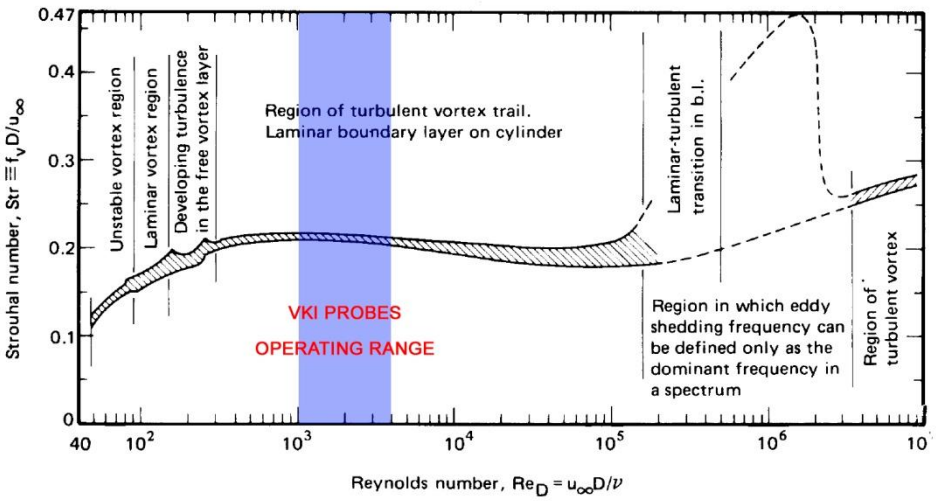

Figure 4.3. Strouhal versus Reynolds number. Different flow regimes around a cylinder. VKI probes operating range is highlighted in blue [21].

The Strouhal number is useful to estimate a time discretization step for the numerical problem. The time step should be small enough with respect to flow unsteadiness period. From Figure 4.3 we can assume a Strouhal number of 0.2. An alternative extensive review of Strouhal-Reynolds correlations is found in [23], where several detailed experimental studies are compared and a final analytical piecewise formula is given:

$$Sr = Sr^* + \frac{m}{Re^{1/2}} \tag{4.3}$$

Equation 4.3 is valid in the range 1300 < Re < 5000 assuming parameters Sr^*=0.2040 and m= 0.33624. For this case the resulting Strouhal number (Sr) is 0.21. The vortex shedding frequency, corresponding to Sr=0.21 is f_v = 14857 Hz. The associated time scale is:

$$T = \frac{1}{f_v} = 6.73 \cdot 10^{-5} \text{ [s]} \tag{4.4}$$

A good practice in unsteady CFD is to select a discretization step which is at least 1/20 of the period length [24]. In this case a time step of 10^{-6} seconds was chosen, which correspond to 1/67 of the vortex shedding period length. The selected time step is considered as a good trade-off between higher time resolution and increasing computational effort. Similar values have been used in an analogous investigation of a wedge probe external aerodynamics [7].

4.2 CFD modelling

Fluids dynamics must satisfy mass, momentum and energy conservation principle which can be expressed in mathematical form. The fluid behaviour needs to be modelled also. The equation set is written for a fluid domain. Boundary and initial conditions must be imposed. Every CFD solver discretizes the set of analytical differential equations into an algebraic system which is solved iteratively. The solver used for the present work is Numeca FINE™/Open v2.12. The discretization procedure implemented in the solver is based on the finite volume method [24] [25].

4.2.1 Mathematical model

The problem is time dependent and the nature of the flow is turbulent. Turbulence is described using the approach proposed by Reynolds. Every fluid property is decomposed as the sum of a steady mean component and a time fluctuating component. The latter by definition has zero mean value.

$$\varphi(t) = \emptyset + \varphi'(t) = \bar{\varphi} + \varphi'(t) \tag{4.5}$$

In equation (4.5) the superscript $\bar{}$ is the Reynolds averaging operator. Following the averaging approach of Reynolds the set of Reynolds Averaged Navier Stokes equations for a compressible Newtonian fluid can be written in the following form [25]:

$$\begin{cases} \frac{\partial \bar{\rho}}{\partial t} + \mathrm{div}\left(\bar{\rho}\widetilde{\boldsymbol{V}}\right) = 0 \\ \frac{\partial(\bar{\rho}\widetilde{U})}{\partial t} + \mathrm{div}\left(\bar{\rho}\widetilde{U}\widetilde{\boldsymbol{V}}\right) = -\frac{\partial \bar{P}}{\partial x} + div\left(\mu\ grad\ \widetilde{U}\right) + \left[-\frac{\partial(\bar{\rho}\overline{u\prime^2})}{\partial x} - \frac{\partial(\bar{\rho}\overline{u\prime v\prime})}{\partial y} - \frac{\partial(\bar{\rho}\overline{u\prime w\prime})}{\partial z}\right] + S_{M_x} \\ \frac{\partial(\bar{\rho}\widetilde{V})}{\partial t} + \mathrm{div}\left(\bar{\rho}\widetilde{V}\widetilde{\boldsymbol{V}}\right) = -\frac{\partial \bar{P}}{\partial y} + div\left(\mu\ grad\ \widetilde{V}\right) + \left[-\frac{\partial(\bar{\rho}\overline{u\prime v\prime})}{\partial x} - \frac{\partial(\bar{\rho}\overline{v\prime^2})}{\partial y} - \frac{\partial(\bar{\rho}\overline{v\prime w\prime})}{\partial z}\right] + S_{M_y} \\ \frac{\partial(\bar{\rho}\widetilde{W})}{\partial t} + \mathrm{div}\left(\bar{\rho}\widetilde{W}\widetilde{\boldsymbol{V}}\right) = -\frac{\partial \bar{P}}{\partial z} + div\left(\mu\ grad\ \widetilde{W}\right) + \left[-\frac{\partial(\bar{\rho}\overline{u\prime w\prime})}{\partial x} - \frac{\partial(\bar{\rho}\overline{v\prime w\prime})}{\partial y} - \frac{\partial(\bar{\rho}\overline{w\prime^2})}{\partial z}\right] + S_{M_z} \\ \frac{\partial(\bar{\rho}\widetilde{\emptyset})}{\partial t} + \mathrm{div}\left(\bar{\rho}\widetilde{\emptyset}\widetilde{\boldsymbol{V}}\right) = div\left(\Gamma_{\emptyset}\ grad\ \widetilde{\emptyset}\right) + \left[-\frac{\partial(\bar{\rho}\overline{u\prime\varphi\prime})}{\partial x} - \frac{\partial(\bar{\rho}\overline{v\prime\varphi\prime})}{\partial y} - \frac{\partial(\bar{\rho}\overline{w\prime\varphi\prime})}{\partial z}\right] + S_{\emptyset} \end{cases} \tag{4.6}$$

In equations (4.6) μ is the viscosity, U,V and W are all three components of the velocity vector $\boldsymbol{V}$ in a Cartesian frame of reference, respectively for directions x, y and z. Source terms are identified with S, and all fluid properties are written with the notation introduced with equation (4.5). In the equations, density and pressure are time averaged, whereas the scalar property and velocity components are density-weighted time averaged, denoted with $\widetilde{\ }$ superscript (Favre-averaging). In Numeca FINE™/Open v2.12 the last equation of set (4.6) is expressed in terms internal total energy. The fluid is air modelled as perfect gas by the constitutive equation

$$p = \rho RT \tag{4.7}$$

Since the flow is compressible the set of equations is fully coupled. In FINE™/Open v2.12 the static pressure is obtained from the conservative variables solving the equation

$$p = (\gamma - 1)\left[\rho E - \frac{(\rho \boldsymbol{V})^2}{2\rho}\right] \tag{4.8}$$

As a consequence of the Reynolds decomposition, in the equation set (4.6) there are additional unknown terms. They are known as Reynolds stresses and they need to be defined with a turbulence model. In analogy with the model of Newtonian fluid, linear eddy viscosity turbulence models are based on the Boussinesq hypothesis which relates the viscous stress tensor to the mean shear rate. Thus Reynolds stresses are defined as:

$$\tau_{ij} = -\rho\overline{u'_\iota u'_j} = \mu_t\left(\frac{\partial U_i}{\partial x_j} + \frac{\partial U_j}{\partial x_i}\right) - \frac{2}{3}\rho k\delta_{ij} \tag{4.9}$$

In equation (4.9) μ_t is the turbulent eddy viscosity, δ_{ij} is the Kronecker delta and indices i and j refers to the Cartesian coordinate system directions x,y,z. k is the turbulent kinetic energy

$$k = \frac{1}{2}(u'^2 + v'^2 + w'^2) \tag{4.10}$$

The problem of turbulent modelling requires a definition of turbulence parameters μ_t and k. In the energy equation, the turbulent heat flux vector must also be modelled. Similarly this is done by introducing a turbulent thermal conductivity Γ_t, related to the eddy viscosity μ_t through a turbulent Prandtl number Pr_t which is imposed 1:

$$\rho\overline{\boldsymbol{V}''h''} = -\Gamma_t \,\mathrm{grad}\, T \qquad \text{where} \qquad \Gamma_t = \frac{\mu_t c_p}{Pr_t} \tag{4.11}$$

Reynolds stresses are no more unknown quantities provided that a definition of the turbulent eddy viscosity μ_t and the turbulent kinetic energy k is given. The problem of turbulence modelling is reduced to the definition of these two quantities over the whole domain.

4.2.2 Turbulence model

Among the few available the choice was for Spalart-Allmaras for three main reasons:

1) it has been historically conceived and implemented to model external flows around profiles;
2) it is based on a single equation which is a good advantage for unsteady problems which requires a huge amount of iterations to converge;
3) it is considered sufficiently robust for both coarse and fine meshes.

The Spalart-Allmaras model implemented in FINE™/Open is based on the papers of Spalart and Allmaras (1992) with the improvement described by Ashford and Powell (1996) [26]. The model neglects the second part on the right-hand side of Boussinesq's hypothesis (equation 4.9) expressing the turbulent eddy viscosity in function of an artificial parameter $\tilde{\nu}$ through equation 4.12:

$$\mu_t = \rho\tilde{\nu}f_{v1} \tag{4.12}$$

In equation (4.12) f_{v1} is a wall-damping function which tends to unity for high Reynolds numbers (in the free stream) and to zero near the wall. The Spalart Allmaras turbulence model has a single transport equation for parameter $\tilde{\nu}$ to be solved over the fluid domain. Details on the structure of the turbulence model are available in FINE™/Open theoretical manual [26].

4.2.3 Numerical scheme

For a control volume Ω delimited by a control surface S, neglecting source terms, the integral conservation laws for a generic transport property W are written as:

$$\frac{\partial}{\partial t}\int_{\Omega} W d\Omega + \int_{S} \boldsymbol{A}\cdot d\boldsymbol{S} - \int_{S} \boldsymbol{D}\cdot d\boldsymbol{S} = 0 \tag{4.13}$$

A and **D** are the advective and diffusive part of the fluxes, while d**S** is the oriented surface element. In the finite volume method, transport properties are defined at the centre of each cell. The finite volume discretization for cell J takes the following form:

$$\frac{\partial}{\partial t}\left(W_J \Omega_J\right) + \sum_{sides}[(\boldsymbol{A}-\boldsymbol{D})\cdot\boldsymbol{S}] = 0 \tag{4.14}$$

Diffusive and convective fluxes are kept separated because they need to be treated in a different way. For diffusive fluxes it is necessary to evaluate gradients on cell faces while advective terms can be computed using transport properties values which are defined at the centre of each cell. A complete explanation of the finite volume method can be found in several books, like the one of Versteeg and Malalasekera [25] . A description of the techniques specifically implemented in FINE™/Open can be found in the solver's theoretical manual [26]. In the present work just a few details are reported.

In FINE™/Open diffusive fluxes are determined in a purely second order accurate central way. For convective fluxes two options are available: a purely central scheme or upwind methods. For the present work the choice was for the second order accurate central scheme.

To solve steady problems, a pseudo-time integration is performed by the solver using an explicit q-stage (q=4 by default in FINE™/Open) Runge-Kutta scheme for the equation:

$$\frac{dW}{dt} = F(W) \tag{4.15}$$

which can be written as:

$$W^1 = W^n + \alpha_1 \Delta t F(W^n) \tag{4.16}$$

$$W^2 = W^n + \alpha_2 \Delta t F(W^1) \tag{4.17}$$

...

$$W^q = W^n + \Delta t F(W^{q-1}) \tag{4.18}$$

$$W^{n+1} = W^q \tag{4.19}$$

The stability area and the order of accuracy of the scheme is defined by coefficients α which can be chosen by the user. The local time step is calculated through the Courant-Friedrichs-Lewy number (CFL). In a simplified monodimensional domain this condition is:

$$CFL = \frac{V\Delta t}{\Delta x} \tag{4.20}$$

In equation (4.20) *V* is the velocity, *Δt* is the local time step and *Δx* is the cell dimension. Since the flow around a bluff body is intrinsecally unsteady, a converged steady state solution of the numerical problem is possible only if the time step of the scheme is wide enough to average the solution unsteadiness. Otherwise iterative convergence will never be reached. In order to do so, it is common practice to increase gradually the CFL number to very high values. In this case, because of the conditioned stability of the scheme it was not possible to obtain a steady state solution. For all the cases solved, the discretization scheme was central second order accurate and CFL was imposed 3. URANS equations are solved with the dual time stepping technique.

In order to do so, the Reynolds-Averaged Navier-Stokes equations are expressed as:

$$\frac{\partial}{\partial t}\int_\Omega W d\Omega + \int_\Omega \frac{\partial W}{\partial \tau} d\Omega + \int_S \boldsymbol{A}\cdot d\boldsymbol{S} - \int_S \boldsymbol{D}\cdot d\boldsymbol{S} = 0 \tag{4.21}$$

where *t* is the physical time, *τ* is a pseudo time and sorce terms have been neglected. A second order backward method impremented in FINE™/Open is applied for the evaluation of the first term of equation (4.21):

$$\left(\frac{\partial}{\partial t}\int_\Omega W d\Omega\right)^{n+1} = \frac{1.5W^{n+1}\Omega^{n+1} - 2W^n\Omega^n + 0.5W^{n-1}\Omega^{n-1}}{\Delta t} \tag{4.22}$$

while all the other terms are computed at time *n+1*. The equation is then treated as a modified steady state problem in the pseudo time *τ*:

$$\frac{\partial W}{\partial \tau}\Omega^{n+1} + R_{TA}(W) = 0 \tag{4.23}$$

$R_{TA}(W)$ is the residual used for the time accurate computations. Denoting by R the residual corresponding to the steady state problem, $R_{TA}(W)$ is given by:

$$R_{TA}(W) = R(W) + \frac{1.5W\Omega^{n+1} - 2W^{n}\Omega^{n} + 0.5W^{n-1}\Omega^{n-1}}{\Delta t} \qquad (4.24)$$

The new residual contains terms that depend only on the solution of previous time steps, all other terms depend on the current solution *W*.
When steady state is reached at each physical time step, the left hand side of equation (4.24) tends to zero and the time accurate solution is obtained.
The physical time step is according to the desired level of accuracy, while the pseudo time step is obtained with the CFL condition. For the present work the physical time step has been set to 10^{-6} seconds, and the number of inner iterations per time step has been set to 50.

4.2.4 Domain definition

The domain has been defined according to information found in papers about similar studies. The fluid domain is a rectangle whose dimensions have been kept as adopted by D. Delhaye and others [7]. Assuming as characteristic dimension the probe diameter, the domain extents for 20 diameter downstream and 10 upstream, left and right sides. In the work of Delhaye cells are triangular. A smaller domain with rectangular cells was adopted by Vaz *et. al*. in [27]. For the present study, the geometry has been created in Catia®, and unstructured meshes have been generated with Hexpress™ which is part of Numeca FINE™ integrated software environment. The default grid generation mode is 3D. 2D domain are still treated as 3D, but only one cell is generated along the z direction and the fluid domain is bounded by two mirror planes [24] in the *z*-direction. The final unstructured grids consist of a flat plate of hexahedral cells with 1 mm height.

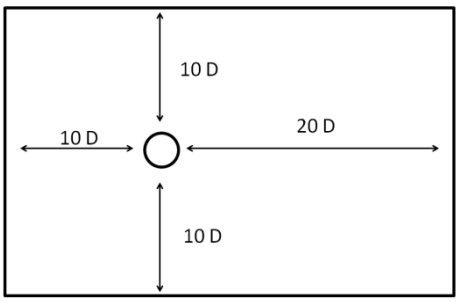

Figure 4.4. Extension of the rectangular fluid domain around the profile.

The independence of the solution from the domain size has been verified with an additional case for a bigger domain. However, since they have been chosen as

external field, and not as walls, there should not be any significant influence of the domain size. Proper cell size and refinement criteria have been established through mesh sensitivity analysis. Different levels of local refinement have been used. In order to properly capture vortex shedding, finer cells have been placed inside zone *B* downstream the profile and around the probe walls in zone *C* (see fig. 4.5). In the external part of the domain, the cell size becomes less critical as the flow is parallel with cell orientation.

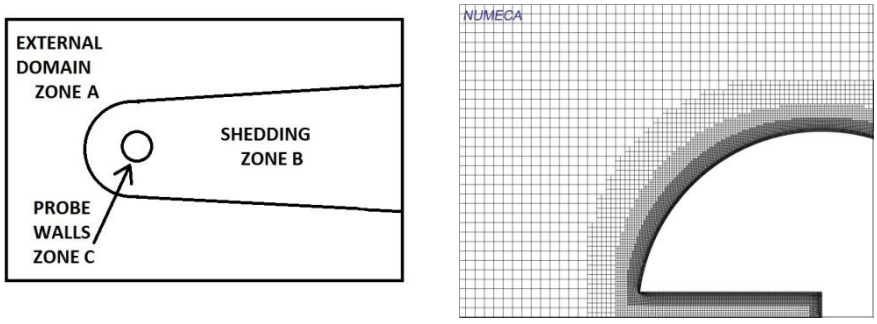

Figure 4.5. Left side: fluid domain details: different refinement zones. Sketch not in scale. Right side: detail of zone B and C cells for *AUX* mesh.

Some global settings have been maintained for all grids in the overall domain generation. In order to achieve smoother transition between different zones, the refinement diffusion level have been increased from 2 to 7. The last step of the meshing is the generation of a viscous sublayer on probe walls to model properly the boundary layer. First cell $y+$ values have been maintained below 1, except for the very coarse grid (*RAW*) where $y+$ reached 1.6 at some locations.

4.2.5 Grid sensitivity

In order to obtain grid independent solution, a grid sensitivity analysis has been carried out. When partial differential equations are discretized in space, a discretization error proportional to the spatial discretization step is introduced. In order to minimize it, grid cells dimensions should be reduced as much as possible. When discretization errors reach the same order of magnitude of the machine truncation errors the solution would not improve anymore and the cost in terms of resources would become prohibitive. The aim of grid dependence tests is to optimize spatial discretization, namely the mesh cells size, going towards a point where solution does not change significantly anymore with further increasing number of cells. The purpose of the analysis is to define a set of refinement settings which is reliable enough to generate grids for all cases investigated. In order to do so, the Grid Convergence Index method has been applied to estimate uncertainty. Other mesh quality indicators like skewness and

aspect ratio have not been taken into account because they are systematically good in such a domain discretized with hexahedral cells.

The grid convergence level has been assessed monitoring relevant flow parameters such as the pressure distribution on the probe profile. The problem is time dependent, thus the comparison has been done in terms of integral time varying quantities. Integration over surfaces is an operation that intrinsically smooths local differences. Thus a few other smaller surfaces have been chosen for this purpose. Moreover, to avoid eventual influence of numerical approximations on the domain solid boundary (properties are numerically extrapolated from the fluid domain on solid boundaries), a small surface immersed in the flow have been considered immediately downstream of the profile.

The variables monitored in the analysis are:

- Inviscid Lift[1] and Drag forces on the probe. (*DRAG* and *LIFT*).

- Static pressure integrated just on a fraction of the probe back surface (+/- 60° respect to *x* axes). (*P STAT BACK PROBE*). See figure 4.6, first from the left.

- Static and total pressure integrated on a vertical plane placed at a length of 1/10 with respect to probe diameter downstream the profile. The ratio between the plane width and the probe diameter is 0.75. (*P STAT JUST DOWN* and *P TOT JUST DOWN*). See figure 4.6, second from the left.

- Static pressure integrated on the probe tap plane. (*P STAT PROBE TAP*). See figure 4.6, third from the left.

- Total pressure integrated on the probe cavity plane. (*P TOT CAVITY*). See figure 4.6, first on the right side.

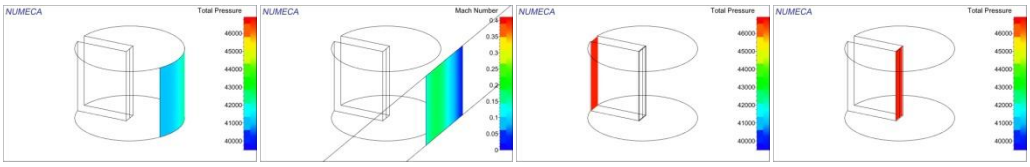

Figure 4.6. Location of selected surfaces for grid sensitivity analysis.

[1] Lift force has been included in the analysis as it was an available variable already monitored for convergence detection. However, since the profile is symmetrical and the corresponding lift is zero, lift time mean value is not suitable for grid convergence analysis.

For each time dependent variable, the time mean value (*MEAN*), the amplitude of the peak to peak oscillation (*DELTA MAX*) and the frequency (*FREQ*) are analyzed. To avoid our analysis being influenced by time discretization, selected quantities were taken with respect to different time intervals. The same number of periods has been chosen for same variable comparisons, but for each variable the number of periods was changed.

Although there is no standard method to quantify numerical uncertainty in the CFD community, a few strategies have been proposed and are accepted by editors. The *Journal of Fluids Engineering* editorial policy [28] for example accept the Grid Convergence Index (GCI) method proposed by Roache [28] [29] which is based on Richardson extrapolation.
For a differential equation solved numerically [30] the discretization error (*Err*) on mesh level *k* can be written as:

$$Err_k = w_k - w_{exact} \tag{4.25}$$

where w_{exact} is the exact solution to the continuum and w_k is a discrete solution on mesh level *k*. Expressing the error by a series expansion and rearranging equation (4.25)

$$w_k = w_{exact} + g_1 h_k + g_2 h_k^2 + g_3 h_k^3 + O(h_k^4) \tag{4.26}$$

where g_1, g_2 and so on are coefficients of the error expansion terms and *h* is a measure of grid spacing. Equation (4.26) is a measure of the order of discretization, and for a formally second order scheme g_1 coefficient will be zero. The general procedure for extrapolation consists in writing equation (4.26) for a number of different mesh levels, solving it for w_{exact} and the dominant error term coefficient. Extrapolated values can simply be used as a more accurate solution or to estimate the error of discrete solutions. In order to do so, the solution must be in the asymptotic convergence range (which implies that higher order terms in equation (4.26) are small).

Starting from standard Richardson extrapolation many techniques have been developed and validated. Derivation of several methods and validations are described in various publications like in [29] [31], [25] and [32]. Application of the method to non uniform grid is investigated by Celik and Karatekin [33]. As explained by Roache [29], in some specific cases it is possible to use extrapolation techniques to get higher order approximate solutions from results obtained with less accurate discretization schemes, but the generalization of the principle is not straightforward. The GCI method considered here is applicable to both uniform and non uniform grid spacing and requires solution on three

different grids. It is also necessary to estimate an apparent order p of the method.
The first step of the procedure [28] is to define an appropriate grid size h

$$h = \left[\frac{1}{N}\sum_{i=1}^{N}\Delta V_i\right]^{\frac{1}{3}} \tag{4.27a}$$

$$h = \left[\frac{1}{N}\sum_{i=1}^{N}\Delta A_i\right]^{\frac{1}{2}} \tag{4.27b}$$

where ΔV_i is the volume and ΔA_i is the area of the i^{th} cell, and N the total number of cells. Equations (4.27a) and (4.27b) are to be used when integral quantities are considered respectively for 3D and 2D problems.
Three different grids need to be solved to determine key variables ϕ to compare. Refinement ratio r is:

$$r = \frac{h_{coarse}}{h_{fine}} \tag{4.28}$$

and should be kept higher than 1.3 (based on experience and not on formal derivation [28]).
If $h_1<h_2<h_3$ (subscript 1 means finest grid) and $r_{21}=h_2/h_1$, $r_{32}=h_3/h_2$. The apparent order p of the method must be found solving equations (4.29a), (4.29b), (4.29c)

$$p = \frac{1}{\ln(r_{21})}\left|ln|\varepsilon_{32}/\varepsilon_{21}| + q(p)\right| \tag{4.29a}$$

$$q(p) = ln\left(\frac{r_{21}^{p}-s}{r_{32}^{p}-s}\right) \tag{4.29a}$$

$$s = 1\cdot sign(\varepsilon_{32}/\varepsilon_{21}) \tag{4.29a}$$

where $\varepsilon_{32}=\phi_3 - \phi_2$ and $\varepsilon_{21}=\phi_2 - \phi_1$. If refinement ratio r is constant $q(p)=0$. Negative values of $\varepsilon_{32}/\varepsilon_{21} < 0$ are an indication of oscillatory convergence. If either ε_{32} or ε_{21} is "very close" to zero the above procedure does not work. Once all parameters have been defined it s possible to compute extrapolated values:

$$\phi_{ext}^{21} = (r_{21}^{p}\phi_1 - \phi_2)/(r_{21}^{p} - 1) \tag{4.30}$$

and similarly, calculate ϕ_{ext}^{32} .
The approximate relative error is:

$$e_a^{21} = \left|\frac{\phi_1-\phi_2}{\phi_1}\right| \tag{4.31}$$

Extrapolated relative error:

$$e_{ext}^{21} = \left|\frac{\phi_{ext}^{12} - \phi_1}{\phi_{ext}^{12}}\right| \tag{4.32}$$

The fine grid convergence index finally is:

$$GCI_{fine}^{21} = \frac{1.25 e_a^{21}}{r_{21}^p - 1} \tag{4.33}$$

Grid convergence indexes (GCIs) represent an error band generally amplified by a factor of safety, like 1.25 in equation (4.33) [29] [25]. This method does not require constant refinement ratio (as others do) and has been validated even on non uniform grids [33] also in case of mixed first and second order schemes.
An important aspect of Richardson Extrapolation is that it applies not only to point-by-point solution values but also to solution functionals [29].
In principle the observed *p* could be higher than 2 (for formal second order schemes) but in practical cases due to many non-idealities it might be inaccurate. Thus high values of *p* should be considered with care. The safety factor in equation (4.33) partially account for this. Extrapolation methods based on just two grids sometimes use a safety factor of 3, but when more accurate three grids sensitive studies are done, a safety factor of 3 has been found to be overly conservative [29]. When *p* is found to be high, uncertainty band might be underestimated. Examples given in [31] and [33] shows clearly that *p* could change significantly when evaluated at different locations. It is common practice then to assume an average *p* to estimate uncertainty and extrapolated values. Celik and Karatekin [33] suggest to limit the maximum *p*, for example to 2 when second order methods are in use.
The debate on numeric uncertainty is still an open issue and this is not the appropriate context for discussing it. In this work the GCI method has been applied in order to satisfy requirements of the scientific community, in agreement with the *Journal of Fluids Engineering* editorial policy which states: "*The GCI method described herein is an acceptable and recommended method that has been evaluated over several hundred CFD cases. [...] Rather, this policy is meant to facilitate CFD publication by providing practitioners with a method that is straightforward to apply, is fairly well justified and accepted, and will avoid possible review bottlenecks.*"

In order to satisfy the requirement of $r > 1.3$ four meshes have been selected among few generated. Average cell size *h* has been estimated according to formula (4.27a) and grids have been combined in three different ways as shown in table 4.1.

Table 4.1. Mesh selected for grid dependence test. For each grid set mesh names, number of cells, average cell dimension *h* and refinement ratio are reported.

MESH NAME	**h**	$\mathbf{r_{43}}$	$\mathbf{r_{32}}$	**CELLS**
RAW (4)	3.47E-04			10 236
COARSE (3)	2.61E-04	1.327	1.374	77 592
AUX (2)	1.90E-04			242 398

MESH NAME	**h**	$\mathbf{r_{43}}$	$\mathbf{r_{31}}$	**CELLS**
RAW (4)	3.47E-04			10 236
COARSE (3)	2.61E-04	1.327	1.843	77 592
ULTRA (1)	1.42E-04			717 310

MESH NAME	**h**	$\mathbf{r_{32}}$	$\mathbf{r_{21}}$	**CELLS**
COARSE (3)	2.61E-04			77 592
AUX (2)	1.90E-04	1.374	1.341	242 398
ULTRA (1)	1.42E-04			717 310

Richardson extrapolation based methods are intended for monotonic converging solutions. Monotonic convergence [32] occurs when $0<R<1$ where R is defined as

$$R = \varepsilon_{21}/\varepsilon_{32} \tag{4.34}$$

while $R<0$ is an indicator of oscillatory convergence and $R>0$ means divergence. Monotonic convergence is evident for all variables for the grid set composed by *RAW*, *COARSE* and *AUX* meshes *(432)*, but not in *COARSE AUX FINE (321)*. All quantities monitored exhibit a trend similar as the example given in figure 4.7.

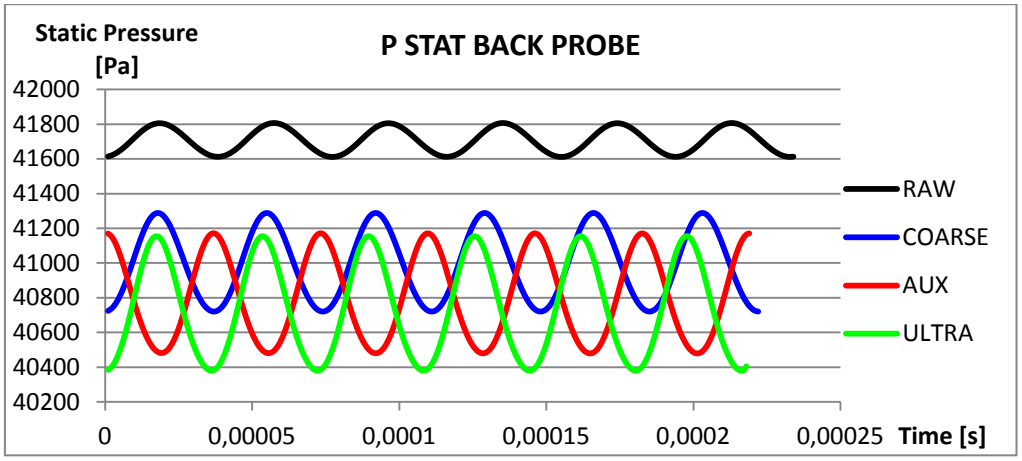

Figure 4.7. Example of variables trend in grid dependence study. The variation of mean values and fluctuations amplitude is clear: it becomes smaller going from *RAW* to *ULTRA* mesh. The variable in the plot is the static pressure integrated on a fraction of the probe back profile.

Frequencies do not exhibit such a relevant change, but all other variables show the same monotonic trend which is more clear if we plot mean values and fluctuations amplitude (see figure 4.8 and 4.9).

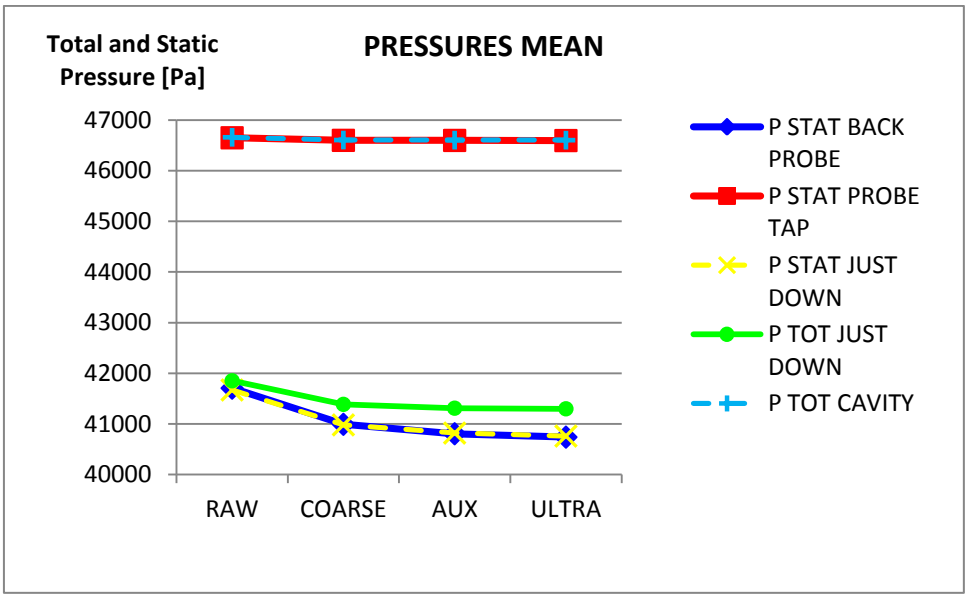

Figure 4.8. Example of pressures time mean signal considered in grid dependence test.

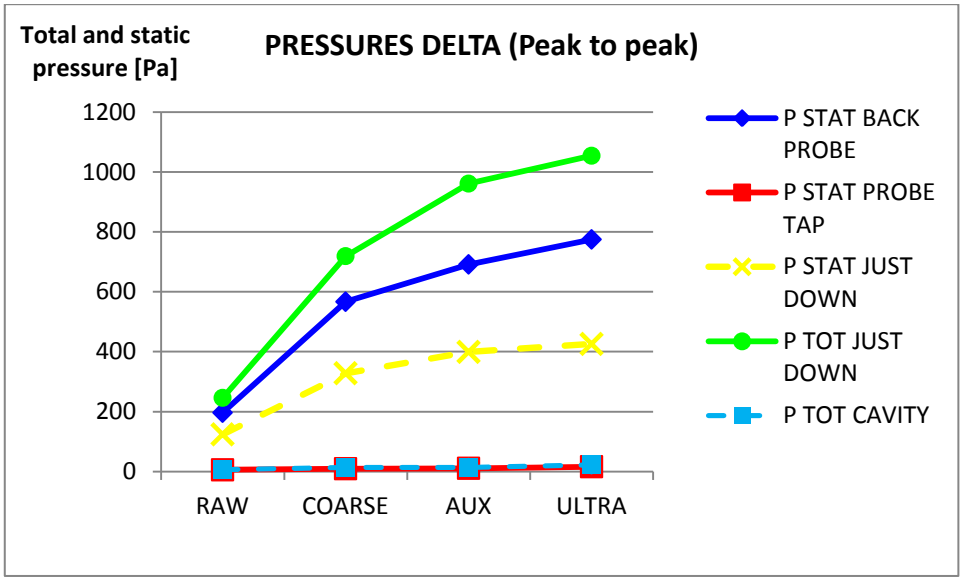

Figure 4.9. Pressure fluctuations amplitude for the variables considered in grid dependence test.

All results for *(432)* and *(321)* grid sets are available in Appendix B. *RAW-COARSE-ULTRA (431)* did not show any relevant benefit respect to the others thus *431* grid set has been rejected. A little change in frequency is found: approximate relative error is below 1.7% when the comparison is between *COARSE* and *AUX* grids. Better estimates of frequency and related uncertainty should be addressed with further work regarding time discretization analysis.
For *AUX* mesh GCIs estimated with grid set *432* are generally below 1% for time mean values, and are in the range of 4 ÷ 12 % for fluctuations amplitude except for the case of total pressure immediately downstream the profile (*P TOT JUST DOWN*) for which GCI is 24%. The apparent order *p* is found to be higher than the formal order of accuracy. According with variables trend and grid sensitivity study, the final choice is for *AUX* mesh. All grids for subsequent computations have been generated with the same refinement settings.
During the mesh sensitivity analysis, it has also been observed a significant difference in the establishment of shedding unsteadiness. Coarser meshes require more time steps to be solved in order to model the wake. Finer meshes are more expensive in terms of computational resources, but the solution convergence is faster in terms of total amount of iterations. COARSE mesh needs approximately 1500 additional time steps before the shedding is completely established in the flow. AUX mesh, which is finer, anticipates

convergence of approximately 1500 time steps which correspond to a global amount of 75000 iterations.

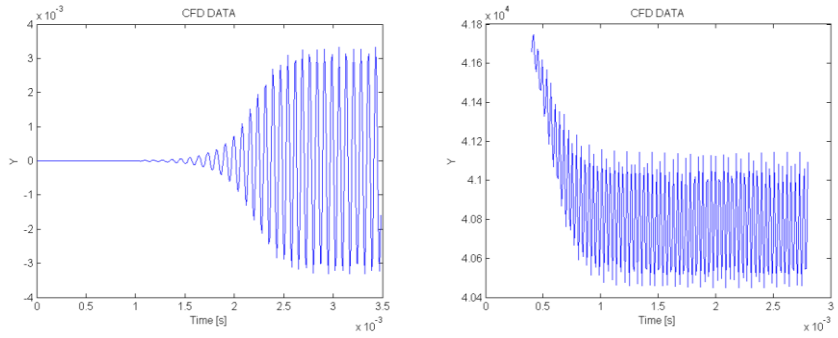

Figure 4.10. Left side: COARSE mesh. Variable monitored: LIFT force. Data are recorded every 10 time steps. Fluctuations of flow quantities on probe walls are not well established before 2.5 second (2500 time steps).
Right side: AUX mesh. Variable monitored: P STAT BACK PROBE . Data are recorded every 10 time steps. Fluctuations of quantities on probe walls already well established after 1 second (1000 time steps)

4.2.6 Boundary conditions

To close the problem a set of boundary condition need to be imposed. The probe surface is treated as a smooth wall, adiabatic, subjected to no slip condition. For lateral sides of the domain (all of them) the choice is for external flow field boundary conditions. These boundary conditions require as input parameters the flow direction, static temperature, static pressure and Mach number. In order to simulate the flow at different angular incidence, the flow direction in the boundary condition has been maintained fixed, and the mesh has been changed accordingly. Each mesh was generated rotating the probe profile of the desired incidence angle.
From expetcted flow conditions given in chapter 2 the following values have been chosen, being them representative of an average operating scenario:

- Static pressure: 43800 [Pa]
- Static temperature: 360 [K]
- Mach number: 0.275
- Flow direction: parallel to the rectangular domain (x direction in the mesh Cartesian reference).

For the turbulence parameter, having chosen Spalart-Allmaras model it is necessary to impose the turbulence viscosity (ν_T) at the boundary. The ratio between turbulent and molecular viscosity used to estimate ν_T was chosen from the CFD results which predict the flow in the facility.

From static flow condition, assuming that air molecular viscosity is dependent only from temperature, with Sutherland's law is possible to estimate the dynamic viscosity (μ):

$$\mu(T) = \mu_0 \left(\frac{T}{T_0}\right)^{1.5} \left(\frac{T_0+T_{Suth}}{T+T_{Suth}}\right) \qquad \text{for T >120 K} \qquad (4.35)$$

where $\mu(T)$ is the dynamic viscosity at temperature T expressed in [µPa·s], μ_0 is a reference viscosity at reference temperature T_0, and T_{Suth} is a constant value depending on the fluid considered. All temperatures must be given in Kelvin. Constants for air are: T_0 = 291.15 K, μ_0 = 18.27 µPa·s, T_{Suth} 120 K.
For T = 360 K equation 5.3 yields to μ= 21.48 µPa·s.
Dynamic viscosity is found from his definition

$$\nu = \frac{\mu}{\rho} \qquad (4.36)$$

being the density ρ = 0.2458 kg/m^3 the kinematic viscosity is 5.05E-5 m^2/s. Multiplying it for the turbulent viscosity ratio μ_T / μ =100 we obtain for boundary condition a turbulent kinematic viscosity ν_T of 5.05·10^{-3} m^2/s.

As initial solution the following constant values have been imposed in the whole fluid domain:

- Static pressure: 43800 [Pa]
- Static temperature: 360 [K]
- Velocity vector components: Vx=104 m/s; Vy and Vz = 0.
- Turbulence viscosity ratio μ_T / μ =100

1000 steady iterations on a three level multigrid have been run as part of the initialization before switch to the unsteady problem.

4.2.7 Convergence criteria

In order to assess convergence of unsteady solutions the methodology presented in chapter 3 has been applied. Convergence has been accepted when full periodicity has been detected in lift and drag forces on the probe profile, as shown in figure 4.10. Typically the exhibited trend is that of a flat line which slowly starts to oscillate until fluctuations becomes periodical. At that point the unsteadiness of the flow is fully modelled and the solution is deemed converged. The method presented in chapter 3 has been applied with an oversampling factor of 10 and the convergence threshold set at 0.99. Examples of the processed

signal and corresponding convergence indicators are shown in figure 4.11 and 4.12.

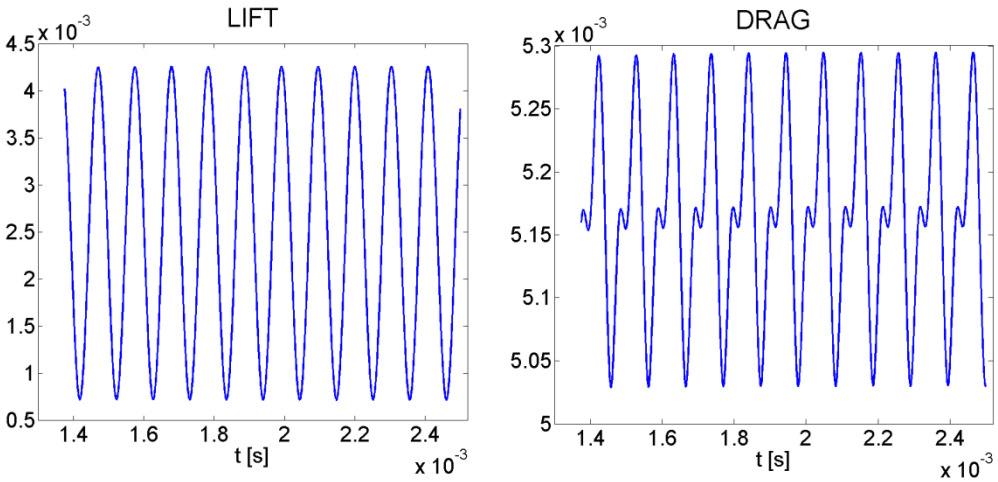

Figure 4.11. Time history of lift and drag forces on the probe profile. Data are taken from CFD simulation of the Kiel probe subjected to flow angle of 30°.

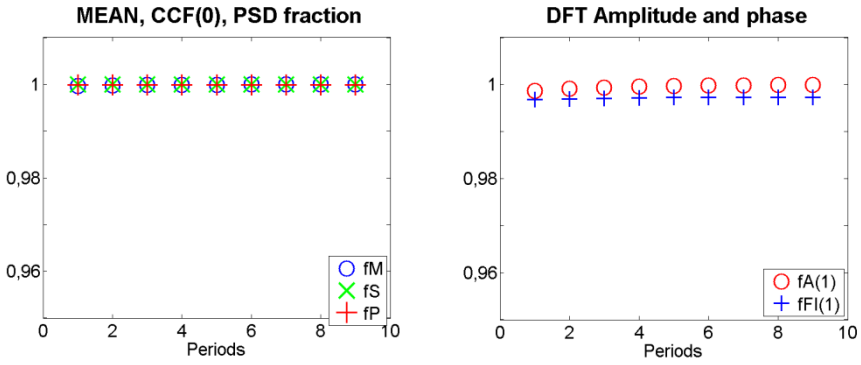

Figure 4.12. Convergence indicators obtained applying the procedure presented in chapter 3 to the variable depicted in figure 4.11.

Primary importance has been given to flow quantities monitoring but also global residuals have been observed. For all cases they decreased of a few orders of magnitude with respect to the first iteration. After the steady initialization which brought all of them below order of magnitude of 10^{-3}, for each unsteady time step they exhibit a step increase at the first iteration and a strong decay during 50 inner iterations of the physical time step. At the end of each time step, in the final part of the solution, the order of magnitude of normalized residuals was below 10^{-9} for density and energy equations, below $10^{-7.5}$ for *x* and *y* momentum

equation, below 10^{-11} for turbulence model equation. A test case revealed that further increase in the number of inner iterations did not improve the solution.

4.3 Results

Validity of results from numerical modelling should always be assessed through comparison with experimental data and literature. Most of the available information, like the correlation used to estimate the Strouhal number, have been obtained gathering data from several experimental campaigns over different ranges of Reynolds numbers. An extensive work on cylinders aerodynamics has been done by Lienhard [22]. He refers also to studies conducted by two other authors who are mentioned very often in literature: Wieselberger [34] and Roshko [35]. Most of these studies have been conducted at low speed and apparently there is scarce literature about the influence of the Mach number on Strouhal number and drag coefficient. Experiments on the influence of Mach number in subsonic and transonic region have been conducted by Rodriguez [20] in 1984. He did not find any significant influence of Mach number on the Strouhal number, but he was able to see a progressive increase in the drag force, thus the drag coefficient depends also on the Mach number. Shirani [36] in 2001 still outline a lack of reference for studies about the cylinder in compressible flow at low Mach numbers.
From a numerical point of view, further sensitivity studies of the model in terms of time discretization and turbulence parameters should be assessed. Reliability of results should also be confirmed or rejected by proper experiments. However, assuming that the model provides reasonable results it is possible to look at them critically and get some valuable insights.

Most of the following results are expressed comparing the single hole cylindrical probe with the Kiel probe. In order to make a fair comparison, pressure readings are compared with respect to the pressure tap in both cases. As highlighted in figure 4.13, the pressure tap for the Kiel is the same as for the normal probe. The pressure tap is the surface corresponding to the line inlet, not the frontal area of the Kiel shield. Some results, instead, are referred to the pressure read by the probe (in the two dimension numerical model). In this case what is referred as the pressure measured is the pressure found at the end of the line, on the plane labelled as "cavity" in figure 4.13.

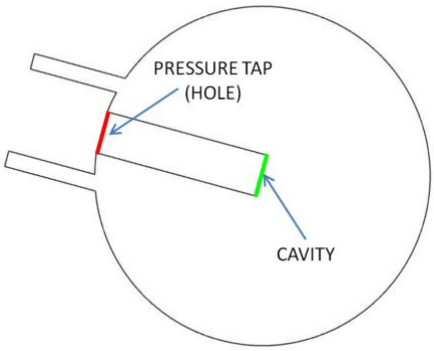

Figure 4.13. Detail of surfaces adopted for CFD data post processing.

4.3.1 General aerodynamics consideration

The first comparison to assess the validity of the model should be to compare Strouhal number computed from the CFD with the estimated value. Similar graphical correlations are available for predictions of drag coefficient as a function of Reynolds number.

For the 1.47 mm profile used in the grid sensitivity analysis, the estimated Strouhal number was found to be 0.21. For the same Reynolds (3000), according to Lienhard [21] [22] the mean drag coefficient should be around 0.9-1. The mean drag coefficient is defined as:

$$Cd = \frac{D}{\frac{1}{2}\rho V_{\infty}^{2} S} \tag{4.37}$$

Where D is the drag force, ρ is the density; V_{∞} is the velocity of the undisturbed flow and S the frontal section area of the body, which is simply the product of diameter and probe section length in this case.
The drag coefficient is a time dependent quantity, which consists of two contributions: the effect of the pressure distribution around the profile and the viscous stress on the wall.
The pressure distribution account for more than 95% of the total drag force.
From the converged solution the Strouhal number was found to be 0.18 and the mean drag 1.32. The difference of Strouhal numbers seems to be close to the order of magnitude of uncertainty given in the work of Lienhard [22]. However, the drag coefficient obtained from the CFD, seems to be wrong. The range of uncertainty for measures of drag coefficient is not clear. From figure 4.14 it is evident that experimental results does not fall exactly on the line which represent the best fitting over a range of experimental data. Some measured drag coefficients are above 1.2. The same is visible in the experimental data

conducted more recently at the Marine Research Institute (Netherlands) [27], where the experimental drag coefficient was found to range from 1 to 1.4.

It has to be considered that in the work of Lienhard, the flow velocity is low and boundary layer on the cylinder is assumed to be laminar until the transition occurs in proximity of $Re=2\cdot10^5$. In the present numerical investigation, the flow is at relatively high speed and modelled as fully turbulent, thus extrapolation from correlations might not be accurate.

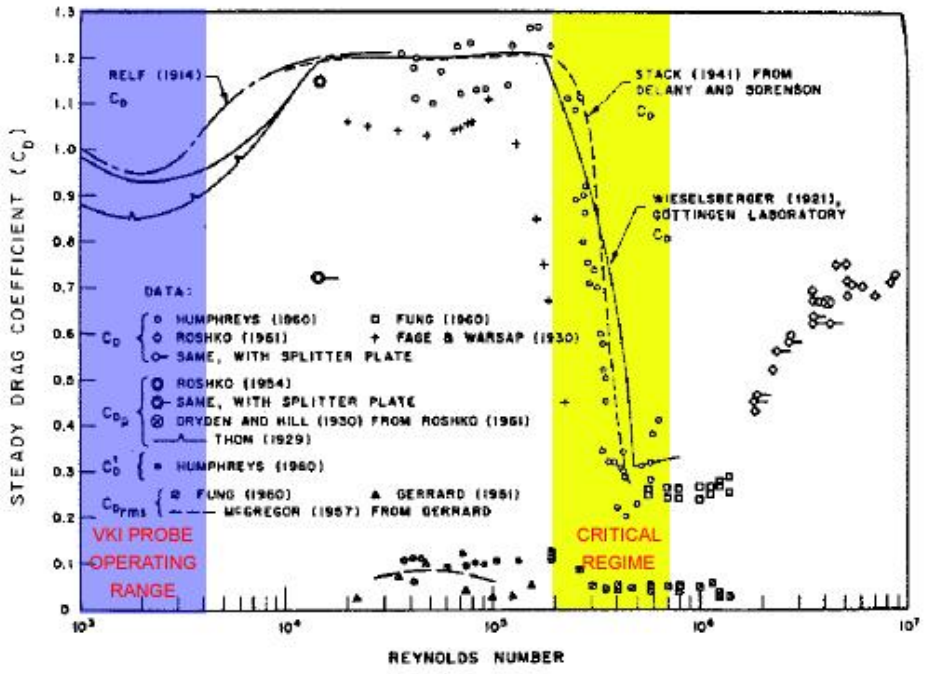

Figure 4.14. Drag coefficient results for circular cylinders in the range of $10^3<Re<10^7$ [22].

In the subcritical regime, the location of the separation point it is retained to be at an angular distance of 80° from the forward stagnation point. For higher Reynolds numbers, after an increase in the drag coefficient, transition occurs and the dethatching point moves downstream at ≈ 140°. Consequently the drag coefficient drops and the wake narrows.

The excessive drag predicted by the numerical model might be attributed to two main reasons:
1) the turbulence model;
2) influence of boundary conditions (domain dimensions too small);
3) presence of the tap on the profile (the probe is not a perfect smooth cylinder);
4) Mach number.

Turbulence model

The turbulence model should be the first factor to be questioned in this analysis. Sensitivity to the turbulence parameter, as well as test cases with different turbulence models should be done and compared. However, as highlighted in the numerical study conducted by the Marine Research Institute [27] results might be even less accurate. In that work, a deep sensitivity study has been conducted in which results are obtained using k-ω SST, a k-ω transition model and even an ω-based Reynolds stress model, both in two and three dimensions. For the two dimensional computations, errors on the drag coefficient range from 26% to 39%, which is absolutely not significantly better than results found in the present investigation. Only the Reynolds stress model, and the 3D DES simulation seem to be more accurate, but this is achieved thanks to an increase in computational cost which does not compensate the benefit.

Influence of boundary conditions.

Artificial blockage effect might be encountered if the domain is not sufficiently extended from the profile. Influence of boundary conditions has been excluded running an additional case. The domain was extended in all directions of a distance corresponding to further 10 probe diameters upstream, 5 on lateral sides, and 10 downstream. The overall drag decreased only of 2 % thus the domain size is not retained to affect sensibly the numerical solution.

Presence of the tap on the profile.

Even if small, the probe tap makes the profile slightly different from the smooth cylinder. To question the influence of the pressure tap, an additional auxiliary case was executed, with a perfect cylindrical profile. Figure 4.15 depict the drag coefficient obtained for the perfect cylinder modelled whit the same mesh characteristics and boundary conditions used for probes.

The mean value of the drag coefficient for the perfect cylinder, is 1.29, slightly lower than the case with the pressure tap.

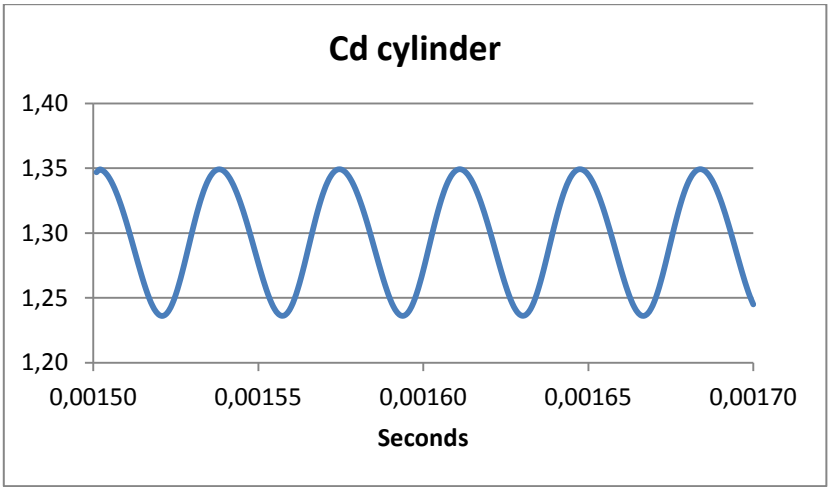

Figure 4.15. Drag coefficient results for the cylinder obtained with the numerical model.

The difference between the two cases account approximately to 3%. In order to see if the pressure tap affect sensibly the pressure distribution on the profile, it is also possible to compare pressure profiles, taken at corresponding instants, for cases with different flow incidence. Pressure profiles on the probe at the instant of maximum lift are given in figure 4.16, respectively for the case of 0, 45 and 60 degrees of angular incidence. It is clearly evident that the hole presence has a negligible impact on the pressure distribution, especially on the pressure side of the profile.

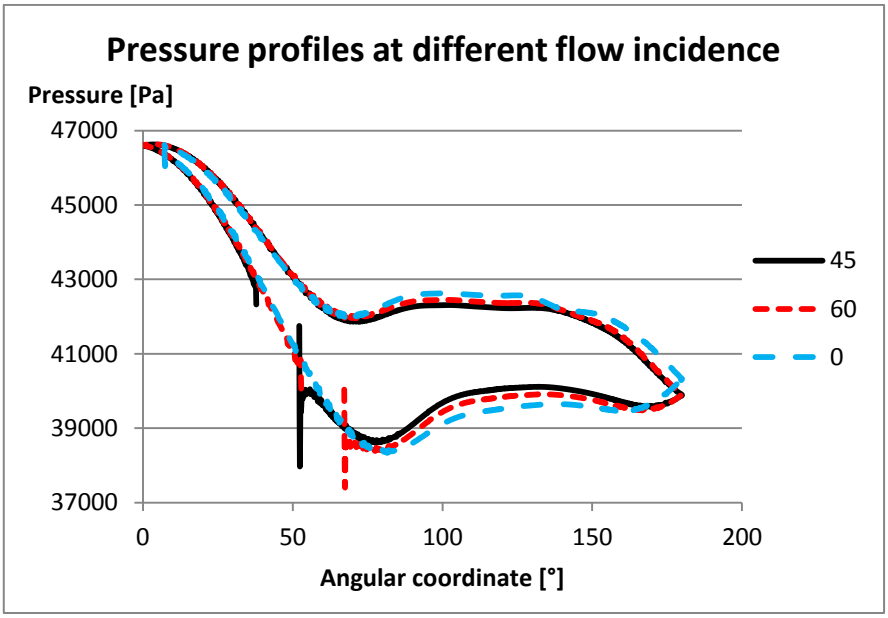

Figure 4.16. Static pressure distribution on the probe profile, when the lift force is at his maximum value, for the normal probe profile with aligned with the flow, and rotated of 45 and 60 degrees.

Mach number.
The main contribution to the extra drag however could probably be ascribed to the effect of compressibility. The Mach number imposed at the boundary is 0.275. On the probe profile it changes continuously in time, and locally it can increase up to 0.5.

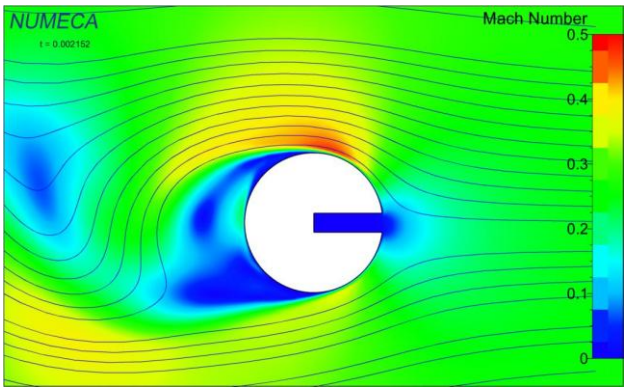

Figure 4.17. Contours of the Mach number for the single hole cylindrical probe at angular incidence of 0°. The contour refers to time step (toss.) 2152 of the converged solution obtained during the grid sensitivity analysis with *AUX* mesh. At this time the pressure drag force is at his maximum value.

Viscous contribution to the total drag force in general is small except for very low Reynolds number. In this case it has been found to account for about 5% of the total drag force. The reason for the excessive drag thus must be searched looking at the pressure distribution around the profile. Pressure distribution around the profile taken at three different times are depicted in figure 4.19. In order to have a complete representation of the unsteadiness, profiles have been taken at three representative instant with respect of the drag force: at instants of minimum, medium, and maximum drag.
Results are shown in the commonly adopted nondimensional form of a pressure coefficient, *Cp*, defined on the probe profile as:

$$Cp = \frac{P - P_\infty}{\frac{1}{2}\rho_\infty V_\infty^2} \tag{4.38}$$

In definition (4.38) P is the static pressure on the profile, and the other variables expressed in the usual notations are properties of the undisturbed flow. In the chart background, there are theoretical pressure profiles representative of the subcritical and post critical regime [37]. In subsequent charts, pressure profiles are given according to the notation sketched in figure 4.18. The angular coordinate goes from 0° at the stagnation point up to 180° at the extreme opposite side of the cylinder. The angular coordinate is taken as positive in both

directions and the two sides of the profile are identified as "TOP" and "BOTTOM".

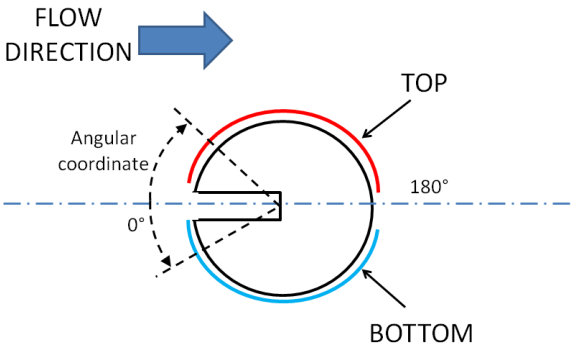

Figure 4.18. Definition of the angular coordinate and references for profiles representation.

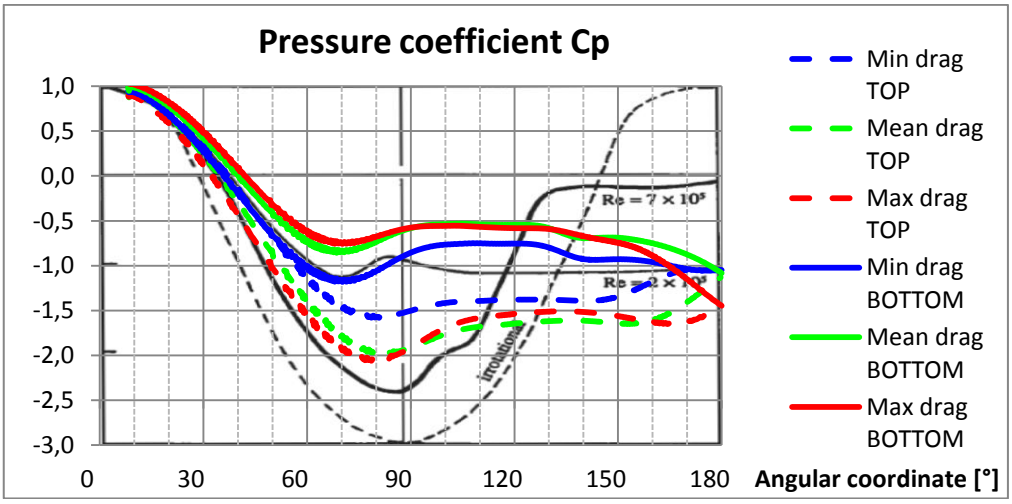

Figure 4.19. Pressure coefficient *Cp* along the probe profile. Data are taken from the converged solution on *AUX* mesh from the grid sensitivity analysis at three different times, respectively when the drag force is at a minimum (t.s.=1770), at his mean value (t.s.=1778) and at his maximum (t.s.=1787). On the background, theoretical profiles for the cylinder in subcritical regime (up to $Re=2\cdot10^5$) and post critical regime ($Re=7\cdot10^5$) according to Colombo [37].

From these profiles the flow seems to be clearly in the subcritical regime which is in line with expectations. In the post critical regimes, in fact, after the flow dethatches, the pressure profile becomes flat. In the post critical regime, after a bubble dethatches, the boundary layer reattaches to the profile and the pressure keeps increasing. The profile becomes flat later, after the flow dethatches again at an angular position of about 140°. From this representation it is not straightforward to detect the position of the dethatching point which can be

better seen from the friction coefficient distribution. Where the flow dethatches, the local friction coefficient is zero because the wall shear stress is null.

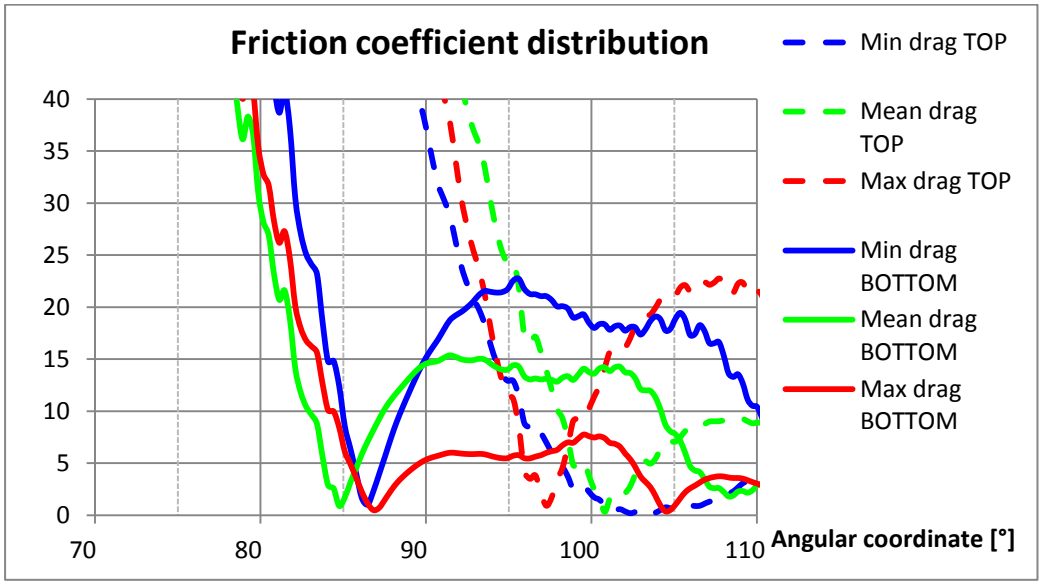

Figure 4.20. Details of the friction coefficient distribution the profile. Data are taken from the converged solution of *AUX* mesh from the grid sensitivity analysis at three different times, respectively when the drag force is at a minimum (t.s.=1770), at his mean value (t.s.=1778) and at his maximum (t.s.=1787).

The numerical model predicts a dethatching point which oscillates between approximately 85 ° and 100 °. This means that the probe frontal area over which a positive pressure is insisting before flow dethatches is maximized and the drag force consequently should increase. The dethatching point oscillating around the 90° angular position, might indicate that the flow is approaching the critical regime. In this range of flow regimes, according to Lienhard's correlations, the drag is maximum, and is about 1.2. It is known that the effect of turbulence is to anticipate the regime transition, so, if the model is capable to assess this feature, the error on the drag coefficient would even be more reasonable.

The effect of the Mach number on the drag force has been measured by Rodriguez [20]. He found an increase in the drag force with progressively higher Mach numbers. In his work, he measured the steady drag force on a cylinder from the steady pressure distribution on the profile. A comparison between results from the present investigation and the work of Rodriguez is given in figure 4.21. In order to make a fair comparison, the contribution to the drag force due to the viscous stresses have been neglected, thus the drag coefficient obtained numerically on the probe profile drops to 1.27, and for the perfect cylinder it drops to 1.23, which are very close to the prediction. In order to check if these values follow a trend which is in line with experiments of

Rodriguez, an additional case have been solved, changing the boundary conditions, to obtain a lower Mach number while keeping the Reynolds number to 3000. (Static pressure 94600 Pa, M=0.1, static temperature 300 K; turbulent viscosity ratio has been maintained 100). The pressure drag coefficient obtained in this case is 1.11, and it is represented along with the others in figure 4.21.

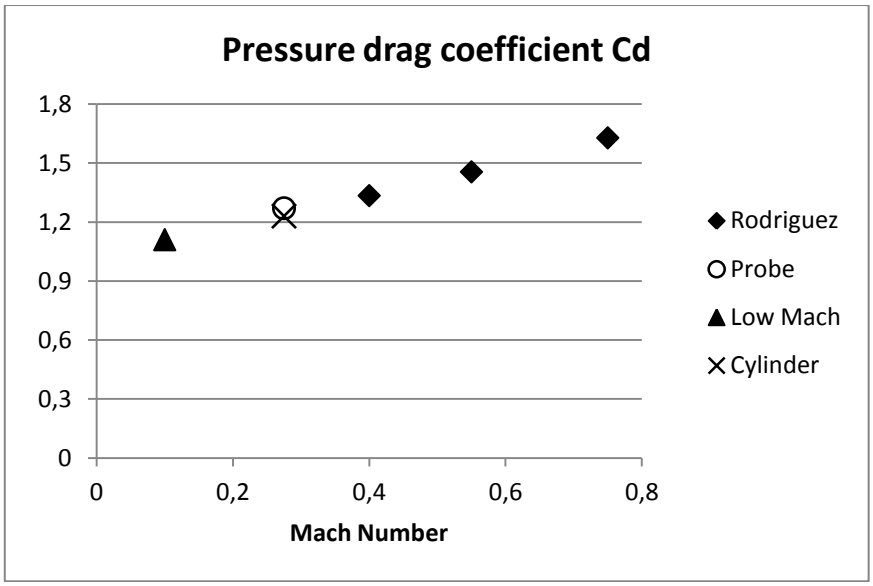

Figure 4.21. Drag coefficient on the cylinder at different Mach numbers. Data plotted with squares are taken from the paper of Rodriguez, while the other points are obtained in the present investigation. The data labelled as "*Probe*" corresponds to the probe profile at nominal condition; "*Cylinder*" is obtained with the perfect cylindrical profile and "*Low Mach*" has been obtained with an additional case with different boundary conditions in order to get the same Reynolds number with a lower Mach.

According to the chart, the drag coefficient increases linearly with the Mach number. Even when the numerically obtained pressure profiles are compared with the few given in [20], it seems that there is a coherent trend in their evolution as a function of the Mach number.
The drag increase is attributable to the increase of the static pressure on the pressure side of the profile, with respect to the upstream conditions.
All of these considerations must be taken with care, but it is reasonable to conclude that the pressure distribution on the probe profile obtained with the present numerical model, is realistic and not significantly distorted, at least on the pressure side of the probe. The turbulence model in use should be investigated more thoroughly and the effect of compressibility on the drag force should be validated experimentally. Nevertheless, this should not represent a critical issue in the present work, since the CFD is used to compare the two probes performance. Even though errors in the absolute value of pressure on profiles might be found, they should not affect significantly the results in terms

of probe performances, because they are evaluated through a comparison between the two cases.

4.3.2 Kiel probe aerodynamics

Regarding the Kiel probe, general aerodynamics is influenced sensibly by the flow incidence, because of the high asymmetry of the profile. The only aspect that is worth to be mentioned here is that according to the CFD computations, it seems that there is a critical incidence which introduces higher disturbances in the flow. This appears clearly from inspection of pressure or Mach number contours.
Apparently at 30° of angular incidence, the effect of the Kiel on the separated region downstream the profile is bigger respect to any other angular incidence.

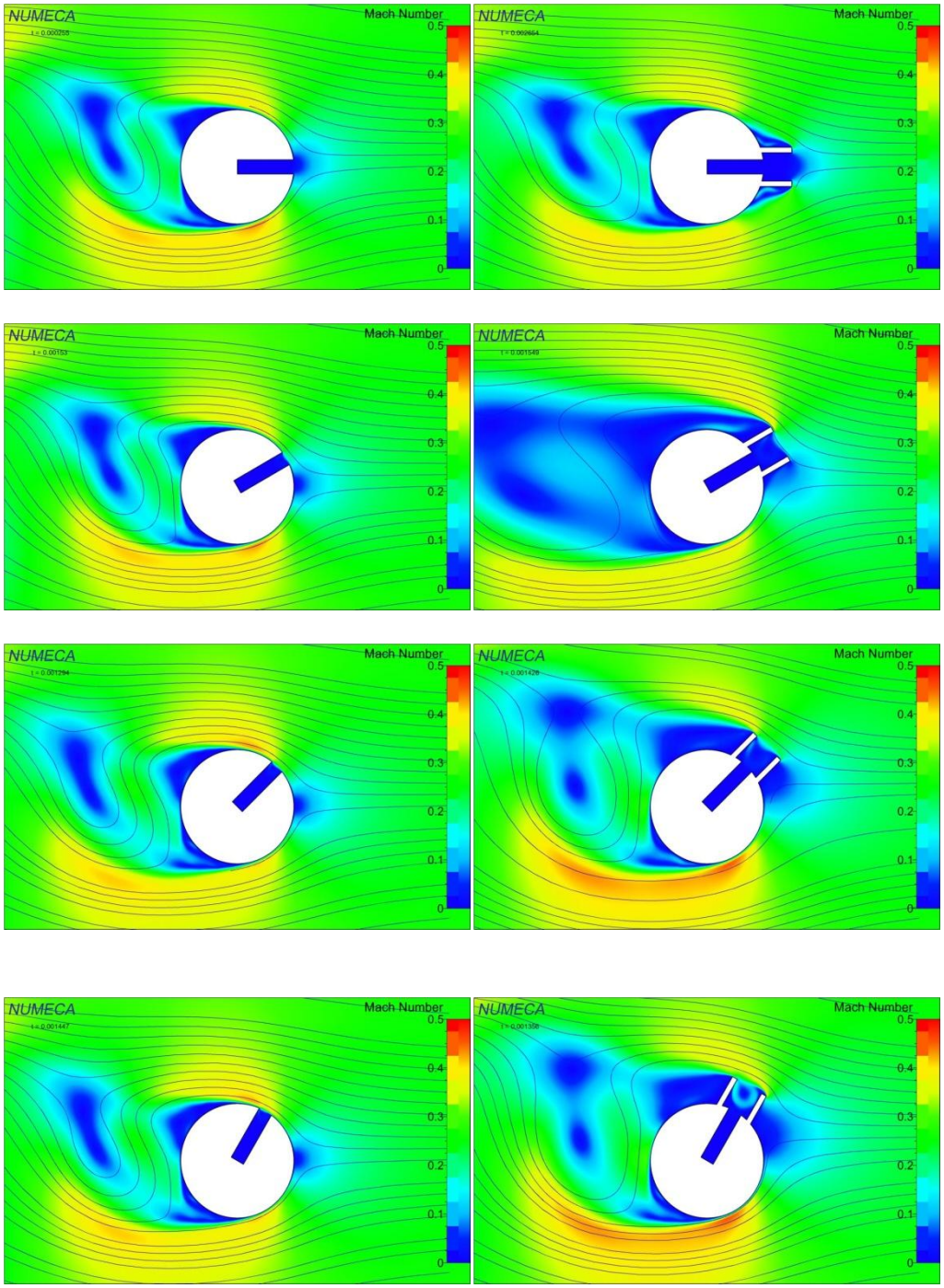

Figure 4.22. Contours of the Mach number around the probe profile at the moment when lift force is at mean value for both profiles for flow incidence of 0°, 30°, 45° and 60°

4.3.3 Angular sensitivity

The effect of the introduction of the Kiel on the angular sensitivity can be regarded in several ways.
Defining a total pressure coefficient as:

$$Kp_{TAP} = \frac{p_{0,TAP}}{p_{0,UPSTREAM}} \tag{4.39}$$

It is possible to evaluate the total pressure distribution in the boundary layer insisting on the pressure port. This is a sort of potential for total pressure measurements. In principle, a good cylindrical probe could measure a maximum value of total pressure, which is limited by this factor. Results are shown in figure 4.23. The coefficient is evaluated for both profiles.

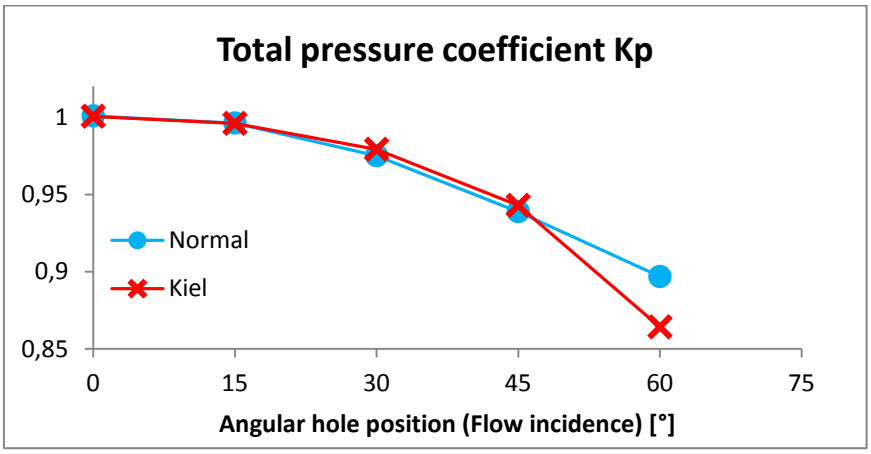

Figure 4.23. Total pressure coefficient *Kp* for both profiles as a function of the angular hole coordinate (flow incidence).

For transverse cylindrical probes it is common practice to evaluate the pressure distribution on the profile in terms of a static pressure coefficient *Cp*:

$$Cp = \frac{p - p_2}{p_0 - p_2} \tag{4.40}$$

where p is the average pressure integrated on the probe pressure tap, p_2 is the static pressure at the end of the domain downstream the profile and p_0 is the undisturbed total pressure upstream. Results are compared with a theoretical pressure profile on a transverse cylinder taken from Bryer and Pankhurst [3].
In terms of *Cp*, results are more clear, because local pressure values are compared with respect to the dynamic fraction of the total pressure.

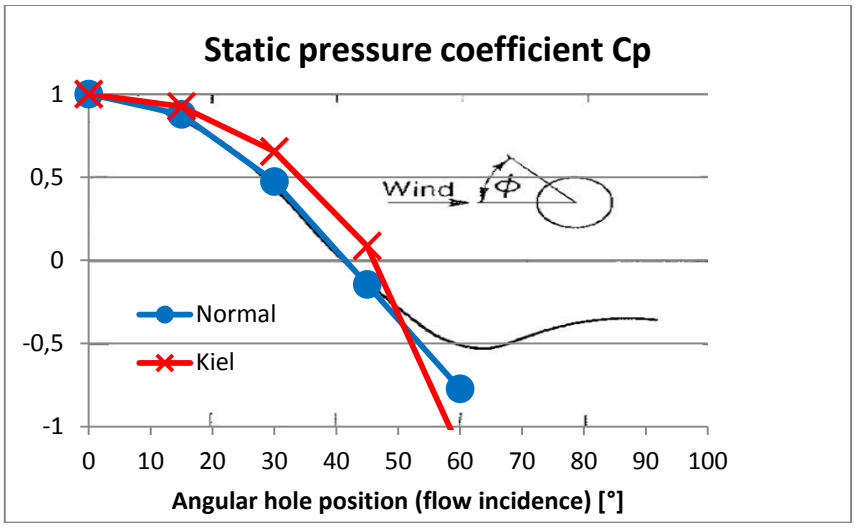

Figure 4.24. Static pressure coefficient *Cp* evaluated on the probe tap for both profiles as a function of the angular hole coordinate (flow incidence). Comparison with a theoretical profile.

Both plots shows that the introduction of a shield make the Kiel probe less sensitive to the incidence angle in the range of interest which is up to 30° of angular incidence. The relative gain in terms of *Cp* accounts to 5% for 15° of angular incidence and to 38% for 30°.

The most valuable way to see benefices introduced by the Kiel in terms of angular sensitivity, however, should be clarified in terms of calibration coefficients, which for real probes are determined experimentally.
In terms of total pressure, for the probe developed at Politecnico di Milano, a static calibration coefficient was defined as follow:

$$K_{pt} = \frac{P_t - P_c}{P_t - P_s} \tag{4.41}$$

In formula (4.41) P_t and P_s are respectively total and static pressure, while P_c is the pressure measured by the probe. From the few angular positions investigated numerically, it is possible to estimate values of K_{pt} and compare them with the performance found experimentally for the original probe. Results are given in figure 4.25. On the plot background, experimental results of the original probe design (Milano) are given [1].

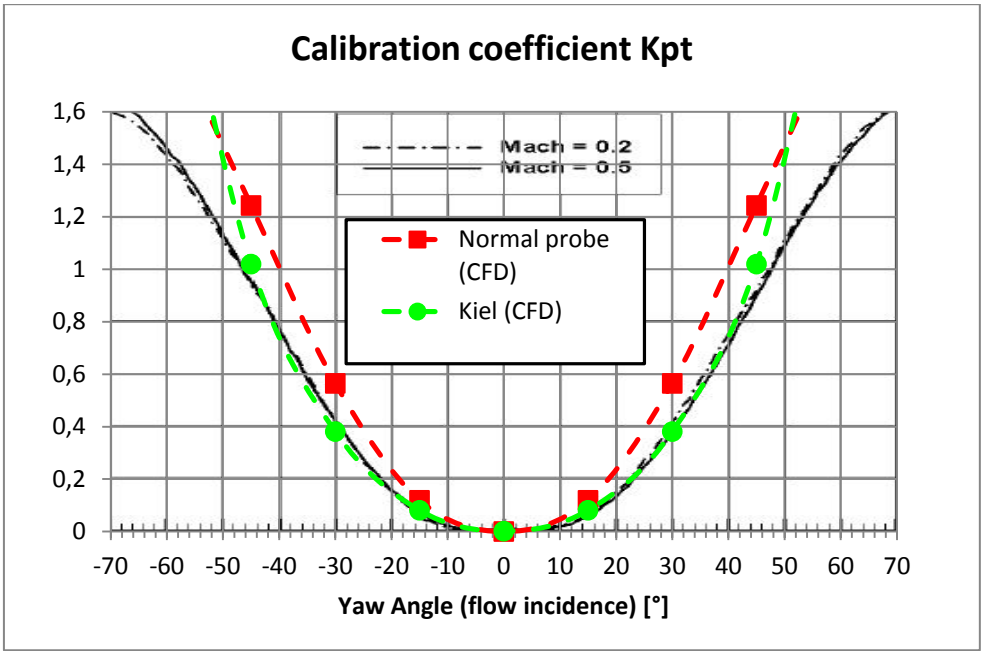

Figure 4.25. Comparison of the calibration coefficient *Kpt* estimated with the numerical model and the coefficient determined experimentally for the original probe at Politecnico di Milano.

According to the CFD, the new prototype should have a higher slope for the static calibration coefficient K_{pt}. If found to be true, this might be due to the smaller probe diameter.
The curvature around the minimum point seems to be in favour of the original design respect to the new prototype (normal probe) in terms of angular insensitivity. This is coherent with the smaller angular span of the pressure tap evaluated in the preliminary design.
The introduction of the Kiel improves the angular insensitivity in proximity of zero incidence, but for higher flow angles, the calibration coefficient for the Kiel probe looses linearity which is generally desired in order to have good calibration maps. However it does not seem that the Kiel is able to provide a significantly wider region of angular insensitivity around the zero angular incidence.
In the end, for high angular incidence, the numerical model estimates depart significantly from experimental data on similar probes.

4.3.4 Kiel length optimization

In order to define the optimal Kiel length, additional CFD cases have been performed. The Kiel length originally chosen to be 0.4 mm has been doubled and reduced by 50% for both cases at 30 and 15 degrees of angular incidence.
The comparison is more clear when it is made in terms of *Cp*.

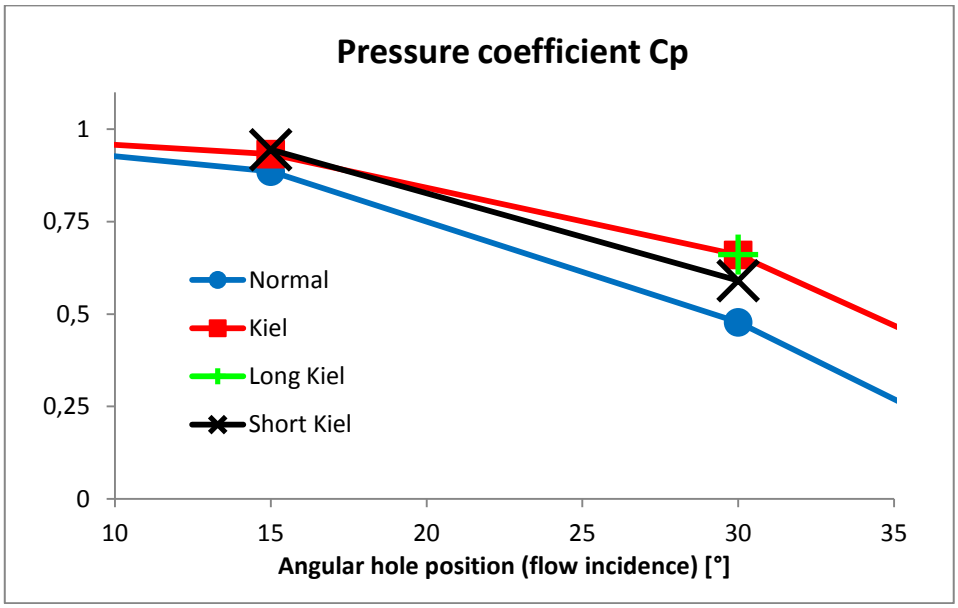

Figure 4.26. Effect of the Kiel length on the static pressure coefficient *Cp*.

At 30°, apparently, the pressure on the probe port increases with the kiel length, but not linearly. The double length Kiel gave the same results as the baseline. Thus the length adopted for the prototype manufacturing seems to be adequate, while a longer Kiel should not introduce any benefit. In the final design, further increase of the Kiel length must be avoided.
At 15° the length of the Kiel seems not to influence the response significantly.

4.3.5 Pressure readings

Pressure detected on the probe tap have been compared with the pressure at the end of the cavity in the two dimensional model. The purpose of the next observation is to see if the damping effect introduced by the line is independent on the flow incidence or not. Results are given in terms of recovery coefficient defined as follow:

$$K_{rec} = \frac{P_{CAVITY} - P_{STAT,TAP}}{P_{TOT,TAP} - P_{STAT,TAP}} \tag{4.42}$$

The coefficient expresses which fraction of the dynamic pressure available on the hole surface in principle could reach the transducer. In K_{rec} definition $P_{TOT,TAP}$ stands for the total pressure detected on the hole surface, $P_{STAT,TAP}$ is the static pressure on the same plane and P_{CAVITY} is the pressure at the end of the two dimensional line.
Table 4.2 gives the recovery coefficient for the normal probe

Table 4.2. Recovery coefficient K_{rec} for the normal probe for different flow incidence.

INCIDENCE	0 °	15 °	30 °	45 °	60 °
K_{rec}	97,2%	29,3%	6,3%	-0,1%	-8,0%

Values obtained with incidence of 45° and 60° are misleading because in that case both numerator and denominator in equation 4.42 are of the same order of magnitude, and numerical errors are amplified. From the trend it is evident that at 0° the pressure measured by the probe is almost coincident with the total pressure which acts on the hole surface. At increasing incidence the pressure read by the sensor tends to coincide with the static pressure found on the pressure tap. This evidence appears also looking at data in figure 4.27.

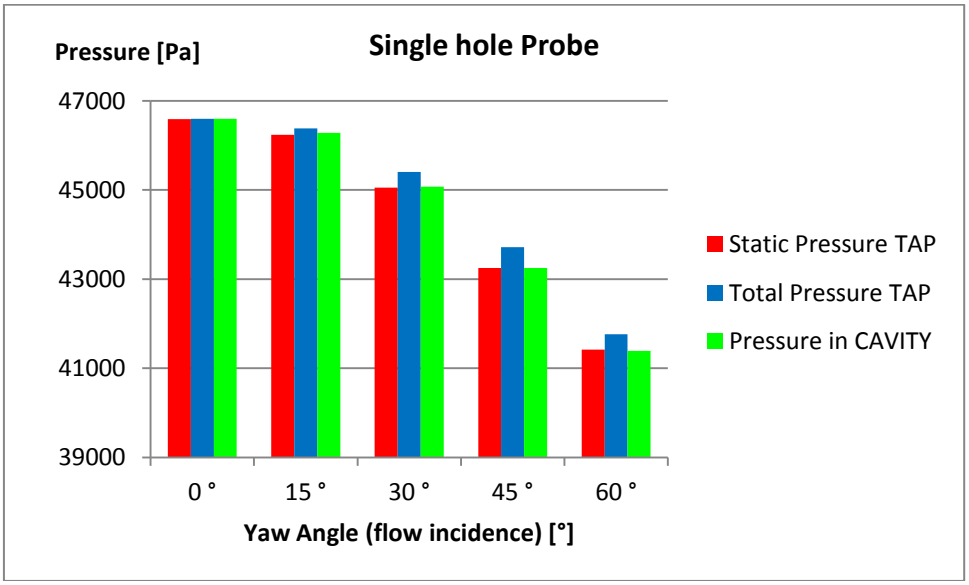

Figure 4.27. Total and static pressure on the probe tap and in the cavity for the normal probe subject to different flow incidence.

From these observations we can assume that angular incidence affects total pressure measurements for two reasons. The most important is the configuration of the boundary layer on the probe profile, which determines the pressure that could be sensed by the probe (for example by a surface mounted transducer). In addition to this, the angular incidence with respect to the line direction seems to

have a non negligible impact in terms of total pressure measurements carried on with a line-cavity arrangement.
This aspect may have already been included in the acoustic analysis of the original probe. If not, for further improvement and optimization, it should be questioned properly, and slightly converging line instead of cylindrical should be considered.

In this context the introduction of the Kiel changes the scenario. For the Kiel probe, the recovery coefficient has no sense, since at the pressure port (but also at the end of the cavity) static and total pressure are almost coincident. In fact the flow has been brought to rest through the cylindrical shield which is placed upstream of the pressure tap. If the total pressure ratio *Kp* defined in equation 4.39 or the static pressure coefficient *Cp* would account for this, the positive effect introduced by the kiel would be more evident.

4.3.6 Vortex shedding

The effect of vortex shedding is evaluated in terms of frequency and amplitude of pressure fluctuations on the pressure tap and at the end of the cavity. In terms of frequency the first thing to notice is that at 0° the pressure unsteadiness is dictated by the drag frequency, because of the synchronized effect of two vortices on the top and bottom side of the profile. At every other incidence, pressure fluctuations are governed by the lower fundamental frequency of the unsteadiness which is the lift frequency. For the cylindrical probe the lift frequency is the same for every incidence. For the Kiel probe different frequencies are found at different incidence, because the frontal area of the profile in the transverse direction changes accordingly. The frequency has a minimum at 30° of angular incidence. From this observation we can conclude that in case vortex induced pressure fluctuations will affect measurements, it is more difficult to detect and filter them for the Kiel probe, since they can be influenced also by the flow direction.

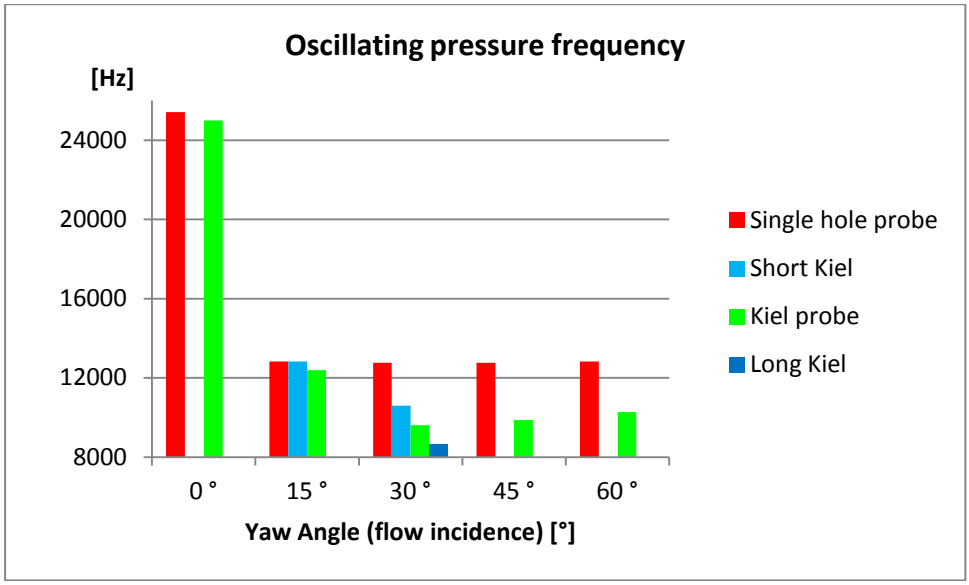

Figure 4.28. Frequency of pressure oscillations on the probe tap for all the cases.

The impact of pressure fluctuations is evaluated in relative terms:

$$\frac{P\prime}{P_{mean}}\% = \frac{P_{\max}(t) - P_{\min}(t)}{2P_{mean}} \cdot 100 \tag{4.43}$$

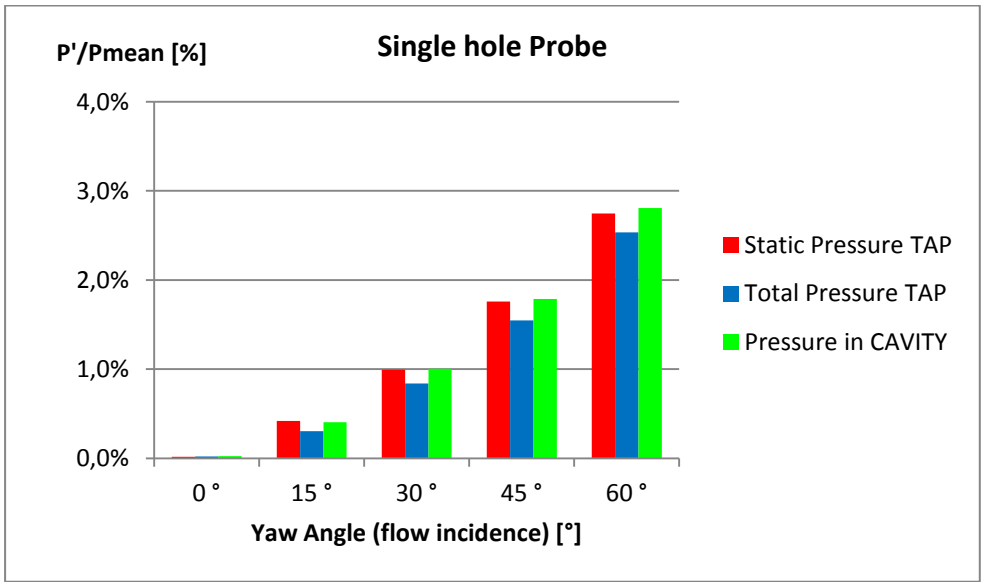

Figure 4.29. Impact of pressure fluctuations on the mean value in relative terms for the single hole cylindrical probe.

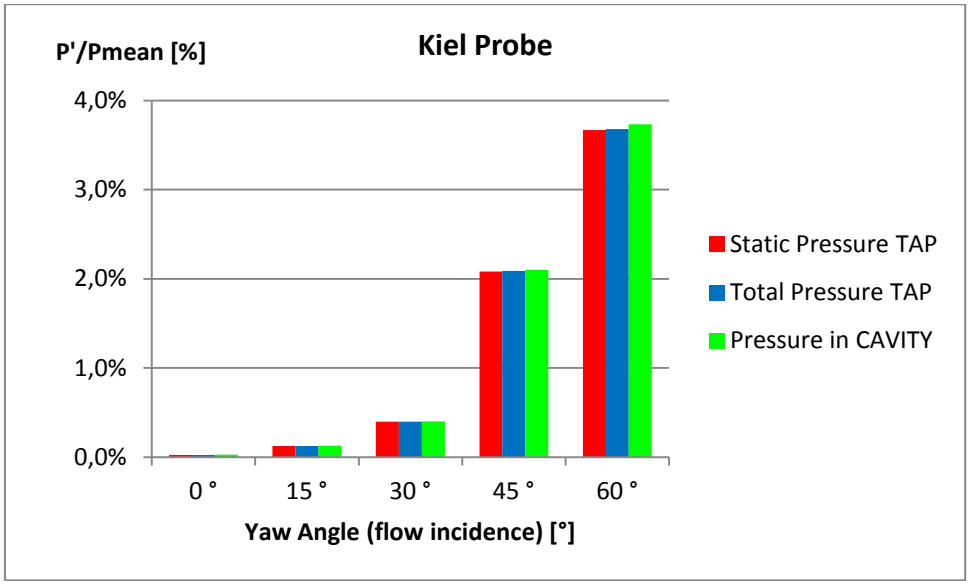

Figure 4.30. Impact of pressure fluctuations on the mean value in relative terms for the Kiel probe.

A part from absolute values, which might be very sensitive to the turbulence model, three aspects are interesting to notice:

1) Even if small, pressure fluctuations induced by vortices seem to be able to reach the end of the cavity, thus they might introduce disturbances in the recorded pressure signal.

2) Pressure disturbances induced by vortex shedding increase in magnitude with the angular position of the tap, in agreement with experimental evidence found by Rodriguez [20]. This is because the pressure port gets closer to the separation point.

3) The presence of the Kiel seems to have also the effect to mitigate the impact of vortex induced perturbations on pressure readings, but in a limited angular range. The higher pressure fluctuating component found for 45 and 60 degrees of incidence might be explained with the presence of a circulation bubble inside the Kiel shield. This is clearly evident in contours representation, for example in terms of Mach number. When the incidence is smaller the flow is more uniform and at rest inside the Kiel. Between the two cases represented below, unsteady pressure fluctuations are stronger where the bubble is more prominent. Whether it is a real effect or just a numerical solution still need to be demonstrated.

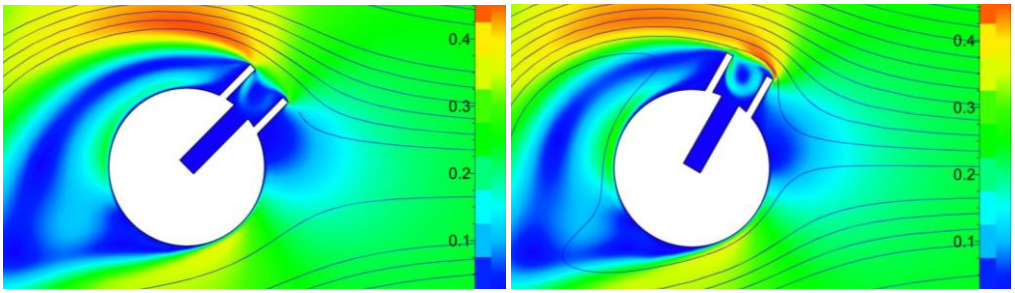

Figure 4.31. Details of Mach number contours for Kiel probe immersed in a flow with angular incidence of 45° and 60°. Contours correspond to a point which is at the 40% of the period length, based on the lift frequency and assuming that each period begins when the lift force reaches its time mean value.

Again from these numbers it seems that 30° is a sort of critical incidence between different aerodynamics phenomena for this kind of profile. The frequency of pressure fluctuations for 30° is about 22% smaller than what was found at 15° of angular incidence. Apparently, with increasing flow incidence from zero to 30° the frequency decreases significantly. For higher incidence (45° and 60°), the frequency increases, at a lower rate. Between few cases simulated, the one at 30° is a minimum. The structure of the wake, and probably also dynamics of dethatching vortices change after a sort of critical angular incidence is overtaken. If this is true, this peculiar angular incidence might be around 30°.

Chapter 5

Preliminary tests and conclusion

Two prototypes have been manufactured and preliminary tests executed. At the moment this thesis is written, preliminary testing activities are still ongoing thus available results are scarce. Nevertheless it is possible to withdraw some conclusions on the overall work.

5.1 Prototypes and preliminary tests

Prototypes heads are shown in the following pictures. Even though figure 5.2 is less accurate, it gives a better perception of the probe actual dimensions, thanks to the 1 € coins which is next to the probe head

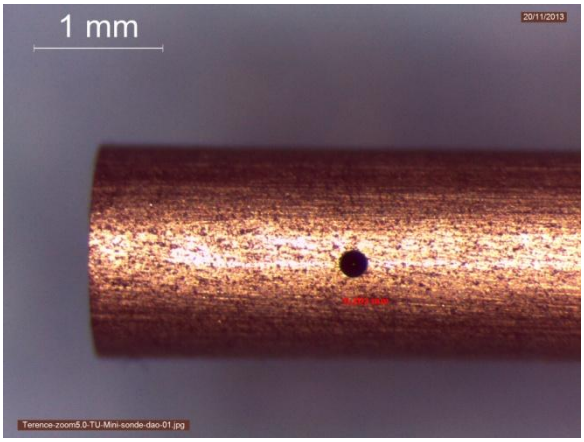

Figure 5.1. Detail of the prototype single hole cylindrical probe.

Figure 5.2. The single hole cylindrical probe next to a 1 € coin.

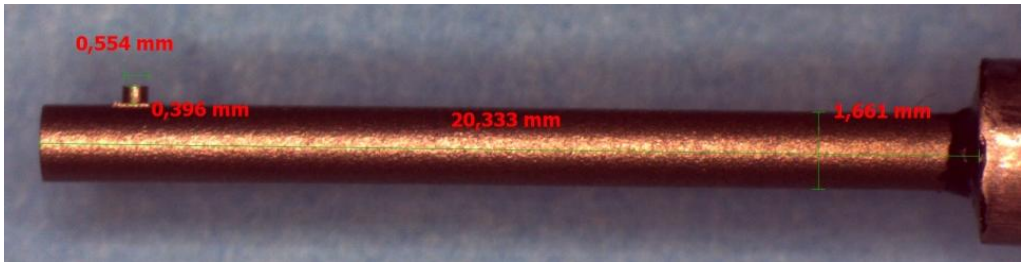

Figure 5.3. Detail of the kiel probe prototype.

The determination of calibration maps will be done with an automatic facility capable to acquire several points with very small uncertainty on the angular position. Dynamic performances will be assessed exciting probes in a shock tube. But the first step to do consists of preliminary tests in order to confirm or reject the design for further probes manufacturing. If preliminary test confirm the design, it will be possible to proceed with thorough probe performances mapping.

To assess angular sensitivity both probes have been tested using the calibrated nozzle shown in figure 5.4. The probe head is placed in the jet core and is rotated from an angular position of approximately -90° to +90° with respect to the alignment of the hole with the jet direction. Total pressure, Mach number, temperature and ambient pressure are monitored.

Figure 5.4. Single hole cylindrical probe and the calibrated nozzle used for preliminary testing.

Preliminary tests have been conducted at constant Mach number 0.27. At each angular position, the voltage mean value have been recorded. Figure 6.5 shows typical probe response in terms of volt per angular position.

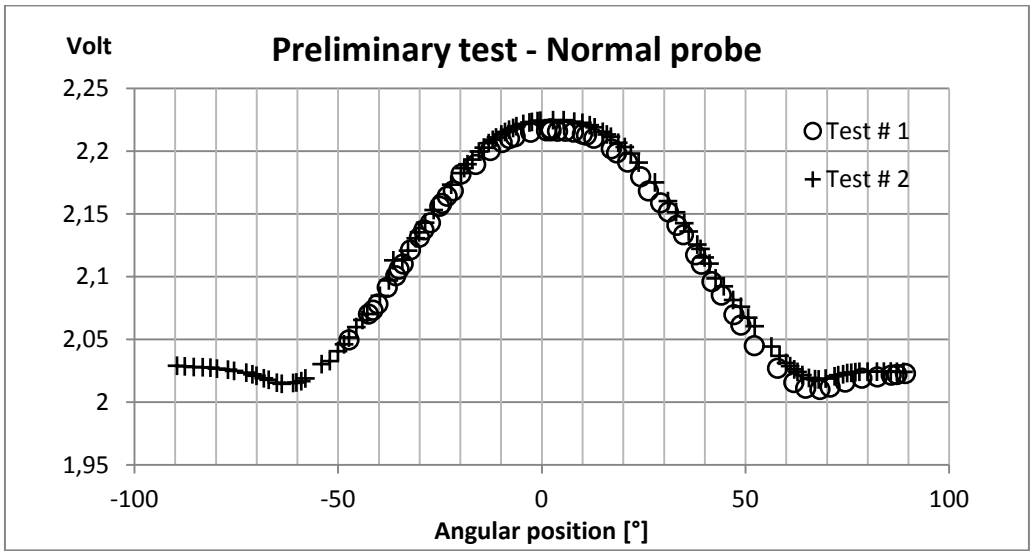

Figure 5.5. Preliminary angular sensitivity test on the single hole cylindrical probe.

The pressure measured by the probe is obtained applying the sensor electric calibration law.

5.2 Cylindrical probe preliminary results

From figure 5.5 we can conclude that the probe behaviour is in line with the expected trend. An evaluation of the probe performance can be done again in terms of the calibration coefficient *Kpt* which can be compared with the reference design and CFD results.
With respect to the reference design, the comparison is satisfactory. There is a very good correspondence in the inner part of the curve, for low angular incidence.
The points of inflection, which are located near the separation region are close to the same angular position of the original probe. Maximum values are smaller and the curve opens thus changing the range of linearity of the calibration coefficient. The decrease in angular sensitivity is limited to the external part of the curve. This differences might be attributed to the smaller tap and external probe diameters, but the overall result can be retained satisfactory.

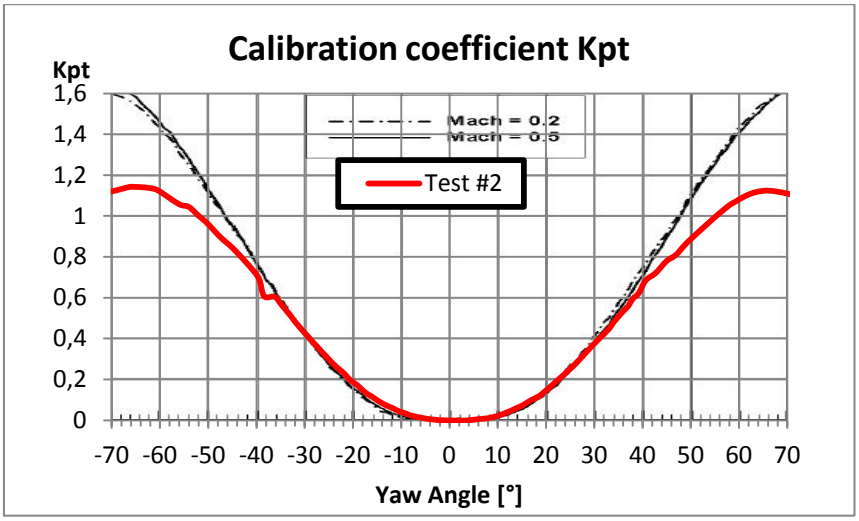

Figure 5.6. Comparison between the calibration coefficient *Kpt* obtained with the preliminary tests and the calibration curve of the probe developed at Politecnico di Milano [1].

CFD results are more imprecise: experimental data of the normal probe seems to be closer to the numerically predicted performance of the Kiel instead of the normal probe. This fact can be seen as a confirm that the numerical model is affected by inaccuracies in terms of absolute values as already outlined. Unfortunately, the more interesting comparison in terms of relative gain of the Kiel probe with respect to the normal, is not possible at the moment, because of the lack of good data regarding Kiel probe performance.

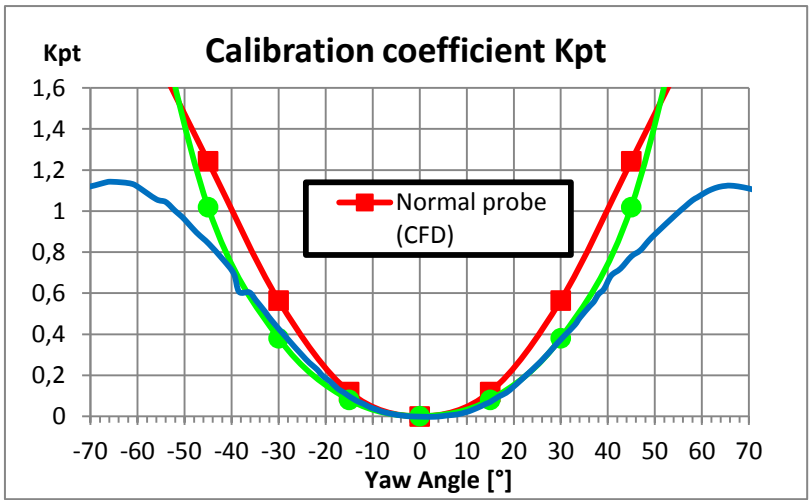

Figure 5.7. Comparison between the calibration coefficient *Kpt* obtained with the preliminary tests and values determined numerically with the CFD.

5.3 Kiel probe preliminary results

As already anticipated in the previous paragraph, so far no good data are available to evaluate the Kiel probe performances. Preliminary testing in fact highlighted an unexpected behaviour which is currently being investigated. From preliminary testing, output curves are not symmetrical and are characterized by the presence of some peaks. Moreover, the behaviour seems to depend also on the direction of probe rotation during the test: the anomalous peak always appears during the first half of the test.
Data represented in figure 5.8 in fact have been taken rotating the probe from negative to positive angles during test # 2 and vice versa for test # 3.

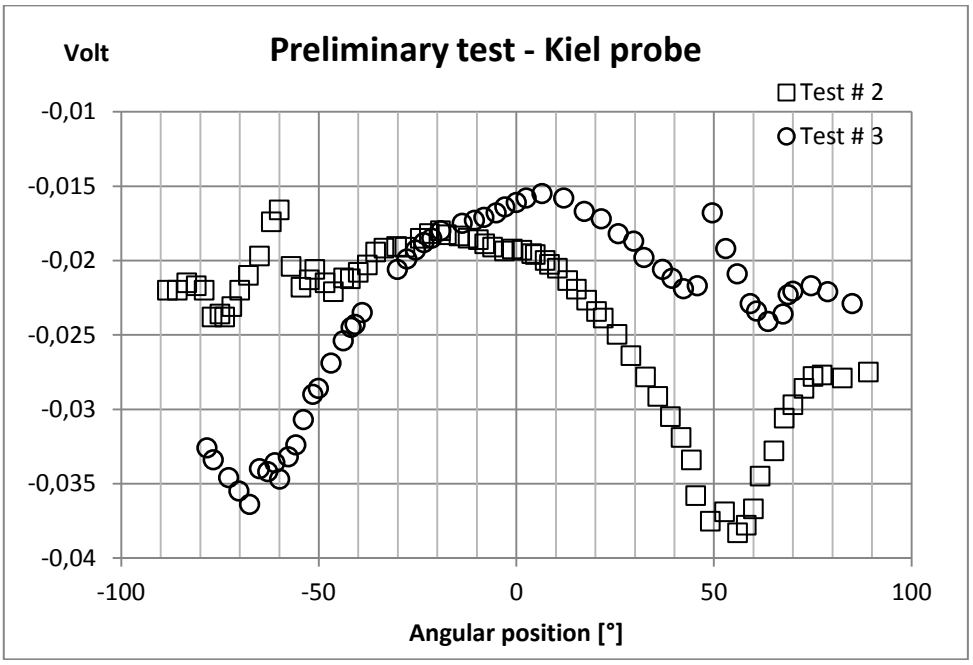

Figure 5.8. Preliminary angular sensitivity test on the Kiel probe.

If this behaviour will be confirmed by new tests, among the possible explanations there are two major hypothesis:
1) imperfections and errors in the manufacturing,
2) wrong design of the Kiel

In terms of manufacturing, some little deficiencies are visible at the microscope on the external surface. The little burr highlighted in figure 5.9 probably does not alter significantly the flow, because it is very small respect to the Kiel, but it casts doubt on the precision of the manufacturing inside the Kiel and the cavity.

The presence of such little imperfections inside the probe and eventual failures in the sensor positioning and sealing might alter the measurement completely. Nonetheless, if the asymmetry of the curve will be found to be systemic and not a random error this explanation sounds not reasonable.

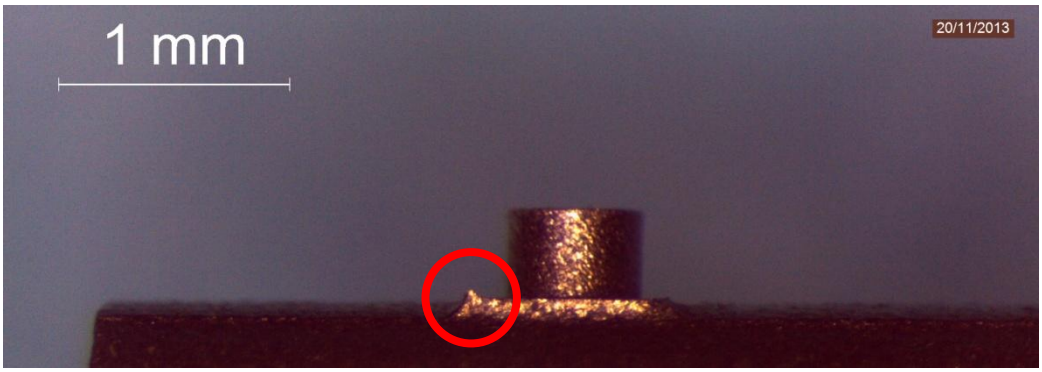

Figure 5.9. Detail of the kiel probe external surface.

If the asymmetry of the curve is a peculiar characteristic of the probe, and if it is really dependent from the sequence of angular positions during tests, the explanation is more likely to be found looking at probe aerodynamics. Although approximate, the CFD model found a sort of recirculation bubble inside the Kiel, which was changing with the flow incidence. If this phenomenon is real, it could explain the asymmetry in the pressure readings.

The curves depicted above in figure 5.8, have been obtained rotating the probe on the nozzle from -90° to +90°, and vice versa. The peak has been detected only in the first part of the test. Starting from -90° (but also from +90°) as long as the Kiel gets aligned with the flow, the bubble might establish inside the Kiel and affect the measurement. After a critical point, as the flow angle gets smaller, there is a sharp drop in the pressure and the trend in the curve changes, becoming more flat. In the second part of the test, from the aligned position (0°), towards increasing angles, this phenomenon is absent. It might be that the stagnating condition which has establishes inside the Kiel at low incidence prevents the formation of the circulation bubble. Thus the evolution of this phenomenon might depend on the history of flow angular incidence. In fact it happens on both sides, depending on the probe turning direction and not on any geometrical feature.

This critical position is at about 50°. Additional tests confirmed that this peak is not found if the angular span investigated is more narrow, as shown in figure 5.10, regarding a test that started with the probe at about -30°.

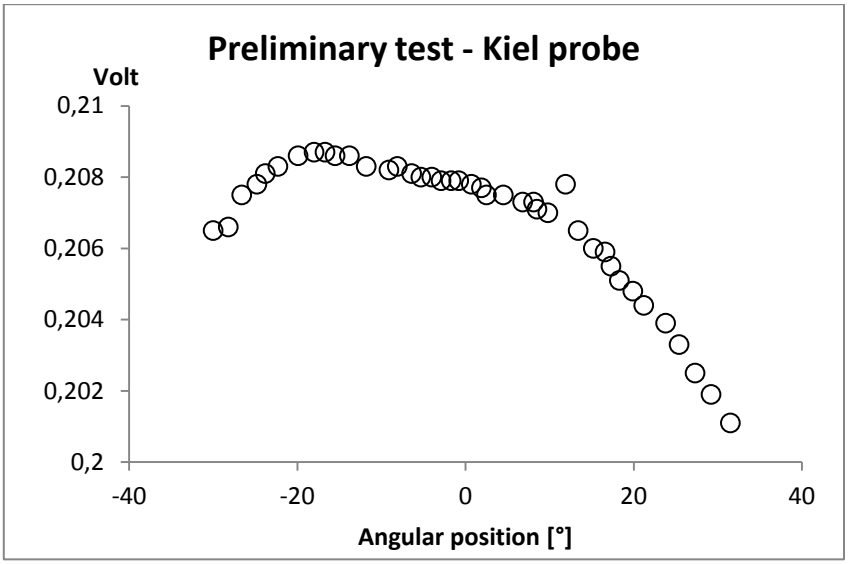

Figure 5.10. Preliminary angular sensitivity test on the Kiel probe.

This explanation might be completely wrong, and is inspired by the observation of the CFD results, which are subjected to approximations and limitations. A radical change in the boundary layer structure, especially inside the Kiel, might explain the sharp drop in the pressure readings and its "history dependence".
All these tests are affected by thermal drift, because they have been performed immediately after the measurement system was switched on.

5.4 Conclusions and future work

The numerical model adopted in the present investigation can be used to estimate global performances but still needs to be validated with experimental results. Further sensitivity analysis might be conducted but probably the uncertainty would still remain high and prevent its use for details investigation.

In spite of its potential, if tests will confirm what has been argued so far, the Kiel probe, cannot be considered a success. Even if thermal drift will be verified and removed, the presence of unexpected peaks and their dependence on the history of flow directions makes this probe not reliable for measurements in turbomachinery.
A thorough study of its aerodynamic would be very interesting, for better understanding and further development of improved geometries.
Probably, a smoother inlet, like a converging duct which goes from the Kiel external profile until the line beginning could improve the stagnation region and the pressure readings, but further studies are necessary. Another option is to keep a constant inner diameter through the kiel and the line, as in a cylinder.

In terms of angular sensitivity, the normal probe is successful. It is adequate for steady measurements and if dynamic tests will confirm expectations, it can be used also for fast response measurements. So far there is no reason to doubt about it. To the best knowledge of the author, the single hole probes developed at Politecnico di Milano, and ETH Zurich have been so far the smallest single hole transverse cylindrical probes in the world with their 1.8 mm external diameter. The new probe sets a new record and is probably the smallest (1.6 mm - 11% reduction in diameter), obtained at a very competitive cost.

This work is still going on at the Von Kármán Institute, thanks to Dr. Sergio Lavagnoli and Angela Morelli which are completing preliminary tests, dynamic characterization and improving the calibration procedure.

APPENDIX A

Unsteady convergence Matlab® script

In this appendix the Matlab® script developed for the unsteady convergence assessment is reported.

Name of the original file :Unsteady_convergence_load_08.m

```
%%%%%%%%%%%%%
%%%%%%%%%%%%% The code is not perfect, but you can always improve it if you
%%%%%%%%%%%%% want. All settings are in the first lines. Read the
%%%%%%%%%%%%% comments and pay attemption to the message appearing in the
%%%%%%%%%%%%% command window during execution.
%%%%%%%%%%%%% Info and bugs report @ giovanni.bonetti@mail.polimi.it
%%%%%%%%%%%%%
%%%%%%%%%%%%% It seems to work properly, but I give you no guarantee about
%%%%%%%%%%%%% results.           GOOD LUCK!

clc
clear all
close all
format short

%%%%%%%%%%%%%%%%%%%%%%%%%%%%%%%%%%%%%%%%%%%%%%%%%%%%%%%%%%%%%%%%%%%%%%%%%%%%%%%
%%%%%%%%%%%%%%%%%%%%%%%%%%%%%%%%%%%%%%%%%%%%%%%%%%%%%%%%%%%%%%%%%%%%%%%%%%%%%%%
%%%%%%%%%%%%    SET OPERATING PARAMETERS HERE

%%%%%%%set here the name of the input file and the input folder
test_file='Static_pressure_integrated_probe_raw_10000_13000.txt';
input_folder='Data_to_load\';

%%%%% data must be in a single .txt file gathered in column.
%%%%% set here the column indexes for time and the quantity to be read
%%%% set the variable name to avoid overwrite output files generated for
%%%% different quantities.
TIME_INDEX=1;
VARIABLE_INDEX=3;
VARIABLE_NAME='LIFT';

%%%%%%%set here the name of the output file and the output folder
output_folder='Convergence_output\';
%%% set the name of the output excel file
name_output_file='output_summary_';

%%%%%%% set here an oversampling coefficient if you want to increase the
%%%%%%% number of points available in the dataset. The code will perform
%%%%%%% spline interpolation between existing points.
%%%%%%% K_interp is defined as
%%%%%%% K=dt_signal/dt_interp=(Nof_points_interp-1)/(Nof_points_signal-1)
K_interpolation=10;
```

```
%%%%%%%     END OF OPERATING PARAMETERS INPUT SECTION
%%%%%%%%%%%%%%%%%%%%%%%%%%%%%%%%%%%%%%%%%%%%%%%%%%%%%%%%%%%%%%%%%%%%%%%%%%%
%%%%%%%%%%%%%%%%%%%%%%%%%%%%%%%%%%%%%%%%%%%%%%%%%%%%%%%%%%%%%%%%%%%%%%%%%%%

%%%%%LOADING DATA
data=load([input_folder test_file]);
time=data(:,TIME_INDEX);
variable_to_test=data(:,VARIABLE_INDEX);
nof_points=length(time);

t=time';
true_y=variable_to_test;
dt_original=t(1,2)-t(1,1);

disp(' ');
fprintf('The time discretization step in the original dataset is:  [s]
%E\n',dt_original);
fprintf('The original number of points is: %i\n',nof_points);

%%%%INTERPOLATION SECTION
%%%%% THIS SECTION PERFORM SPLINE INTERPOLATION ON THE DATSET TO INCREASE
%%%%% THE NUMBER OF SAMPLES AVAILABLE.
%%%%% comment this section if not needed
dt_interpolation=dt_original/K_interpolation;
delta=round(dt_original/dt_interpolation);
n_of_interpolating_points=(nof_points-1)*delta+1;
interpolating_time=zeros(n_of_interpolating_points,1);
i=1;
interpolating_time(i)=time(1,1);
for i=2:n_of_interpolating_points
    ii=i-1;
    interpolating_time(i)=interpolating_time(1)+ii*dt_interpolation;
end
y_interpolated=interp1(time,true_y,interpolating_time,'spline');
t=interpolating_time';
true_y=y_interpolated;
%%%%%%% end of interpolation section

disp(' ');
fprintf('The time discretization step after the interpolation is:  [s]
%E\n',dt_interpolation);
fprintf('The new number of points is: %i\n',n_of_interpolating_points);

%%% setting an index for figures
fn=1;

%%%%%%%%%%%%%%%%%%%%%%%%%%%%%%%%%%%%%%%%%%%%%%%%%%%%%%%%%%%%%%%%%%%%%%%%%%%
%%%%%%%%%%%%%%%%%%%%%%%%%%%%%%%%%%%%%%%%%%%%%%%%%%%%%%%%%%%%%%%%%%%%%%%%%%%

%%%%%%          STARTING THE SIGNAL PORCESSING HERE
%%%% A FIRST FFT IS PERFORMED AND THE PERIOD FREQUENCY IS ESTIMATED

nof_samples=length(true_y);
n=nof_samples;
fs=round((nof_samples-1)/(t(1,end)-t(1,1)));
true_y_fluct=true_y-mean(true_y);
y_FFT=fft(true_y_fluct,nof_samples);
amplitude=abs(y_FFT);
power=(abs(y_FFT).^2)/n;
freq_range=(0:n-1)*(fs/(n-1));

%%%%%ACQUIRED signal and relative FFT ARE PLOTTED ON SCREEN FOR A VISUAL CHECK

figure(fn);
fn=fn+1;
```

```
subplot(1,2,1);
plot(t,true_y,'b-','LineWidth',1)
xlabel('t [s]')
ylabel('Y')
title('{\bf INPUT SIGNAL}');

subplot(1,2,2);
plot(freq_range(1:floor(n/2)),power(1:floor(n/2)));
xlabel('Frequency (Hz)')
ylabel('FFT Power')
title('{\bf HALF PERIODOGRAM}')
hold on
temp_name=sprintf('Tested_signal - %s',VARIABLE_NAME);
saveas(gcf,[output_folder temp_name],'fig')

%%%%TO PERFORM DATA ANALYSIS THE SIGNAL MUST BE SPLITTED. THE SIGNAL MUST
%%%%BE SPLITTED IN PERIODS HAVING APPROPRIATE LENGTH CORRESPONDING TO THE
%%%%LOWEST FREQUENCY SEEN. THE OVERALL SIGNAL AND GLOBAL FFT PLOT GIVES
%%%%THE USER SOME REFERENCES TO GUESS WICH ARE THE DOMINANT FREQUENCYES IN
%%%%THE SIGNAL. TO PROCEDE, THE USER MUST TYPE THE FREQUENCY HE WANT TO USE
%%%%FOR SUBSEQUENT CONVERGENCE ANALYSIS. SINCE THERE COULD BE MORE THAN ONE
%%%%PERIODIC ARMONIC, THE USER CAN GIVE AS INPUT A FEW FREQUENCY VALUES OR
%%%%JUST ONE. ONE CAN BE TYPED AS A NUMBER, MORE VALUES MUST BE GIVEN IN
%%%%BETWEEN SQUARED BRACKETS. WHEN MORE VALUES ARE GIVEN, THE CODE WILL USE
%%%%THE LOWEST TO COMPUTE THE PROPER PERIOD FOR SIGNAL SPLITTING.

disp(' ');
disp('Which are the frequency you are looking for???');
disp('WARNING: No more than 10 values ');
disp('WARNING: The code will split the signal using the minimun frequency ');
disp('WARNING: If you type multiple values put them in between squared brackets
');
prompt = 'Tipe the value/values in Hz - [freq1 freq2 .... freqN] ';
freq_of_interest = input(prompt);


%%%%%%COMPUTING PARAMETERS FOR SIGNAL SPLITTING IN SUBSEQUENT PERIODS
minimum_freq=min(freq_of_interest);
target_period=1/minimum_freq;
dt=(t(1,end)-t(1,1))/(length(t)-1);
intervals_per_period=round(target_period/dt);
SAMPLE_PER_PERIOD=intervals_per_period+1;
N_of_periods=floor(n/(SAMPLE_PER_PERIOD));
%%% change floor to round in this line if your signal is made of an exact
%%% number of periods. Otherwise you could miss the last period.
%%% It is also important, if this happens, that you add just one more point
%%% at the end of the data series, to avoid encounter this problem
%%% N_of_periods=round(n/(SAMPLE_PER_PERIOD));

disp(' ');
fprintf('The user has typed as frequency:  [Hz] %E\n',freq_of_interest);
fprintf('The code has chosen as minimum: [Hz] %E\n',minimum_freq);
fprintf('The corresponding dt used as target period is: [s]
%E\n',target_period);
fprintf('Number of intervals per period: %i\n',intervals_per_period);
fprintf('Number of corresponding samples: %i\n',SAMPLE_PER_PERIOD);


%%%%EXTRACTION OF CONSECUTIVE SAMPLES TO BE COMPARED
for i=1:(N_of_periods-1)
    period(i)=i;
    t1(i,(1:SAMPLE_PER_PERIOD))=t(1+(i-
1)*intervals_per_period:(1+i*intervals_per_period));
```

```
    y1(i,(1:SAMPLE_PER_PERIOD))=true_y(1+(i-
1)*intervals_per_period:(1+i*intervals_per_period));

t2(i,(1:SAMPLE_PER_PERIOD))=t(1+i*intervals_per_period:(1+(i+1)*intervals_per_pe
riod));

y2(i,(1:SAMPLE_PER_PERIOD))=true_y(1+i*intervals_per_period:(1+(i+1)*intervals_p
er_period));
    y1_fluctuating(i,:)=y1(i,:)-mean(y1(i,:));
end
    y1_fluctuating(N_of_periods,:)=y2(i,:)-mean(y2(i,:));
%%%%END OF CONSECUTIVE PERIODS EXTRACTION HERE


    %%% Plot extracted data for a visual check.
    %%% The splitted signal is plotted onscreen for a visual check.
    %%% In this way the user has the chance to check if the number of
    %%% points used per period is correct or not.
    %%% After the plot will be asked to give as input the correct
    %%% number of points.

    %%%BE CAREFUL BECAUSE FOR PRACTICAL REASON THE LAST ONE OR TWO PERIODS
    %%%MIGHT BE MISSING FROM THE PLOT (BUT NOT IN THE PARAMETERS COMPUTATION)
    %%%IT'S JUST THE WAY I USED TO PLOT CONSECUTIVE PERIODS WITH DIFFERENT
    %%%COLOURS THAT MAKE THIS HAPPEN. IT'S NOT A PROBLEM FOR LONG SIGNAL, COULD
    %%%LOOK STRANGE IF YOU COMPARE JUST TWO OR THREE PERIODS.

figure(fn)
fn=fn+1;
for i=1:2:(N_of_periods-2)
plot(t1(i,:),y1(i,:),'b-','LineWidth',2)
hold on
i=i+1;
plot(t1(i,:),y1(i,:),'g-','LineWidth',2)
end
xlabel('t [s]')
ylabel('Y')
title('{\bf SPLITTED SIGNAL}');
hold off

%%%%%%%% PLOT onscreen informations:
%%%% A bunch of important informations about the splitted
%%%% periods are given in the command window.
%%%% According to them and having a look at the previous plot
%%%% the user can decide which is the correct number of points to be used
%%%% for correct periods splitting.
%%%% The user must insert the number of points he wants to use to continue.

disp(' ');
disp('#######       WARNING !!!!!       #######');
disp('Pay attemption at this step since it is critical.');
disp('Have a look at the number of samples used by the code (you will find it
some lines above this message).');
disp('Check the last plot generated and verify if periods are splitted
correcltly.');
disp('If they are good, you have to confirm the number of samples per period
used by the code.');
disp('If not, you have to correct this value. The plot is made to help you.');
disp('You can check and count how many points add/substract from the default
value used by the code');
disp(' ');
prompt = 'Type the correct number of points you want ';
new_SAMPLE_PER_PERIOD = input(prompt);

%%%%%%% Accrording to the number of points typed by the user the
```

```
%%%%%%% main parameters for signal splitting are computed again
%%%%%%% and the signal splitting procedure is repeated

new_target_period=dt*(new_SAMPLE_PER_PERIOD-1);
new_target_freq=1/new_target_period;
new_intervals_per_period=new_SAMPLE_PER_PERIOD-1;
new_N_of_periods=floor(n/(new_SAMPLE_PER_PERIOD));
%%% change floor to round in this line if your signal is made of an exact
%%% number of periods. Otherwise you could miss the last period.
%%% It is also important, if this happens, that you add just one more point
%%% at the end of the data series, to avoid encounter this problem
%%% new_N_of_periods=round(n/(new_SAMPLE_PER_PERIOD));

disp(' ');
fprintf('The new target frequency is: [Hz] %E\n',new_target_freq);
fprintf('The new corresponding dt used as target period is: [s]
%E\n',new_target_period);
fprintf('New number of intervals per period: %i\n',new_intervals_per_period);
fprintf('New number of corresponding samples: %i\n',new_SAMPLE_PER_PERIOD);
disp(' ');
fprintf('Number of periods detected to be compared: %i\n',new_N_of_periods);

clear t1
clear y1
clear t2
clear y2
clear y1_fluctuating
clear period

    %%%%NEW EXTRACTION OF CONSECUTIVE SAMPLES TO BE COMPARED
for i=1:(new_N_of_periods-1)
    period(i)=i;
    t1(i,(1:new_SAMPLE_PER_PERIOD))=t(1+(i-
1)*new_intervals_per_period:(1+i*new_intervals_per_period));
    y1(i,(1:new_SAMPLE_PER_PERIOD))=true_y(1+(i-
1)*new_intervals_per_period:(1+i*new_intervals_per_period));

t2(i,(1:new_SAMPLE_PER_PERIOD))=t(1+i*new_intervals_per_period:(1+(i+1)*new_inte
rvals_per_period));

y2(i,(1:new_SAMPLE_PER_PERIOD))=true_y(1+i*new_intervals_per_period:(1+(i+1)*new
_intervals_per_period));
    y1_fluctuating(i,:)=y1(i,:)-mean(y1(i,:));
end
    y1_fluctuating(new_N_of_periods,:)=y2(i,:)-mean(y2(i,:));
    %%%%END OF CONSECUTIVE PERIODS EXTRACTION HERE

%%%%%%%%%%%%%%%%%%%%%%%%%%%%%%%%%%%%%%%%%%%%%%%%%%%%%%%%
%%%%%%%%%%%%SINGLE PERIOD FFT BLOCK
%%%% FFT is performed over each period of the splitted signal

n=new_intervals_per_period +1;
for i=1:new_N_of_periods
    period_FFT(i,:)=fft(y1_fluctuating(i,:));
    power_FFT(i,:)=(abs(period_FFT(i,:)).^2)/n;
    freq_range=(0:n-1)*(fs/(n-1));
end

%%%% The intervals between each frequency is extracted for being used
%%%% later to detect the location of frequency in the frequency vector
DF=freq_range(2)-freq_range(1);

%%%% EXTRACTING AMPLITUDE AND PHASE VALUE FROM DFT
amplitude=abs(period_FFT);
phase=angle(period_FFT);
```

```
phase_deg=phase.*(360/(2*pi));

%%%% A NEW SERIES OF PLOT IS MADE TO ALLOW THE USER TO CHECK THE FINAL
%%%% SPLITTED PERIOD AND TO SEE THE FFT PARAMETERS COMPUTED FOR EACH PERIOD

figure(fn);
fn=fn+1;

%%%TOP LEFT PLOT IS THE SPLITTED SIGNAL WITH THE CORRECT NUMBER OF POINTS
%%%BE CAREFUL BECAUSE FOR PRACTICAL REASON THE LAST ONE OR TWO PERIODS
%%%MIGHT BE MISSING FROM THE PLOT (BUT NOT IN THE PARAMETERS COMPUTATION)
%%%IT'S JUST THE WAY I USED TO PLOT CONSECUTIVE PERIODS WITH DIFFERENT
%%%COLOURS THAT MAKE THIS HAPPEN. IT'S NOT A PROBLEM FOR LONG SIGNAL, COULD
%%%LOOK STRANGE IF YOU COMPARE JUST TWO OR THREE PERIODS.

subplot(2,2,1);
for i=1:2:(new_N_of_periods-2)
plot(t1(i,:),y1(i,:),'b-','LineWidth',2)
hold on
i=i+1;
plot(t1(i,:),y1(i,:),'g-','LineWidth',2)
end
xlabel('t [s]')
ylabel('Y')
title('{\bf SPLITTED SIGNAL}');
hold off

%%%%%TOP RIGHT PLOT IS A PLOT OF THE PERIODS SUPERIMPOSED IN THE SAME
%%%%%WINDOW. WHEN PERIODS ARE PERFECT THEY TEND TO APPEAR AS A SIGNLE THIN
%%%%%LINE, BECAUSE THEY MATCH EXACTLY EACH OTHER IN EVERY POINTS.

subplot(2,2,2);
for i=1:(new_N_of_periods-1)
    t1_from_zero(i,:)=t1(i,:)-t1(i,1);
end
for i=1:1:(new_N_of_periods-1)
plot(t1_from_zero(i,:),y1(i,:))
hold on
end
xlabel('t [s]')
ylabel('Y')
title('{\bf SUPERIMPOSED PERIODS}');
hold off

%%%%% BOTTOM LEFT PLOT IS THE DFT AMPLITUDE OF EVERY PERIOD
%%%%% THIS IS THE PLOT THE USER SHOULD LOOK AT TO CHOOSE WHICH FREQUENCY HE
%%%%% WANTS TO USE TO COMPUTE PHASE AND AMPLITUDE CONVERGENCE PARAMETER
%%%%% EVERY PERIOD IS PLOTTED WITH A DIFFERENT COLOUR

subplot(2,2,3);
y_plot=amplitude';
aux=freq_range';
for i=1:new_N_of_periods
    x_plot(:,i)=aux(:,1);
end
    plot(x_plot,y_plot)
    xlim([freq_range(1) freq_range(end)/2]);
    xlabel('Frequency (Hz)')
    ylabel('Amplitude DFT')
    title('{\bf DFT AMPLITUDE - HALF SPECTRUM}')

%%%%% BOTTOM RIGHT PLOT IS THE DFT PHASE OF EVERY PERIOD
%%%%% THIS IS THE MOST TRICKY PLOT SINCE THE PHASE IS VERY SENSITIVE TO
%%%%% DISCRETIZATION INTERVAL AND IT CAN LOOK VERY STRANGE.
%%%%% AGAIN EACH PERIOD IS PLOTTED WITH A DIFFERENT COLOUR
```

```
    subplot(2,2,4);
    y_plot=phase_deg';
    plot(x_plot(:,2:end),y_plot(:,2:end),'o')
    xlim([freq_range(1) freq_range(end)/2]);
    xlabel('Frequency (Hz)')
    ylabel('Phase DFT')
    title('{\bf DFT PHASE - HALF SPECTRUM}')

    temp_name=sprintf('Split_periods_plots - %s',VARIABLE_NAME);
    saveas(gcf,[output_folder temp_name],'fig')

%%%%%% FREQUENCY OF INTEREST

%%%%% ACCORDING TO THE LAST PLOT ABOUT THE SPLITTED SIGNAL THE USER CAN NOW
%%%%% CHOOSE WHICH FREQUENCIES TO BE USED FOR AMPLITUDE, PHASE AND DFT
%%%%% INDICATORS. THE CODE WILL ASK IN THE COMMAND WINDOW TO TYPE
%%%%% FREQUENCY VALUES. THE CODE IS CAPABLE TO HANDLE UP TO 10 FREQUENCIES.
%%%%% IF WE LOOK FOR JUST ONE VALUE WE HAVE TO TYPE THE NUMBER AND PRESS
%%%%% ENTER. IF WE ARE INTERESTED IN MORE THAN ONE (BECAUSE OF SEVERAL
%%%%% HARMONICS OR BECAUSE PEAKS ARE DISCRETISED AS A BAND OVER A FEW
%%%%% FREQUENCIES) VALUES MUST BE GIVEN IN BETWEEN SQUARED BRACKETS.

%%%%%           WARNING             %%%%
%%%%% The frequencies computed by FFT are discretised whith a minimum df
%%%%% between each values. Therefore it's possible to detect just
%%%%% discretised values. The user can read frequency values from the
%%%%% FFT plots and type those values as input. The input value could be
%%%%% even a bit different from the real discretised values stored in the
%%%%% frequency vector. The code is capable to detect the corresponding
%%%%% discretised value closer to the one typed by the user, and will
%%%%% compute corresponding indicators. Therefore it is possible that the
%%%%% user ask to look for 13800 Hz, while the codse consider 13842. The
%%%%% exact frequencies taken from the spectrum can be read form the FFT
%%%%% plots and are reported in the excel output summary file.


%%%%%% QUESTIONS ARE TYPED IN THE COMMAND WINDOW AND THE CODE WAIT FOR USER
%%%%%% VALUES INPUT.
disp(' ');
disp('According to the new FFT plot,');
disp('Which are the frequency you are looking for???');
disp('WARNING: No more than 10 values ');
disp('WARNING: If you type multiple values put them in between squared brackets
');
prompt = 'Tipe the value/values in Hz - [freq1 freq2 .... freqN] ';
freq_of_interest = input(prompt);

n_of_frequency=length(freq_of_interest);

for i=1:n_of_frequency
locations_of_frequency(i) = round(freq_of_interest(i)/DF)+1;
end

%%%%%%%% THE FOLLOWING LOOP SET FREQUENCY LABELS FOR LATER USE IN THE EXCEL
%%%%%%%% OUTPUT AND ALSO FOR PLOT ONSCREEN INFORMATION  NOW


    frequency_label(1,1)=freq_range(1,locations_of_frequency(1,1));
    frequency_label(1,2)=freq_range(1,locations_of_frequency(1,1));
    Visual_label(1,1)=freq_range(1,locations_of_frequency(1,1));
    kk=2;
for i=2:n_of_frequency
    j=2*i-1;
    Visual_label(1,kk)=freq_range(1,locations_of_frequency(1,i));
```

```
    kk=kk+1;
    frequency_label(1,j)=freq_range(1,locations_of_frequency(1,i));
    j=2*i;
    frequency_label(1,j)=freq_range(1,locations_of_frequency(1,i));
end
%%%%%%%% END OF FREQUENCY LABELS SECTION


disp(' ');
fprintf('The user has typed as frequency:  [Hz] %E\n',freq_of_interest);
fprintf('The code has detected in the frequency vector these: [Hz]
%E\n',Visual_label);
disp('Indicators will be computed with the discretized detected values');
disp(' ');
disp('§§§§        WAIT A SECOND, PLEASE       §§§§§');
disp(' ');
%%%%%%%%%%%%%%%%%%%%%%%%%%%%%%%%%%%%%%%%%%%%%%%%%%%%%%%%%%%%%%%%%%%%%%%
%%%Convergence indexes computation START HERE

%%%%MEAN (fM)

for i=1:(new_N_of_periods-1)
    mean1=mean(y1(i,:));
    mean2=mean(y2(i,:));
    fM(i)=1-abs(1-mean2/mean1);
end

%%%%CCF at zero time lag (fS)

for i=1:(new_N_of_periods-1)
    mean1=mean(y1(i,:));
    y1_fluct=y1(i,:)-mean1;
    mean2=mean(y2(i,:));
    y2_fluct=y2(i,:)-mean2;

CCF(i)=((sum(y1_fluct.*y2_fluct))/new_intervals_per_period)/(((sum((y1_fluct.^2)
)*sum((y2_fluct.^2)))^(0.5))/new_intervals_per_period);
    fS(i)=abs(CCF(i));
end

%%%%%FFT AMPLITUDE (fA)

fa_lim=size(amplitude);
for j=1:(fa_lim(2)-1)
    for i=1:(new_N_of_periods-1)
        A1(j)=amplitude(i,j);
        A2(j)=amplitude(i+1,j);
        fA(i,j)=1-abs(1-A2(j)/A1(j));
    end
end

%%%%%FFT PHASE (fA)

for j=1:(fa_lim(2)-1)
    for i=1:(new_N_of_periods-1)
        ph1(j)=phase(i,j);
        ph2(j)=phase(i+1,j);
        fFI(i,j)=1-abs((ph2(j)-ph1(j))/pi);
    end
end

%%%%%POWER SPECTRAL DENSITY (PSD)
%%% PSD has already been calculated to make the plot.
%%% here we just define the convergence parameter
```

```
clear k_expected
clear num
k_expected=length(freq_of_interest);
num(1:new_N_of_periods)=0;
for j=1:new_N_of_periods
    for i=1:k_expected
        num(1,j)=num(1,j)+power_FFT(j,locations_of_frequency(i));
    end
end
for j=1:new_N_of_periods
    den(1,j)=sum((power_FFT(j,:))');
end
fP=num./den;
%%%%% IT'S MUPLTIPLIED BY 2 TO TAKE ACCOUND OF THE "MIRROR" SPECTRUM IN THE
%%%%% FFT THAT WAS NOT PLOTTED FOR CLARITY AND SIMPLICITY
fP=fP.*2;

%%%%%%%%%%Covergence computation parameters STOP HERE
%%%%%%%%%%%%%%%%%%%%%%%%%%%%%%%%


%%%%%%%% FINAL PLOTS

%%%%%% IN ALL OF NEXT PLOT, THE ABSCISSA IS 1,2,3... NUMBER 1 MEANS THAT
%%%%%% THE CORRESPONDING INDICATOR IS ACCOUNTED CHECKING PERIOD 2 WITH 1,
%%%%%% NUMBER 2 MEANS PERIOD 3 VERSUS 2, AND SO ON...
%%%%%% JUST THE PSD FRACTION IS REFERRED TO EACH PERIOD AND NOT AS A RATIO
%%%%%% BETWEEN CONSECUTIVE PERIODS, SO FOR THAT INDICATOR ABSCISSA 1 MEANS
%%%%%% PERIOD 1, ABSCISSA 2 MEANS PERIOD 2, ...
%%%%%% FOR PHASE FACTORS AND FREQUENCYES OF INTERESTS, THERE ARE 3 PLOTS:
%%%%%% THE FIRST ONE IS ON THE TOP RIGHT CORNER, WITH BOTH INDICATORS
%%%%%% TOGETHER (SAME COLOUR MEANS SAME PERIOD, SAME SIMBOL MEANS SAME
%%%%%% PARAMETER(PHASE OR AMPLITUDE)). IN THIS PLOT JUST 5 FREQUENCIES
%%%%%% PARAMETERS ARE PLOTTED. SINCE THE USER CAN LOOK FOR UP TO 10
%%%%%% frequencies, AND SINCE THE PRESENCE OF MANY POINTS TOGETHER ON THE
%%%%%% SAME PLOT CAN MAKE IT HARD TO BE READ, IN THE BOTTOM LINE, TWO
%%%%%% SEPARATE PLOTS OF THE SAME INDICATORS ARE MADE, SO ONE CAN SEE
%%%%%% SEPARATELY AMPLITUDE AND PHASE INDICATORS.

figure(fn)
fn=fn+1;

%%%%%delimiting the number of series to be plotted
num_of_plot=length(freq_of_interest);

%%%%%%%%%%%%PLOT MEAN FACTOR & CCF(0) & FP (PSD)
subplot(2,2,1);
plot(period,fM,'bo','LineWidth',2)
hold on
plot(period,fS,'gx','LineWidth',2)
plot(period,fP(1,1:(end-1)),'r+','LineWidth',2)
ylim([0 1]);
xlabel('Periods')
ylabel('Parameters')
title('{\bf CONVERGENCE PARAMETERS - MEAN, CCF(0), PSD fraction}');
legend('fM','fS','fP','Location','SouthEast');

%%%%%%%%%%%%PLOT DFT AMPLITUDE FACTOR & PHASE TOGETHER (5 freq MAx)
subplot(2,2,2);
i=1;
if i<=num_of_plot
j=locations_of_frequency(i);
plot(period,fA(:,j),'bo','LineWidth',2)
ylim([0 1]);
hold on
```

```
plot(period,fFI(:,j),'b+','LineWidth',2)
end
i=i+1;
if i<=num_of_plot
j=locations_of_frequency(i);
plot(period,fA(:,j),'gx','LineWidth',2)
plot(period,fFI(:,j),'go','LineWidth',2)
end
i=i+1;
if i<=num_of_plot
j=locations_of_frequency(i);
plot(period,fA(:,j),'rd','LineWidth',2)
plot(period,fFI(:,j),'r*','LineWidth',2)
end
i=i+1;
if i<=num_of_plot
j=locations_of_frequency(i);
plot(period,fA(:,j),'c*','LineWidth',2)
plot(period,fFI(:,j),'cs','LineWidth',2)
end
i=i+1;
if i<=num_of_plot
j=locations_of_frequency(i);
plot(period,fA(:,j),'ms','LineWidth',2)
plot(period,fFI(:,j),'md','LineWidth',2)
end
xlabel('Periods')
ylabel('Parameters')
title('{\bf CONVERGENCE PARAMETERS - DFT AMPLITUDE AND PHASE frequency OF
INTEREST}');
legend('fA(1)','fFI(1)','fA(2)','fFI(2)','fA(3)','fFI(3)','fA(4)','fFI(4)','fA(5
)','fFI(5)','Location','SouthEast');

%%%PLOT DFT AMPLITUDE FACTOR
subplot(2,2,3);
%%% DELIMITING PLOTTING frequency
num_of_plot=length(freq_of_interest);
aux_indexes=ones(1,num_of_plot);
subplot(2,2,3);
i=1;
if i<=num_of_plot
j=locations_of_frequency(i);
plot(period,fA(:,j),'bo','LineWidth',2)
ylim([0.85 1]);
aux_indexes(1,i)=j;
end
i=i+1;
hold on
if i<=num_of_plot
j=locations_of_frequency(i);
plot(period,fA(:,j),'gx','LineWidth',2)
aux_indexes(1,i)=j;
end
i=i+1;
if i<=num_of_plot
j=locations_of_frequency(i);
plot(period,fA(:,j),'rd','LineWidth',2)
aux_indexes(1,i)=j;
end
i=i+1;
if i<=num_of_plot
j=locations_of_frequency(i);
plot(period,fA(:,j),'c*','LineWidth',2)
aux_indexes(1,i)=j;
end
```

```
i=i+1;
if i<=num_of_plot
j=locations_of_frequency(i);
plot(period,fA(:,j),'ms','LineWidth',2)
aux_indexes(1,i)=j;
end
i=i+1;
if i<=num_of_plot
j=locations_of_frequency(i);
plot(period,fA(:,j),'b+','LineWidth',2)
aux_indexes(1,i)=j;
end
i=i+1;
if i<=num_of_plot
j=locations_of_frequency(i);
plot(period,fA(:,j),'gp','LineWidth',2)
aux_indexes(1,i)=j;
end
i=i+1;
if i<=num_of_plot
j=locations_of_frequency(i);
plot(period,fA(:,j),'k.','LineWidth',2)
aux_indexes(1,i)=j;
end
i=i+1;
if i<=num_of_plot
j=locations_of_frequency(i);
plot(period,fA(:,j),'ro','LineWidth',2)
aux_indexes(1,i)=j;
end
i=i+1;
if i<=num_of_plot
j=locations_of_frequency(i);
plot(period,fA(:,j),'c*','LineWidth',2)
aux_indexes(1,i)=j;
end
xlabel('Periods')
ylabel('Parameters')
title('{\bf  CONVERGENCE PARAMETERS - DFT AMPLITUDE frequency OF INTEREST}');
legend('fA(1)','fA(2)','fA(3)','fA(4)','fA(5)','fA(6)','fA(7)','fA(8)','fA(9)','
fA(10)','Location','SouthEast');

%%%%%PLOTTING PHASE PARAMETERS
subplot(2,2,4);
i=1;
if i<=num_of_plot
j=locations_of_frequency(i);
plot(period,fFI(:,j),'b+','LineWidth',2)
ylim([0.85 1]);
end
i=i+1;
hold on
if i<=num_of_plot
j=locations_of_frequency(i);
plot(period,fFI(:,j),'go','LineWidth',2)
end
i=i+1;
if i<=num_of_plot
j=locations_of_frequency(i);
plot(period,fFI(:,j),'rd','LineWidth',2)
end
i=i+1;
if i<=num_of_plot
j=locations_of_frequency(i);
plot(period,fFI(:,j),'c*','LineWidth',2)
```

```
end
i=i+1;
if i<=num_of_plot
j=locations_of_frequency(i);
plot(period,fFI(:,j),'ms','LineWidth',2)
end
i=i+1;
if i<=num_of_plot
j=locations_of_frequency(i);
plot(period,fFI(:,j),'b+','LineWidth',2)
end
i=i+1;
if i<=num_of_plot
j=locations_of_frequency(i);
plot(period,fFI(:,j),'gp','LineWidth',2)
end
i=i+1;
if i<=num_of_plot
j=locations_of_frequency(i);
plot(period,fFI(:,j),'k.','LineWidth',2)
end
i=i+1;
if i<=num_of_plot
j=locations_of_frequency(i);
plot(period,fFI(:,j),'ro','LineWidth',2)
end
i=i+1;
if i<=num_of_plot
j=locations_of_frequency(i);
plot(period,fFI(:,j),'c*','LineWidth',2)
end
xlabel('Periods')
ylabel('Parameters')
title('{\bf CONVERGENCE PARAMETERS - PHASE FACTOR frequency OF INTEREST}');
legend('fFI(1)','fFI(2)','fFI(3)','fFI(4)','fFI(5)','fFI(6)','fFI(7)','fFI(8)','
fFI(9)','fFI(10)','Location','SouthEast');

 temp_name=sprintf('Convergence_indicators - %s',VARIABLE_NAME);
 saveas(gcf,[output_folder temp_name],'fig')

%%%%%%%EXCEL OUTPUT

%%%%%%%     WARNING
%%%%%%% About the frequencies typed by the user and the one reported in the
%%%%%%% output file, please read the warning message above, in the
%%%%%%% "FREQUENCY OF INTEREST" section.

 name_file=[name_output_file,VARIABLE_NAME];

label_0={'FREQUENCY  -->>>',};
data_0=[frequency_label];
label_1={'PERIODS','fM','fS','fP','fA(1)','fFI(1)','fA(2)','fFI(2)','fA(3)','fFI
(3)','fA(4)','fFI(4)','fA(5)','fFI(5)','fA(6)','fFI(6)','fA(7)','fFI(7)','fA(8)'
,'fFI(8)','fA(9)','fFI(9)','fA(10)','fFI(10)'};
data_1a=[period' fM' fS' fP(1:end-1)'];
data_1=[fA(:,aux_indexes(1,1)) fFI(:,aux_indexes(1,1))];
label_2={'dt original [s]',};
label_3={'dt interpolation [s]',};
label_4={'Sample per period',};
label_5={'Period length [s]',};
label_6={'Period frequency [Hz]',};

%%%%writing the excel file

xlswrite([output_folder name_file],label_2,'','B1');
```

```
xlswrite([output_folder name_file],dt_original,'','C1');
xlswrite([output_folder name_file],label_3,'','B2');
xlswrite([output_folder name_file],dt_interpolation,'','C2');
xlswrite([output_folder name_file],label_4,'','B3');
xlswrite([output_folder name_file],new_SAMPLE_PER_PERIOD,'','C3');
xlswrite([output_folder name_file],label_5,'','E1');
xlswrite([output_folder name_file],new_target_period,'','F1');
xlswrite([output_folder name_file],label_6,'','E2');
xlswrite([output_folder name_file],new_target_freq,'','F2');

xlswrite([output_folder name_file],label_0,'','C4');
xlswrite([output_folder name_file],data_0,'','E4');
xlswrite([output_folder name_file],label_1,'','A5');
xlswrite([output_folder name_file],data_1a,'','A6');
xlswrite([output_folder name_file],data_1,'','E6');
i=2;
if i<=n_of_frequency
data_2=[fA(:,aux_indexes(1,2)) fFI(:,aux_indexes(1,2))];
xlswrite([output_folder name_file],data_2,'','G6');
i=i+1;
end
if i<=n_of_frequency
data_3=[fA(:,aux_indexes(1,3)) fFI(:,aux_indexes(1,3))];
xlswrite([output_folder name_file],data_3,'','I6');
i=i+1;
end
if i<=n_of_frequency
data_4=[fA(:,aux_indexes(1,4)) fFI(:,aux_indexes(1,4))];
xlswrite([output_folder name_file],data_4,'','K6');
i=i+1;
end
if i<=n_of_frequency
data_5=[fA(:,aux_indexes(1,5)) fFI(:,aux_indexes(1,5))];
xlswrite([output_folder name_file],data_5,'','M6');
i=i+1;
end
if i<=n_of_frequency
data_6=[fA(:,aux_indexes(1,6)) fFI(:,aux_indexes(1,6))];
xlswrite([output_folder name_file],data_6,'','O6');
i=i+1;
end
if i<=n_of_frequency
data_7=[fA(:,aux_indexes(1,7)) fFI(:,aux_indexes(1,7))];
xlswrite([output_folder name_file],data_7,'','P6');
i=i+1;
end
if i<=n_of_frequency
data_8=[fA(:,aux_indexes(1,8)) fFI(:,aux_indexes(1,8))];
xlswrite([output_folder name_file],data_8,'','R6');
i=i+1;
end
if i<=n_of_frequency
data_9=[fA(:,aux_indexes(1,9)) fFI(:,aux_indexes(1,9))];
xlswrite([output_folder name_file],data_9,'','T6');
i=i+1;
end
if i<=n_of_frequency
data_10=[fA(:,aux_indexes(1,10)) fFI(:,aux_indexes(1,10))];
xlswrite([output_folder name_file],data_10,'','V6');
i=i+1;
end

disp(' ');
disp(' ');
disp('######        DONE!       ######');
```

APPENDIX B

Grid Convergence Index results

Table B.1. Uncertainty estimate for AUX mesh.

	INPUT PROPERTIES Φ					
	DRAG force over 5 periods			**LIFT** force over 3 periods		
MESH	MEAN	DELTA MAX	FREQ	MEAN	DELTA MAX	FREQ
RAW	0,003671	0,000122	25773,2	~~-2,58E-07~~	0,003979	12875,54
COARSE	0,004552	0,000340	27027,03	~~1,3E-05~~	0,006659	13513,51
AUX	0,004732	0,000424	27472,53	~~8,509E-06~~	0,007478	13698,63
	GCI RESULTS					
p	5,76	3,56	3,87	~~3,71~~	4,38	4,56
Φ_{ext}^{32}	0,004766	0,000464	27656,41	~~6,515E-06~~	0,007748	13755,38
e_a^{32}	3,80%	19,93%	1,62%	~~52,80%~~	10,95%	1,35%
e_{ext}^{32}	0,72%	8,65%	0,66%	~~30,62%~~	3,49%	0,41%
GCI^{32}	0,91%	11,84%	0,84%	~~29,30%~~	4,52%	0,52%
	TEST FOR MONOTONIC OR OSCILLATORY CONVERGENCE					
ε_{32}	-0,000180	-0,000085	-445,5	~~4,492E-06~~	-0,000819	-185,117
ε_{43}	-0,000880	-0,000217	-1253,83	~~-1,33E-05~~	-0,002680	-637,977
R	0,204295	0,388861	0,355311	~~-0,338806~~	0,305614	0,290162

Table B.2. Uncertainty estimate for AUX mesh.

	INPUT PROPERTIES Φ					
	P STAT BACK PROBE - 6 periods			**P STAT JUST DOWN** - 10 periods		
MESH	MEAN	DELTA MAX	FREQ	MEAN	DELTA MAX	FREQ
RAW	41707,39	196,460	25751,07	41670,914	124,020	25641,03
COARSE	40992,85	566,880	27027,03	40981,376	328,190	27027,03
AUX	40806,85	691,530	27397,26	40820,198	399,340	27472,53
	GCI RESULTS					
p	4,93	4,06	4,56	5,30	3,94	4,21
Φ_{ext}^{32}	40757,85	738,92	27510,75	40783,491	427,854	27630,8
e_a^{32}	0,46%	18,03%	1,35%	0,39%	17,82%	1,62%
e_{ext}^{32}	0,12%	6,41%	0,41%	0,09%	6,66%	0,57%
GCI^{32}	0,15%	8,57%	0,52%	0,11%	8,93%	0,72%
	TEST FOR MONOTONIC OR OSCILLATORY CONVERGENCE					
ε_{32}	185,993	-124,6500	-370,233	161,17841	-71,1500	-445,5
ε_{43}	714,547	-370,4200	-1275,95	689,53754	-204,1700	-1386
R	0,26029	0,33651	0,29016	0,23375	0,34848	0,32143

Table B.3. Uncertainty estimate for AUX mesh.

	INPUT PROPERTIES Φ					
	P TOT JUST DOWN - 10 periods			**P STAT PROBE TAP** - 5 periods		
MESH	MEAN	DELTA MAX	FREQ	MEAN	DELTA MAX	FREQ
RAW	41852,73	246,050	25641,03	46650,357	5,660	25773,2
COARSE	41387,41	719,120	27027,03	46599,552	9,400	27027,03
AUX	41311,82	961,220	27472,53	46597,958	10,880	27472,53
	GCI RESULTS					
p	6,55	2,63	4,21	12,26	3,50	3,87
Φ_{ext}^{32}	41301,05	1146,00	27630,80	46597,925	11,603	27656,41
e_a^{32}	0,18%	25,19%	1,62%	0,00%	13,60%	1,62%
e_{ext}^{32}	0,03%	16,12%	0,57%	0,00%	6,23%	0,66%
GCI^{32}	0,03%	24,03%	0,72%	0,00%	8,31%	0,84%
	TEST FOR MONOTONIC OR OSCILLATORY CONVERGENCE					
ε_{32}	75,5893	-242,1000	-445,5	1,5945	-1,4800	-445,5
ε_{43}	465,3213	-473,0700	-1386	50,8050	-3,7400	-1253,83
R	0,16245	0,51176	0,32143	0,03138	0,39572	0,35531

Table B.4. Uncertainty estimate for AUX mesh.

	INPUT PROPERTIES Φ			
	P TOT CAVITY - 5 periods			
MESH	MEAN	DELTA MAX	FREQ	
RAW	46652,18	5,850	25641,03	
COARSE	46604,12	13,950	27027,03	
AUX	46602,86	14,540	27472,53	
	GCI RESULTS			
p	12,92	9,33	4,21	
Φ_{ext}^{32}	46602,84	14,57	27630,80	
e_a^{32}	0,00%	4,06%	1,62%	
e_{ext}^{32}	0,00%	0,22%	0,57%	
GCI^{32}	0,00%	0,28%	0,72%	
	TEST FOR MONOTONIC OR OSCILLATORY CONVERGENCE			
ε_{32}	1,2508	-0,5900	-445,5	-
ε_{43}	48,0673	-8,1000	-1386	
R	0,02602	0,07284	0,32143	-

Table B.5. Uncertainty estimate for ULTRA mesh.

	INPUT PROPERTIES Φ					
	DRAG force over 5 periods			**LIFT** force over 3 periods		
MESH	MEAN	DELTA MAX	FREQ	MEAN	DELTA MAX	FREQ
COARSE	0,004552	0,000340	27027,03	~~1,3E-05~~	0,006659	13513,51
AUX	0,004732	0,000424	27472,53	~~8,509E-06~~	0,007478	13698,63
ULTRA	0,004756	0,000488	27777,78	~~-1,21E-05~~	0,007665	13888,89
	GCI RESULTS					
p	6,20	0,64	0,97	~~5,78~~	4,52	0,38
Φ_{ext}^{21}	0,004761	0,000796	28702,66	~~-1,67E-05~~	0,007733	15486,21
e_a^{21}	0,51%	13,12%	1,10%	~~170,28%~~	2,45%	1,37%
e_{ext}^{21}	0,10%	38,67%	3,22%	~~27,70%~~	0,88%	10,31%
GCI^{21}	0,12%	78,82%	4,16%	~~47,88%~~	1,10%	14,38%
	TEST FOR MONOTONIC OR OSCILLATORY CONVERGENCE					
ε_{21}	-0,000024	-0,000064	-305,25	~~2,062E-05~~	-0,000187	-190,259
ε_{32}	-0,000180	-0,000085	-445,5	~~4,492E-06~~	-0,000819	-185,117
R	0,135810	0,757651	0,685185	~~4,5890929~~	0,228883	1,027778

Table B.6. Uncertainty estimate for ULTRA mesh.

	INPUT PROPERTIES Φ					
	P STAT BACK PROBE - 6 periods			**P STAT JUST DOWN** - 10 periods		
MESH	MEAN	DELTA MAX	FREQ	MEAN	DELTA MAX	FREQ
COARSE	40992,85	566,880	27027,03	40981,376	328,190	27027,03
AUX	40806,85	691,530	27397,26	40820,198	399,340	27472,53
ULTRA	40740,11	774,940	27777,78	40761,347	426,000	27700,83
	GCI RESULTS					
p	3,07	1,05	0,38	3,02	2,93	1,92
Φ_{ext}^{21}	40694,47	1006,32	30972,42	40719,959	445,557	28003,28
e_a^{21}	0,16%	10,76%	1,37%	0,14%	6,26%	0,82%
e_{ext}^{21}	0,11%	22,99%	10,31%	0,10%	4,39%	1,08%
GCI^{21}	0,14%	37,32%	14,38%	0,13%	5,74%	1,36%
	TEST FOR MONOTONIC OR OSCILLATORY CONVERGENCE					
ε_{21}	66,7392	-83,4100	-380,518	58,8510	-26,6600	-228,304
ε_{32}	185,9929	-124,6500	-370,233	161,1784	-71,1500	-445,5
R	0,35883	0,66915	1,02778	0,36513	0,37470	0,51247

Table B.7. Uncertainty estimate for ULTRA mesh.

	INPUT PROPERTIES Φ					
	P TOT JUST DOWN - 10 periods			**P STAT PROBE TAP** - 5 periods		
MESH	MEAN	DELTA MAX	FREQ	MEAN	DELTA MAX	FREQ
COARSE	41387,41	719,120	27027,03	46599,552	9,400	27027,03
AUX	41311,82	961,220	27472,53	46597,958	10,880	27472,53
ULTRA	41299,79	1054,320	27700,83	46595,621	16,130	27777,78
	GCI RESULTS					
p	5,69	2,85	1,92	1,65	4,84	0,97
Φ_{ext}^{21}	41297,00	1125,62	28003,28	46591,873	17,803	28702,66
e_a^{21}	0,03%	8,83%	0,82%	0,01%	32,55%	1,10%
e_{ext}^{21}	0,01%	6,33%	1,08%	0,01%	9,40%	3,22%
GCI^{21}	0,01%	8,45%	1,36%	0,01%	12,97%	4,16%
	TEST FOR MONOTONIC OR OSCILLATORY CONVERGENCE					
ε_{21}	12,0294	-93,1000	-228,304	2,3372	-5,2500	-305,25
ε_{32}	75,5893	-242,1000	-445,5	1,5945	-1,4800	-445,5
R	0,15914	0,38455	0,51247	1,46580	3,54730	0,68519

Table B.8. Uncertainty estimate for ULTRA mesh.

	INPUT PROPERTIES Φ			
	P TOT CAVITY - 5 periods			
MESH	MEAN	DELTA MAX	FREQ	
COARSE	46604,12	13,950	27027,03	
AUX	46602,86	14,540	27472,53	
ULTRA	46602,57	20,740	27700,83	
	GCI RESULTS			
p	4,46	8,81	1,92	
Φ_{ext}^{21}	46602,47	21,25	28003,28	
e_a^{21}	0,00%	29,89%	0,82%	
e_{ext}^{21}	0,00%	2,38%	1,08%	
GCI^{21}	0,00%	3,05%	1,36%	
	TEST FOR MONOTONIC OR OSCILLATORY CONVERGENCE			
ε_{21}	0,29166	-6,2000	-228,304	-
ε_{32}	1,25080	-0,5900	-445,5	
R	0,23318	10,50847	0,51247	-

Acronyms and symbols

A	Normalized discrete Fourier magnitude
A	Advective fluxes
CCF	Cross correlation coefficient
CFD	Computeational fluid dynamics
c	Speed of sound
Cd	Drag coefficient
CFL	Courant Friedrichs Lewy number
Cp	Pressure coefficient
c_p	Specific heat at constant pressure
D	Base diameter of the conical cavity, drag force
D	Diffusive fluxes
dl	Length of the modelled section of the probe
DFT	Discrete Fourier Transform
d_t	Tap diameter
E	Young modulus
E	Energy
Err_k	Discretization error on mesh level k
e_a^{ij}	Approximate relative error
e_{ext}^{ij}	Extrapolated relative error

F_d	Drag force
f	Period frequency
L	Line length
L_k	Kiel length
l	Cantilever beam length
GCI	Grid convergence index
g	Acceleration of gravity
g_i	Coefficients of the error expansion terms
h	Height of a streamline on a reference point, enthalpy
h_k	Measure of grid spacing
I	Inertia modulus
i	Imaginary unit
Im	Imaginary part of a complex number
k	Turbulent kinetic energy
Kp_{TAP}	Total pressure ratio
K_{rec}	Recovery coefficient
M	Mach number
m	mass
N	Number of time steps per period; total number of cells
p	Pressure; apparent order of the numerical method
p_0	Total pressure
P	Fourier transformed variable

Pr_t	Turbulent Prandtl number
PSD	Power spectral density
q	Generic quantities monitored
$q'(t)$	Time dependent fluctuation of the generic quantity monitored
R	Universal constant of gas
r	Refinement ratio
Re	Real part of a complex number
Re	Reynolds number
S	Source terms, control surface
$\boldsymbol{S}$	Surface vector
s	Stress at a cross section of a cantilever beam
St	Strouhal number
T	Period length
t	Time
U,V,W	Velocity vector mean components in x,y,z directions
u,v,w	Velocity fluctuating components in x,y,z directions
th	Material thickness
th_k	Kiel thickness
V	Cavity volume, module of the velocity vector
$\boldsymbol{V}$	Velocity vector
v	Velocity

Vt Line volume

W Total load on a cantilever beam, transport variable

w_k Discrete solution on mesh level k

w_{exact} Exact solution to the continuum

Z Section modulus of the cross section of a beam

α Angle of the conical cavity

$\Gamma_{\emptyset}$ Fluid thermal conductivity

Γ_t Turbulent heat conductivity

γ Specific heat ratio

Δf Discretization step size in the frequency domain

Δt Discretization time step size

ΔV_i Volume of the i-th cell

ΔA_i Area of the i-th cell

$\delta_{\max}$ Maximum deflection

ϕ Phase

ϕ_k Kiel diameter

ϕ_p Probe external diameter

ϕ_s Sensor diameter

$\varphi(t)$ Generic flow property

$\emptyset, \bar{\varphi}$	Property mean value
ω	Natural or resonant frequency
ζ	Non dimensional damping
μ	Viscosity (kinematic)
μ_t	Turbulent eddy viscosity
ν	Dynamic viscosity
ρ	density
τ	Artificial time
τ_{ij}	Reynolds stresses
Ω	Control volume

Bibliography

[1] G. Persico. *Unsteady Aerodynamic Stator-Rotor Interaction in High Pressure Turbines* PhD Thesis Politecnico di Milano, Dottorato in Energetica: XVIII Ciclo, 2006. Von Karman Institute for Fluid Dynamics ISBN: 978-2-930389-26-5

[2] C. H. Sieverding, T. Arts, R. Dénos, J.-F. Brouckaert. *Measurement techniques for unsteady flows in turbomachines.* Experiments in Fluids 28 (2000) 285-321 Springer-Verlag 2000

[3] D. W. Bryer, R.C. Pankhurst. *Pressure-probe methods for determining wind speed and flow direction.* National physical laboratory, Department of trade and industry. Published by Her Majesty's Stationery Office, 1971. SBN 11 480012 X

[4] P. Kupferschmied, Ch. Gossweiler, G. Gyarmathy. *Aerodynamic fast-response probe measurement systems: state of development, limitations and future trends.* Proceedings of the 12th Symposium on Measuring Techniques for Transonic and Supersonic Flow in Cascades and Turbomachines, Prague, Czech Republic, September 12-13,1994, Paper 18

[5] J. Anthoine, T. Arts, H.L. Boerrigter, J.-M. Buchlin, M. Carbonaro, G. Degrez, R. Dénos, D. Fletcher, D. Olivari, M.L. Riethmuller, R. A. Van den Braembussche. *MEASUREMENT TECHNIQUES IN FLUID DYNAMICS An Introduction, 3rd revised edition*. Reprint of VKI LS 1994-01, 2009. ISBN: 978-2-930389-96-6

[6] F. P. Incropera, D. P. DeWitt, T. L. Bergman, A. S. Lavine. *Fundamentals of heat and mass transfer, sixth edition* Wiley

[7] D. Delhaye, G. Paniagua, J. M. Fèrnández Oro, R. Dénos. *Enhanced performance of fast-response 3-hole wedge probes for transonic flows in axial turbomachinery.* Experiments in Fluids, January 2011, Volume. 50, Issue 1, p. 163-177, Springer

[8] P. Kupferschmied, P. Koppel, C. Roduner, G. Gyarmathy. *On the Development and Application of the Fast-Response Aerodynamic Probe System in Turbomachines - Part 1: The Measurement System.* Journal of Turbomachinery, July 2000, Vol. 122 / 041027 p. 505-516

[9] A. Pfau, J. Schlienger, A. I. Kalfas, R. S. Abhari. *Virtual Four Sensor Fast Response Aerodynamic Probe (FRAP®).* Proceedings of the 16th Symposium on Measuring Techniques in Transonic and Supersonic Flow in Cascades and Turbomachines. Cambridge, UK, September 2002

[10] S. Chirico. *Studio numerico sul comportamento aerodinamico di sonde pneumatiche di pressione per misure in turbomacchine.* Master Thesis, Politecnico di Milano, Academic year 2007-2008

[11] P. Kupferschmied, P. Koppel, W. Gizzi, C. Roduner, G. Gyarmathy. *Time-resolved flow measurements with fast-response aerodynamic probes in turbomachines.* Measurement Science and Technology, 11(2000) 1036-1054

[12] J. F. Brouckaert. *Fast Response Aerodynamic probes for measurements in turbomachines* Proc. IMechE Vol. 221 Part A: J. Power and Energy p.803-814. DOI: 10.1243/09576509JPE460

[13] G. Persico, P. Gaetani, A. Guardone. *Design and analysis of new concept fast-response pressure probes* Measurement Science and Technology, 16(2005) 1741-1750

[14] J.-F. Brouckaert. *Developement of Fast Response Aerodynamic Pressure Probes fot Time-Resolved Measurements in Turbomachines*. PhD thesis, ULB-VKI, 2004.

[15] R. W. Ainsworth, R. J. Miller, R. W. Moss and S. J. Thorpe. *Unsteady pressure measurement.* Measurement Science and Technology, 11(2000) 1055-1076

[16] E. Ower, R. C. Pankhurst. *The measurement of air flow, 4^{th} edition.* Pergamon Press, 1966

[17] E. Oberg, F. D. Jones. *Machinery's handbook, 5th edition* The industrial press, New York, 1915.
http://www.evenfallstudios.com/woodworks_library/machinery_handbook_for_machine_shop_and_drafting_room_1914.pdf

[18] A. G. Piersol, T. L. Paez. *Harris' Shock and Vibration Handbook, 6th edition* McGraw-Hill Handbooks ISBN: 978-0-07-163343-7

[19] J. P. Clark, E. A. Grover. *Assessing convergence in predictions of periodic-unsteady flowfields* AFRL-PR-WP-TP-2006-241. AIR FORCE RESEARCH LABORATORY WRIGHT-PATTERSON AIR FORCE BASE, OH 45433-7251
Proceedings of GT2006 ASME TURBO EXPO 2006: Power of Land, Sea and Air. May 8-11, 2006, Barcelona, Spain. GT2006-90735

[20] O. Rodriguez. *The Circular Cylinder in Subsonic and Transonic Flow*. AIAA Journal, vol. 22, no.12, December 1984

[21] J. H. Lienhard IV, J. H. Lienhard V. *A heat transfer textbook, 3rd edition* Phlogiston Press, Cambridge Massachusetts

[22] J. H. Lienhard. *Synopsis of lift, drag, and vortex frequency data for rigid circular cylinders.* Bulletin 300, Washington State University, 1966

[23] U. Fey, M. König, H. Eckelmann. *A new Strouhal-Reynolds-number relationship for the circular cylinder in the range 47<Re<2x10^5*. Physics of fluids, Vol. 10, No. 7, July 1998, p. 1547, 1549

[24] User Manual. *FINE™/Open v2.12 (Including OpenLabs) Flow Integrated Environment.* Documentation v2.12c December 2012 - NUMECA International

[25] H. K. Versteeg, W. Malalasekera. *An Introduction to Computational Fluid Dynamics, 2nd edition.* Pearson Education
ISBN: 978-0-13-127498-3

[26] Theoretical Manual. *FINE™/Open v2.12 (Including OpenLabs) Flow Integrated Environment.* Documentation v2.12c December 2012 - NUMECA International

[27] G. Vaz, R. van der Wal., C. Mabilat, P. Gallagher *Viscous flow computations on smooth cylinders a detailed numerical study with validation.* Proceedings of OMAE2007, 26th International Conference on Offshore Mechanics and Arctic Engineering. June 10-15, 2007, San Diego, California, USA. OMAE2007-29275

[28] I. B. Celik. *Procedure for Estimation and Reporting of Discretization Error in CFD Applications.* Journal of Fluids Engineering Editorial Policy - Statement on the Control of Numerical Accuracy
http://journaltool.asme.org/templates/JFENumAccuracy.pdf

[29] P. J. Roache. *Quantification of uncertainty in computational fluid dynamics.* Annual Review of Fluid Mechanics Vol. 29, 1997, p. 123, 160
http://www.stanford.edu/group/uq/docs/roache.pdf
http://www.annualreviews.org/doi/pdf/10.1146/annurev.fluid.29.1.123

[30] C. J. Roy. *Grid Convergence Error Analysis for Mixed-Order Numerical Schemes.* AIAA Journal Vol. 41, No.4, April 2003

[31] T. Xing, F. Stern. *Factors of Safety for Richardson Extrapolation* Journal of Fluids Engineering, June 2010, Vol. 132 061403

[32] F. Stern, R. V. Wilson, H. W. Coleman, E. G. Paterson. *Comprehensive Approach to Verification and Validation of CFD Simulations - Part 1: Methodology and Procedures.* Journal of Fluids Engineering, Vol. 123, p. 793, 802, December 2001

[33] I. Celik, O. Karatekin. *Numerical Experiments on Application of Richardson Extrapolation With Nonuniform Grids.* Journal of Fluids Engineering, Vol. 119, p. 584, 590, September 1997

[34] C. Wieselberger. *New data on the laws of fluid resistance.* Technical notes, No. 84, National Advisory Committe for Aeronautics. Taken from "Physikelische Zeitschrift", 1921, Vol. 22.

[35] A. Roshko. *Experiments on the flow past a circular cylinder at very high Reynolds numbers.* Journal of fluid mechanics, vol. 10, part 3, May 1961

[36] E. Shirani. *Compressible Flow Around A Circular Cylinder.* Pakistan Journal of Applied Sciences 1(4): 472-476, 2001

[37] L. Colombo. *Dispensa sui flussi con separazione dello strato limite*. Notes for the course "Heat and mass tranfer" held at Politecnico di Milano, 2011.